High resolution hydrographic reconstructions from the Southeast Pacific spanning Antarctic Warming event A2 (44-48 Kyr BP)

By

TORBJØRN GRIMEN

MASTER THESIS IN MARINE GEOLOGY

Department of Earth science

University of Bergem

October 2022

Abstract:

Knowledge about and reconstructions of past climate change is important to distinguish between natural climate variability on various time scales and the more recent man-made climate changes. In this thesis, sub-millennial resolved proxy records of upper ocean variability (foraminiferal assemblages and lithic counts) as well as intermediate ocean variability (benthic oxygen isotopes) are produced from Ocean Drilling Program Site 1233 (41°0.005'S, 74°26.992'W, 838 m.b.s.l) from the Southeast Pacific from 44 to 48 Kyr BP. This interval spans Antarctic Warming event 2, which is one of the most prominent millennial scale warming events observed in Antarctic ice cores. The new records offer the opportunity to simultaneously monitor both AAIW and southeast Pacific surface water properties and unravel how they are influenced by the major atmosphere- and ocean-systems intersecting the study area, as well as unraveling past variations in the Patagonian Ice Sheet.

Using planktonic foraminiferal assemblage counts and $d^{18}O$ to portray climate over A2, we demonstrate that extratropical near surface ocean properties are extremely variable on millennial-decadal timescales. Furthermore, using ice-rafted debris (IRD) counts, and planktonic foraminifer assemblages to infer iceberg supply and melt water input, this study find strong indications for a coupling of the SE Pacific temperature and Patagonian Ice Sheet (PIS) fluctuations during A2 on sub-millennial time scales. Benthic foraminifera $d^{18}O$ and $d^{13}C$ are used to monitor the properties of AAIW close to its source in the Southeast Pacific, and the new benthic isotopic results spanning A2 show that variations in intermediate ocean properties and climate (foraminiferal census counts and planktic isotopes) of the Southeast Pacific closely align with the record of air temperatures from the EPICA Dronning Maud Land ice core on millennial and centennial scales.

The abrupt and concurrent shifts in extratropical surface and intermediate ocean properties over A2 are most likely driven by latitudinal shift of frontal systems in the Southern Hemisphere, shifting equatorward during cold phases and poleward during warm intervals. The extension of the Antarctic climate signal into the intermediate ocean demonstrates that AAIW is extremely sensitive and responds rapidly to climate variability in its source region in a broad spectrum of timescales. The broad coherence of the observed Antarctic signal supports the concept of hemispheric thermal asynchrony on millennial timescales.

The new results show that changes in ocean temperatures in the Southeast Pacific can have a significant impact on tropical waters and thus tropical climate change. If such natural variations arise today, they can alternately reduce or amplify man-made climate changes. The results can be used in models that simulate the climate change of both the past, the present and the future.

Acknowledgements:

I would like to thank my supervisor team Helga (Kikki) Flesche Kleiven, Ulysses S. Ninnemann and Nil Irvali for the guidance, discussion and assistance throughout this period. Your passion for the Marine Geology field is truly inspiring and unmatched, and thank you for introducing me to your field of study

A huge thank you to Nil Irvali, for the training in identifying the different foraminifera, and for always being available to check in I identified the right foraminifera.

Also huge thanks to Kikki and Ulysses for thorough and honest feedback throughout this period, and especially the last two weeks, with very quick feedback when time was limited. And tolerate all my simple spelling mistakes.

I would also like to thank Anna Tran for showing me around the FARLAB at the Department of Earth Science.

I would also like to thank my fellow students at the Institute of Earth Science and in the end, I would like to thank my family for support through this period.

Contents

1. Introduction

This study contributes to the ongoing work on the sediment cores collected during the International Ocean Discovery Program (IODP) legacy coring program ODP (Ocean Drilling Program) Leg 202 (Shipboard Scientific Party, 2003. Leg 202 summary) in the Southeast Pacific Ocean and is also a contribution to the Department of Earth Science and University of Bergen's contribution to Norway's membership in the European Consortium for Ocean Research Drilling (ECORD).

In this thesis, the near surface ocean and intermediate water climate variability are studied at high resolution by applying foraminiferal-based proxy reconstructions to a core drilled along the Chilean margin. This study make use of already collected marine sediment core samples from Ocean Drilling Program Site 1233 and spans an interval known as Antarctic Warming Event 2 (A2) in the Antarctic ice cores (Blunier and Brook, 2001) A2 occurs during Marine Isotope Stage (MIS) 3 from 48-44 Kyr BP and is now often referred to as Antarctic Isotope Maximum (AIM) 12 if one applies the new nomenclature of the European Project for Ice Coring in Antarctica (EPICA) project (EPICA Community Members, 2006)

ODP Site 1233 is located on the northern margin of the Antarctic Circumpolar Current and its seafloor lies in the core of Antarctic Intermediate Water (AAIW). Thus, the site is ideally situated to reconstruct both near surface and AAIW variability in the high southern latitudes.

The thesis has been supervised by Associate professor Kikki Flesche Kleiven, Researcher Nil Irvali and Professor Ulysses Ninnemann, all from Department of Earth Science and the Bjerknes Centre for climate Research at the University of Bergen. The stable isotope analyses are performed at Facility for advanced isotopic research and monitoring of weather, climate, and biogeochemical cycling (FARLAB) at the Department of Earth Science.

1.1 Objectives

The objectives of this master thesis project are:

- Reconstruct and study in detail climate variability over the A2 interval at ODP Site 1233 with a focus on sea surface temperature variability and changes in frontal positions along the Chilean margin.

- Reconstruct ice sheet variability of the Patagonian Ice Sheet by using iceberg-transported sediment grains detected in the same core samples.

- Reconstruct the physical (density) and chemical (nutrient) variability of Antarctic Intermediate Water (AAIW) over the A2 interval using benthonic foraminifera stable isotope analysis.

1.2 Aim of this study

Abrupt climate changes on centennial and decadal scales have gained broad scientific interest due to the need to place in context recent climate changes relative to human induced and natural variability (Hansen and Sato, 2012). The scientific aim of this thesis is to capture rapid, sub-millennial changes in water masses in the southeast Pacific by measuring planktic and benthic foraminiferal oxygen- and carbon isotopes and study foraminiferal assemblages in core ODP Site 1233 to portray changes in the position of water masses and frontal systems relative to Antarctica and Chile. This study aims to provide new insight that can help define past behaviour of southeast Pacific near surface and intermediate water properties off Chile. The 135-meter-long sediment archive drilled at Site 1233 can be seen as a marine analogue (Figure 1.1 and 1.2) of the recent high-resolution Antarctic ice-cores—filling an important knowledge gap regarding the role of the Southern Ocean in the global climate system

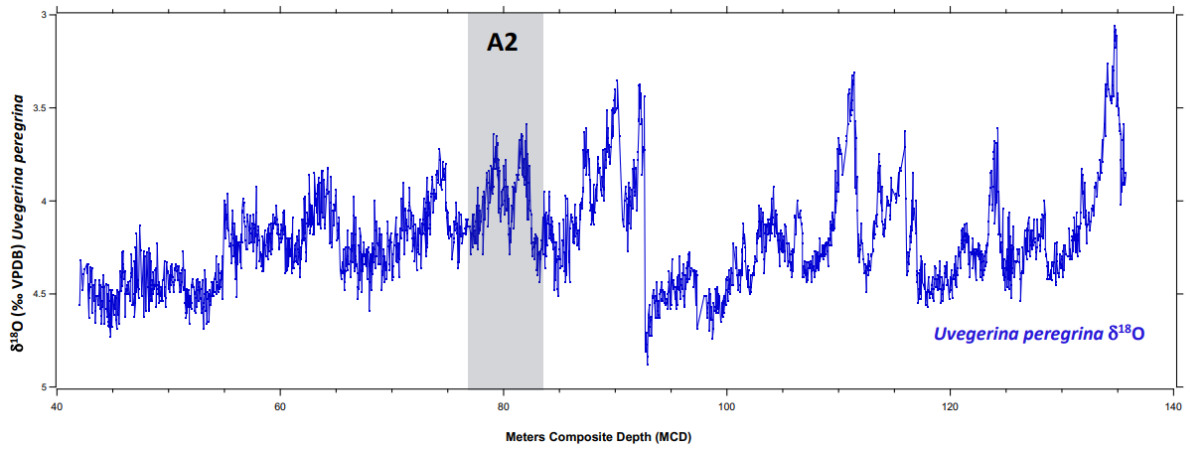

Figure 1.1: *Uvegerina peregrina* $\delta^{18}O$ at ODP 1233 (Kleiven and Ninnemann, in prep) spanning the full spliced core length plotted versus meters composite depth. The A2 study interval is indicated by a grey shaded vertical column.

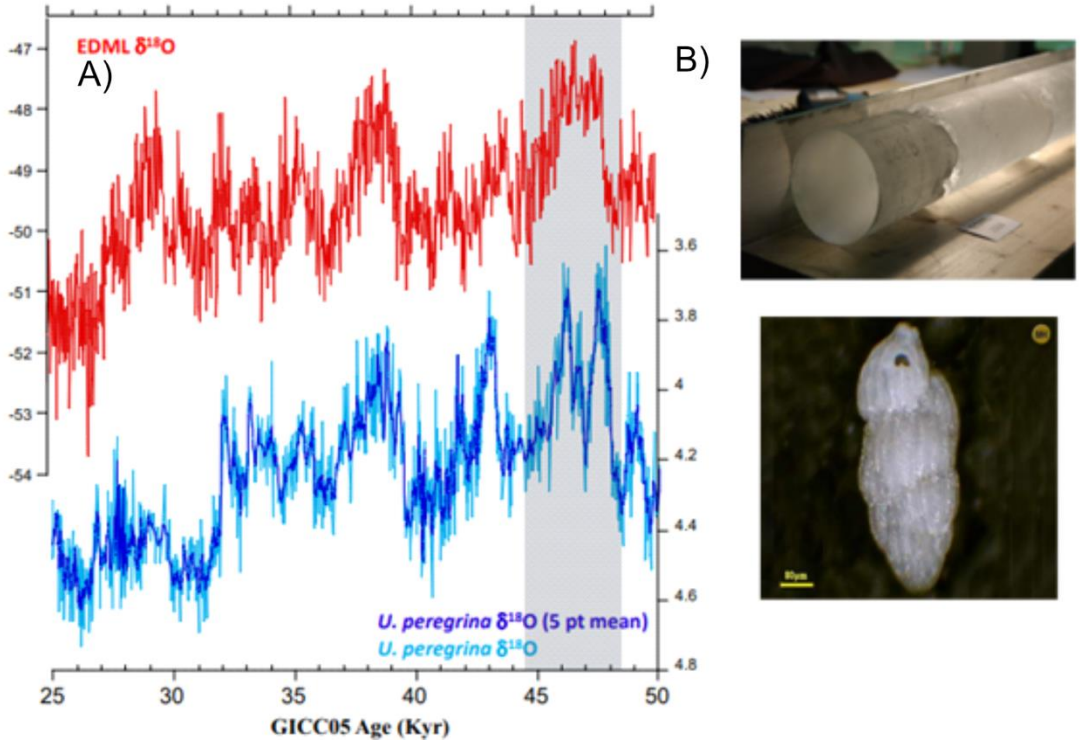

Figure 1.2 A) *Uvegerina peregrina* $\delta^{18}O$ at ODP 1233 (Kleiven and Ninnemann, in prep) and Epica Dronning Maud Land ice core $\delta^{18}O$ (EPICA Community Members, 2006 and 2010) plotted versus age spanning the 25-55 kyr interval. The A2 study interval is indicated by a grey shaded vertical column. B) Photo of an ice core and the shell of *Uvegerina Peregrina* to underscore the different proxy origin of the $\delta^{18}O$ signals in plot A.

1.2.1 Test: resolve the sense and timing of Southern Hemisphere climate change

How variable are the hydrography and the properties of extratropical near surface waters during A2?

How much has Antarctic Intermediate Water changed in the past?

Does the Antarctic climate signal extend to the Southern Hemisphere subtropics (41°S)?

Does the Southern Hemisphere upper ocean (thermocline) warm/thicken as predicted in models?

Do Antarctic changes reflect the Southern Hemisphere, i.e., test if the climate signal in the southeast Pacific (Site 1233) and Chile (terrestrial proxies) align with the EPICA Dronning Maud Land ice core record and the Southern Ocean as a whole.

2. Introduction to palaeoceanography and climate research

The study and understanding of climate change has been of interest and a focus for research to many scientists over the last century. In view of the ongoing climate changes, the need to understand more about the climate system and how different mechanisms, drivers and feedbacks influence climate and respond to rising CO_2 levels has become more important than ever. Today atmospheric CO_2 levels are rising faster than ever recorded in human history (Tierney et al., 2020). Past climates inform our future. and the average global temperature is 1.2°C above pre-industrial levels (IPCC, 2021), rapidly changing conditions on land, in the ocean, glacial extent and global ecosystems. It is therefore relevant to understand how key elements of the climate system are affected under various greenhouse gas levels. To secure the future of humankind we must rapidly reduce our fossil fuel emissions and at the same time, adapt to a changing world. One way to learn what our new world will look like in the future is to study climate archives from the past that hold lessons for the future. Using the phrase "The past is the key to the future" (Doe, 1983) and reconstruct climate change on various timescales, we can more easily predict and understand what the climate will be in the future. The laws of physics do not change with time and climate, thus the processes which were active in the past must also be active today and in the future.

Proxy data are the most common way to study at past climate. Climate proxies are recorded chemical and physical characteristics that act as a substitute for direct temperature measurements. Proxy signals are preserved in multiple ways, often in ice sheets, in marine sediments and in sedimentary rocks. By sampling these archives, we can extract climate data. Marine sediment cores, ice cores, lacustrine cores and speleothems are the most common archives used to reconstruct the past climate. For example, from one single marine sediment core we can use proxy records depicting temperatures, CO2, sea level and ice volume. Over the last three decades there has been much focus on finding high-deposition sites in the ocean, from which ultra-high resolution climate records can reconstructed on millennial-decadal scales. Figure 2.1 demonstrate the status of high-resolution palaeoceanographic records up until 2002, but already that year, ODP Leg 202 drilled the core used in this study along the Chilean margin, and since then more unique coring sites have been found. However, the Southern Ocean remains under sampled when compared to the North Atlantic Ocean, underscoring the need for new detailed studies from this region.

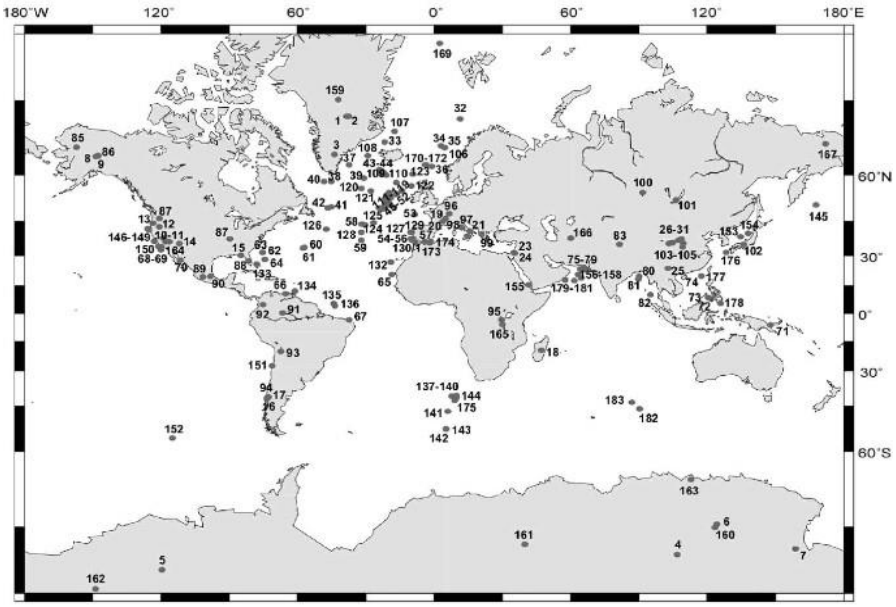

Figure 2.1: Map showing where all palaeoceanographic cores with a resolution > 500 years, have been drilled up until 2002 (Voelker et al., 2002).

One of the most significant natural climate variabilities that has left it's imprint in various climate archives are the recurring glacial to interglacial cycles. The work on this was initiated by Milankovitch (1941) through his theory on orbital forcing. Milankovitch proposed that changes in the shape of the Earth's orbit (eccentricity), the angle of the Earth's axis with respect to Earth's orbital plane (obliquity) and the orientation of the Earth's rotational axis (precession) strongly influenced the Earth's climatic patterns and pushed the Earth in and out of ice ages on the same periodicity as eccentricity, obliquity and precession (100ky, 41ky and 21ky cycles respectively). Then forty-six years ago, Hays, Imbrie and Shackleton (1976) published a paper where they found evidence in proxy records from a marine sediment core in the Pacific Ocean that the variations in Earth's orbit around the Sun were the pacemaker of the ice ages during the Quaternary Period (the current geological period, which began about 2.6 million years ago).

Since then, palaeoceanographic and paleoclimatic studies from all over the globe have provided much deeper and detailed knowledge on climate variability on various timescales, but the theory of orbital forcing is still considered most important for the glacial and interglacial cycles.

In the marine sediment cores, taken from the bottom of the sea (fig. 2.1), fossil remains from various microorganisms are found, often in large quantities. One of these organisms, called foraminifera, form calcareous shells, and have proven to be excellent recorders of past climate variability. Calcareous shells of foraminifera can preserve the chemistry of the ocean water in which they lived. When foraminifera die, they sink to the bottom of the ocean and become part of the ocean sedimentary layers. In fact, Vincent and Berger (1981) estimates that the annual deposition of planktic foraminifera on the sea floor is so enormous, that in 500 years, carbon equal to that of the entire biosphere is deposited. Foraminifera that dwell in waters close to the sea surface and subsurface, are called planktonic foraminifera whereas those that dwell on the seafloor or in the sediments on the seafloor, are called benthic foraminifera. Different foraminifera also prefer different environments, some are abundant in the cold Arctic Ocean, others in the Tropics while some prefer environments with large amounts of upwelling and nutrients.

The use of foraminifera as a climate proxy is especially frequent when reconstructing climate variability during the Pleistocene period (last 2.6 Ma) with particular focus on the last glacial cycle and the current Holocene interglacial interval that was initiated at 11700 ka. One reason is because these records can be more accurately dated using the Accelerator Mass Spectrometry (AMS) ^{14}C dating method, another is that this interval is within reach for most conventional piston coring equipment onboard research vessels. To reconstruct past climate variability from marine sediment cores, large international scientific ocean drilling campaigns has been funded and marine sediment cores has been drilled in all ocean basins, through for instance the International Ocean Discovery Program (IODP). The marine sediment sequences that are retrieved can be several 100 meters long and when cored in areas with extremely high sedimentation rates they can provide climate variability on centennial to decadal time scales. The core used in this thesis, Ocean Drilling Program (ODP) Site 1233, from leg 202, is a 136-meter-long spliced sediment core sequence, which gives detailed climate information spanning the last 75 Kyr (Tiedemann & Mix, 2007). The focus in this thesis will be on the interval between 44 and 48 Kyr BP, spanning Antarctic Isotope Maxima (AIM) 2 (or A2) (Figure 2.2).

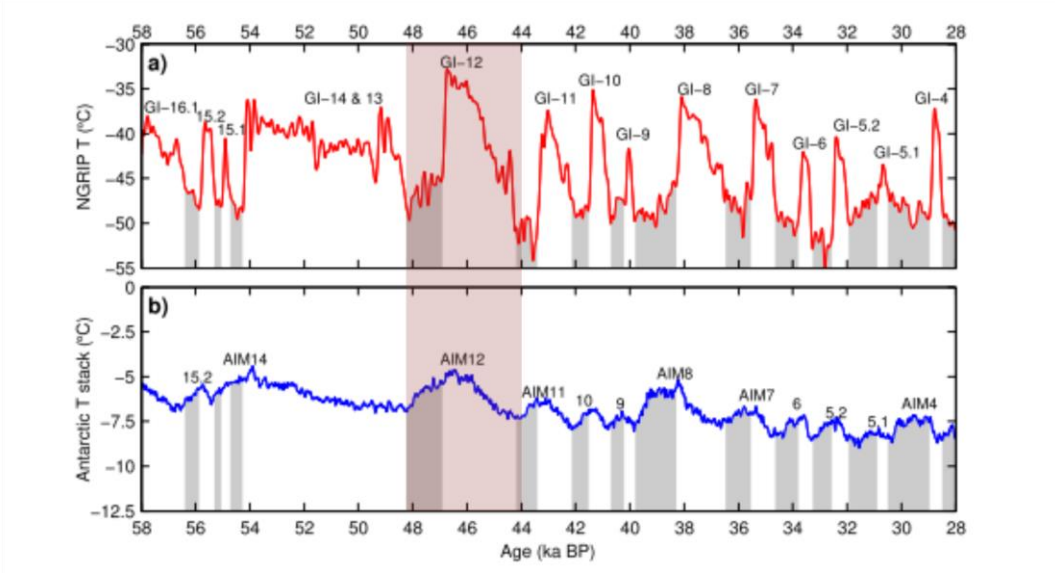

Figure 2.2: Temperature reconstruction from (a) North Greenland Ice core Project (NGRIP) and (b) Average of six Antarctic ice cores (EDML, Vostok, Talos dome, Dome Fuji, WAIS divide and EPICA Dome C) spanning MIS 3. The Greenland cold stadials are marked in grey shading. Note that every Greenland stadial coincide with the relatively warm AIM's. The red shaded vertical bar highlights the study interval in this thesis. Modified after Pedro et al., (2018).

2.1 The Bipolar seesaw hypothesis

Studies on climate archives from ice cores and marine sediment cores from the Northern Hemisphere (NH) were the first to demonstrate high frequency abrupt millennial scale temperature oscillations that was superimposed on the longer orbital-scale cycles. These abrupt climate changes were characterized by rapid changes in North Atlantic Sea surface temperatures and rapid increases in the atmospheric temperature over Greenland (W. S. Broecker, 1998; Stocker & Johnsen, 2003). Up until this discovery, it was believed that the Ice Ages were just stable cold periods. Now it is well documented from several climate archives in many other places in the world that during the last glacial period, the temperature repeatedly and suddenly increased and decreased (summarized by Voelker, 2002).

This rapid (1000 yr) climate fluctuations between cold and warm states are most prominently observed in the Greenland ice cores, where the change in temperature from stadial to interstadial conditions are up to up to 15˚C (North Greenland Ice Core Project Member, 2004). At first these results were thought to be just noise, but several decades of detailed studies have

shown that they are robust features of the last glacial period. These changes have the largest amplitude during Marine Isotope Stage 3 (59-20 Kyr B.P. (Voelker et al., 1998; van Kreveld et al., 2000), but are also clearly present during MIS 2 and 4 (Bond et al., 1992, McManus et al., 1994, Oppo et al., 1995) and even during older glacial periods during the Pleistocene (Kleiven et al., 2003).

It is currently unknown what the causes or triggers these temperature variations. However, Bond et al (1997) suggest this millennial scale variability is caused by a periodic (or quasiperiodic cycle with a periodicity on 1500 yrs. Today these cycles are known as Dansgaard-Oeschger (D-O) oscillations and are named after Dansgaard et al. (1984) and Oeschger et al. (1983) who first discovered them. The D-O oscillations are related to episode of large iceberg discharge from the Laurentide Ice Sheet to the North Atlantic during the last glacial (Bond et al., 1993). These discharges, called Heinrich events, happens during the coldest periods of the cycle (Bond et al, 1993). The Heinrich events are recognized by a decrease in foraminifera flux, lower δ^{18}O values due to freshwater input, and large amounts of ice rafted debris (IRD). The D-O oscillations have been tightly coupled to changes in the Thermohaline Circulation in the North Atlantic Ocean (Keigwin and Lehman, 1994, Oppo and Lehman, 1995, McManus et al., 1999). Heat transport and North Atlantic Deep Water (NADW) formation contributes to milder climate in north-western Europe, and Blunier and Brook (2001) claim latitudinal shifts in the NADW formation zone was caused by increased temperature over Greenland, and that meltwater pulses and increased IRD flux happened prior to a reduction in NADW formation. This led to reduces northward heat flux, cooling the North Atlantic Ocean and re-established NADW formation. Clark et al. (2002) claims that the freshwater budget in NA is the main component controlling the currents in North Atlantic, but his hypothesis doesn't have a controlling factor for the 1500 cycles.

Later it was discovered that Antarctic ice cores also have distinct warm events superimposed on the orbital background signal (Grootes et al., 2001; Johnsen et al., 1972; Jouzel et al., 1987), the so called Antarctic warming events 1-7 (Blunier and Brooke, 2001) but they are not as distinct nor so abrupt as in the Greenland ice cores (fig. 2.2) The study by Blunier and Brooke (2001) show that the Byrd ice cores temperatures gradually increase when it is cold over Greenland and gradually cools while it is relatively warm over Greenland. In 2006, EPICA community members published results from a new high-resolution Antarctic ice core drilled

in Dronning Mauds Land, with a resolution that is starting to match the Greenland ice cores (EPICA community member, 2006). The new results showed a one-to-one coupling between every millennial-scale DO event in Greenland and an accompanying cold event in Antarctica (fig. 2.3).

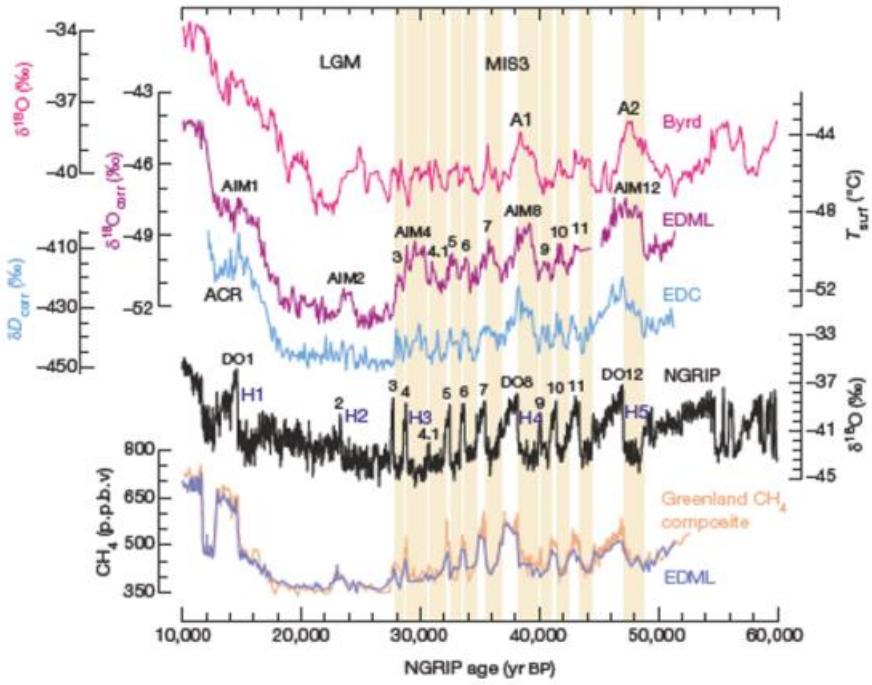

Figure 2.3: Methane synchronisation of the EDML and NGRIP revealing the one- to- one coupling of Antarctic interstadials with Greenland stadial (EPICA community members, 2006).

This demonstrate that the temperatures are antiphased between the NH and the SH. When Greenland experiences a temperature increase, the temperature in Antarctica decreases ca. 200 year after, and vice versa (EPICA community Members, 2015). This led to the hypothesis that these two temperature anomalies are connected (Stocker & Johnsen, 2003), i.e.," the Bipolar Seesaw" hypothesis. Over the last decades scientists have tried to resolve how these processes are connected, and the leading hypothesis is that it is connected to the ocean conveyer belt, also called the Thermohaline Circulation (THC) (Rahmstorf, 2002).

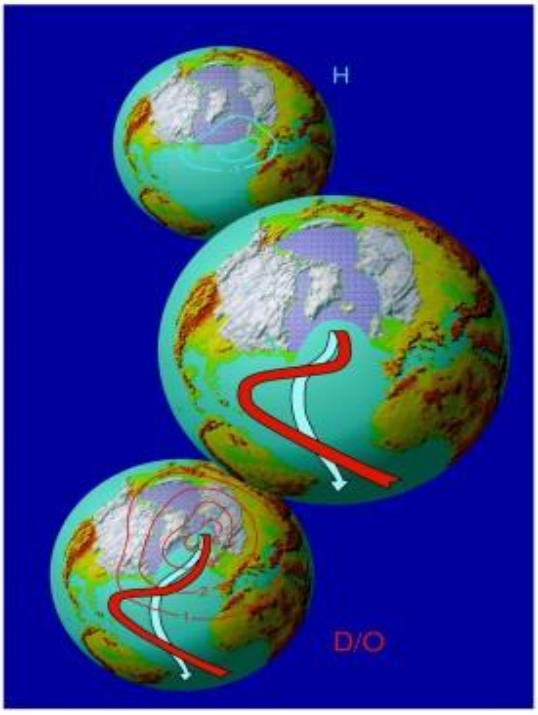

Figure 2.4: Illustration of three stages of North Atlantic Deepwater (NADW) formation and how it reacts to D-O cycles. Top: complete shutdown of NADW formation and sea ice extends far to the south in NH (Greenland Stadial). Middle: Normal NADW formation during glacial times. Some NADW formation and consecutive heat transport (prevailing cold mode (Rahmstorf, 2006)). Bottom: D-O event, Greenland interstadial. Higher transport of heat and surface water to NH and thereby higher NADW formation (Rahmstorf, 2006).

2.2 Thermohaline Circulation

The Thermohaline Circulation (THC) is the term for the large ocean current system, also called the ocean conveyor belt (Rahmstorf, 2006), which ventilate all the major ocean basins on our planet (fig. 2.5). As the name suggests it is a circulation system driven by density, which is controlled by temperature and salinity. Density variations in the THC occur as a result of evaporation, precipitation, sea ice formation, glacial melting and river outwash (Kuhlbrodt et al., 2007). In short, the THC transports warm saline surface waters to the northern high latitudes, with the North Atlantic Current. The heat transport is a key factor in maintaining higher than average temperatures in North-western Europe, compared to similar latitudes. When surface currents reach the northern high latitudes, they lose heat and become colder. Due to surface cooling, and the increased salinity from brine rejection, this surface flow becomes denser (Rahmstorf, 2006). Due to higher density the water then sinks and flows down

to the bottom and is transported towards equator and then to the Southern Ocean. This downflow of water mass is called North Atlantic Deep Water (NADW) formation. Along the way NADW is mixed with water masses from the Southern Ocean, the Antarctic Intermediate Water (AAIW). From Antarctica surface currents flow into the Pacific Ocean towards the equator and to the Indian Ocean. Deep and bottom currents also flow from Antarctica into the Indian and Pacific Ocean.

During glacial periods, The NADW formation has most likely slowed down due to larger freshwater input in the North Atlantic Ocean (Manabe & Stouffer, 1997), and the amount of heat transported to the northern high latitudes has dramatically reduced, but some heat transport has been maintained (Rahmstorf, 2006). Based on the bipolar seesaw hypothesis (Broecker 1998; Stocker and Johnsen 2003) it has been suggested that the heat that is normally transported to the northern high latitudes is reduced and that this could be one of the causes for the sudden decrease in temperature in the NH (North Greenland Ice Core Project Member, 2004). When the heat transport from equator to the northern latitude's halts, heat remains pools near equator and flows south to Antarctica and the Southern Ocean (Crowley, 1992; Stocker et al., 1992)

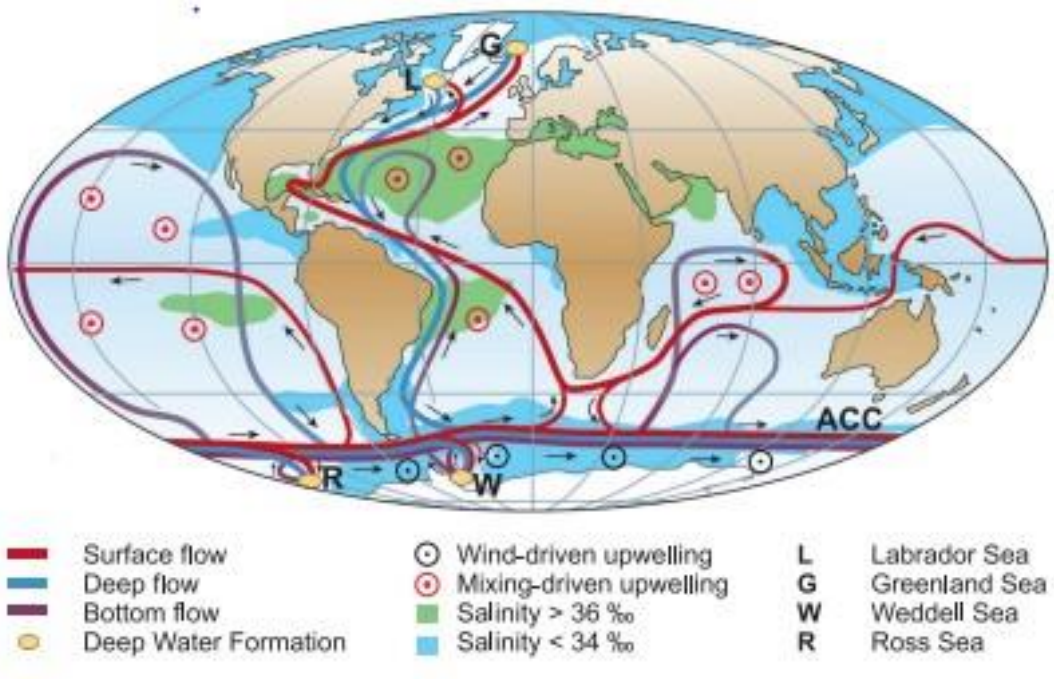

Figure 2.5: Simplified overview of the Thermohaline Circulation (THC). Surface currents are shown in red, deep waters in blue and bottom waters are shown in purple. Deep Water Formation zones are shown as yellows circles. Upwelling (wind-driven in grey and mixing-driven in red) regions are also marked. Salinity, with high saline waters in green and low saline water in light blue. After Rahmstorf. (2006).

3. Introduction to the study area

3.1 Geographical setting

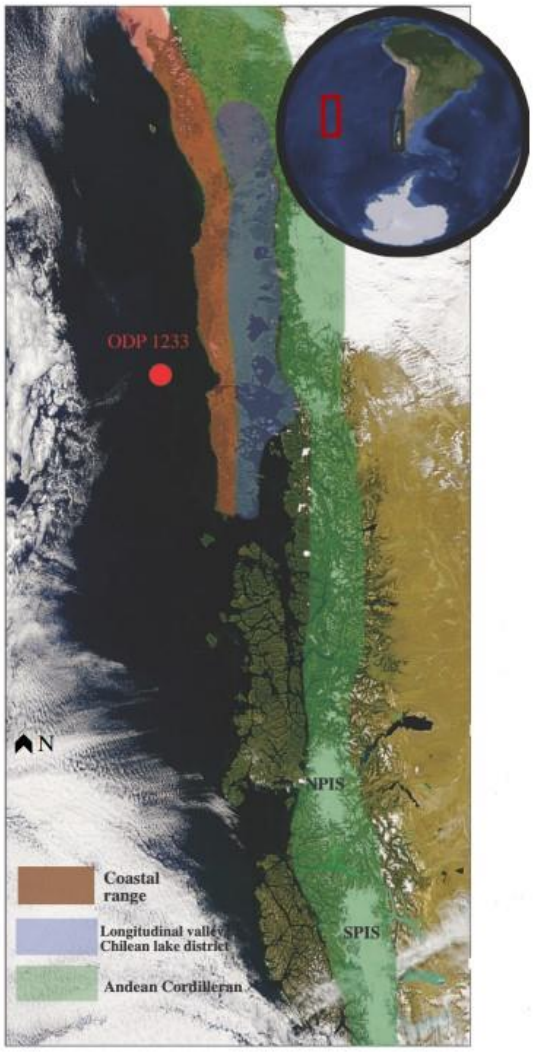

Figure 3.1: Map of Chile and the location of ODP Site 1233. Marked in green shading is the Andes Mountain range. In blue shading, the Longitudinal Valleys and the Chilean Lake District. To the west lies the Coastal Range marked in Red/brown shading. The location of ODP Site 1233 is marked with a red circle just west of the Coastal Range. Modified by Damm-Johnsen (2019) from NASA (2014).

ODP Site 1233 is located in the Southern Hemisphere, off the western coast of Chile, on the South American tectonic plate (41° 0.005' S, 74° 26.992' W, 838 m.b.s.l). The core Site is close to the Nazca subduction zone, which means that the Chilean margin is an active margin. On land, to the east of ODP Site 1233 one can observe the Andes Mountain Range, which spans the eastern coast of South America for 7000 km (fig. 3.1) (Ackert Jr et al., 2008). Between

38˚S and the tip of the continent at 56˚S is the region named Patagonia located. The highest mountains are in the north, and the relief decrease towards south (fig. 3.1). West of the Andes lies the Chilean longitudinal central valley and the Chilean lake district (fig. 3.1), further west, close to the Pacific Ocean, we can trace the Coastal Range (fig. 3.1). The Andes Mountain range has Iron (Fe) rich bedrock, while the Coastal Range is low in Fe (Lamy et al., 2001). The coastal range is mainly made up of low-grade metamorphic rocks (Thornburg & Kulm, 1987). The Longitudinal Valley consist almost entirely of alluvial sediments. High rainfall in this region causes rivers to have a large erosion potential (Galli-Olivier, 1967).

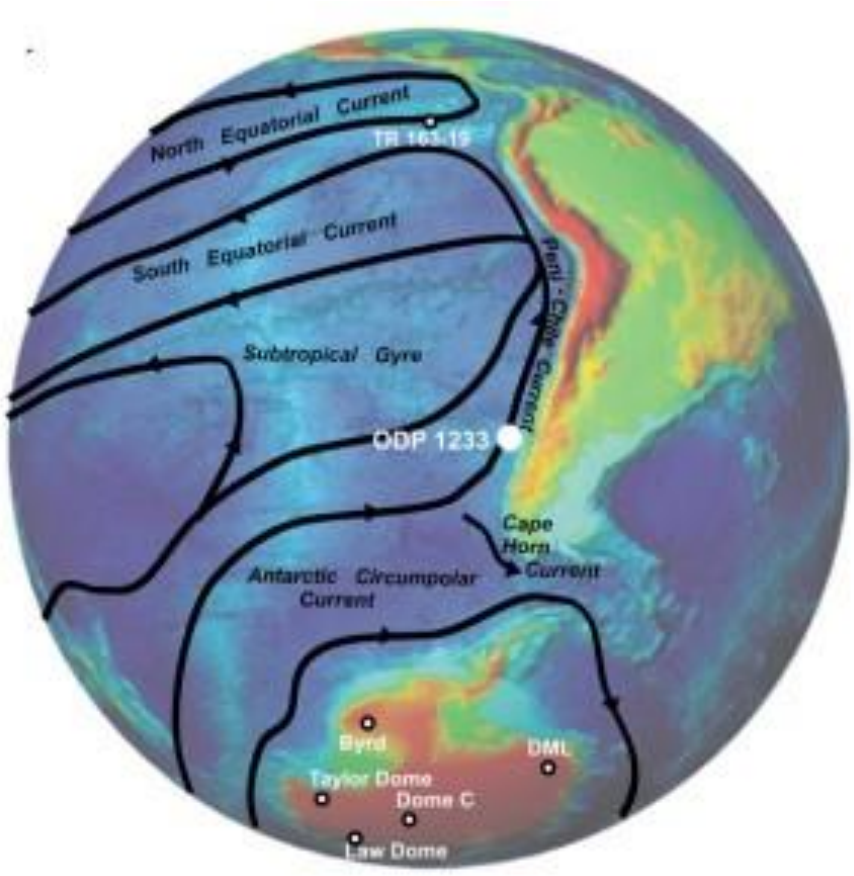

Figure 3.2: Overview of the ocean current system near ODP Site 1233. South 1233 is the Antarctic Circumpolar Current (ACC), that flows around Antarctica uninterrupted. To the northwest of Site 1233 is the location of the Subtropical Gyre. ODP Site 1233 is located in the Peru Chile Current which breaks off from the ACC when it hits Patagonia. After (Lamy et al., 2007).

3.2 Climatic Setting

The climate at ODP Site 1233 is heavily influenced by Antarctica, and past fluctuations of the Antarctic Ice Sheet (AIS). AIS influences climate on seasonal scale all around the globe (Ferrari et al., 2014), and the sea surface temperatures of the coast of Chile have a very steep temperature gradient due to influence of the Antarctic Circumpolar Current (ACC) close to ODP Site 1233 (Levitus & Boyer, 1994). The Chilean coast also has one of the largest precipitation differences in the world. In the north, dry desert-like climate dominates, while the southern region experience rainfall up to 7000 mm/yr because it is presently in the core of the South Westerly Wind (SWW) belt (Mohtadi et al., 2005). This high precipitation and steep temperature gradient are mainly due to the Southern Westerlies hitting the Chilean coast (Heusser, 2003).

The SWW has a large impact on climate and has an annual mean centre around 50˚S (Kaiser & Lamy, 2010). SWW storm tracks seem to have the same activity in summer as in winter (Trenberth, 1991). During austral winter, as the SWW belt moves southward, the precipitation moves with it. The SWW belt is controlled by the subtropical high pressure and the circum-Antarctic low pressure (Kaiser et al., 2007). Because of the impact of the AIS, and from the ocean currents around Antarctica, variations in the positioning of SWW should easily be detected at ODP Site 1233, making its position ideal for studying past climate variability (Kaiser et al., 2005; Lamy et al., 2004). During austral summers the SWW moves southward, increasing the wind intensity, while in austral winter, the SWW moves northward, decreasing the wind intensity (fig. 3.3) (Lamy et al., 2010).

The evidence from hyper humid vegetation pollen in North Patagonia implies that SSW belt migrated northward during glacial times (L. Heusser, Heusser, & Pisias, 2006). Another large contributor to climate variations near ODP Site 1233 is the El Nino-Southern Oscillation (ENSO) (Rutllant & Fuenzalida, 1991). During the El Nino phase of ENSO, SWW shifts towards the equator due to weakened subtropical high increasing cyclonic activity in Chile between 30˚S and 41˚S (Montecinos & Aceituno, 2003). This increases precipitation in the north—in the drier areas of Chile, while southern parts experiences lower precipitation (Montecinos & Aceituno, 2003; Schneider & Gies, 2004). During La Nina the anomalies in Chile are reversed (Blanco et al., 2002).

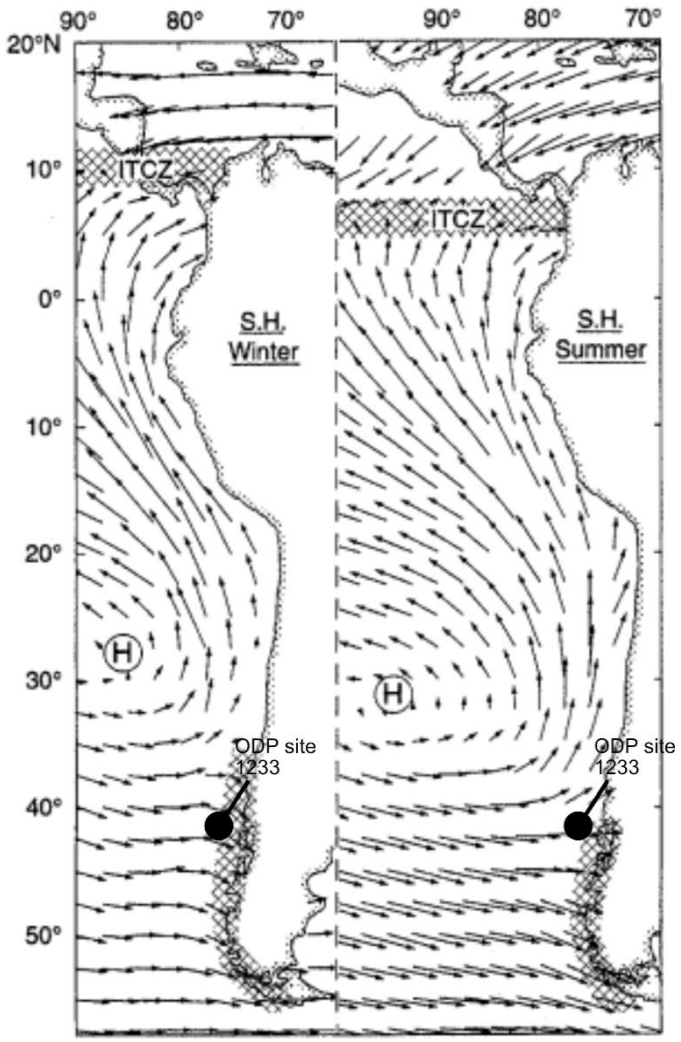

Figure 3.3: Representation of how the SWW and the positioning subtropic high changes from austral summer to austral winter along the Chilean and Peruvian coasts. The left panel shows the austral winter where the Subtropical High moves north toward equator and enlarges region of large precipitation in Patagonia at the south tip of South America. The right panel shows the austral summer, where the Subtropical High moves southward and further from land. This moves the SWW belt south, but it increases in intensity. After Strub et al. (1998)

Southern Annular Mode (SAM) (also Antarctic Oscillation) is another large-scale oscillation affecting the climate in Patagonia. SAM affects the positioning of the westerlies, and during its positive phase there is a poleward expansion resulting in weakened westerlies between 40˚S and 50˚S (Moreno et al., 2018). During a SAM positive phase, climate in Patagonia is

generally warm and dry, while cold and wet climate dominates during negative phase (Quade & Kaplan, 2017).

3.2.1 Frontal movements

The Coast of Chile is strongly affected by the positioning of the fronts around Antarctica (Markgraf et al., 1992) (fig. 3.4). These frontal systems are controlled by the extent of the Antarctic Ice sheet (Gersonde & Zielinski, 2000). A larger ice sheet also broadens the frontal positioning. The first front encountered from north to south is The Subtropical Front (STF) (fig. 3.4). This intersects Chile between 42˚S and 38˚S depending on the season (moves south during summer, and vice versa). STF is controlled by winds generated by the differences in the Subtropical High pressure and the Antarctic low pressure. STF is also a boundary between warm and saline water, and cold and nutrient-rich waters.

With a steep N-S gradient in temperature and a larger displacement between summer and winter the STF is a major climate boundary in SH. During glacial periods, the STF moves further north (Bard & Rickaby, 2009). The position of ODP Site 1233 is ideal for studying climate change in past because of the steep N-S temperature gradient and the effect the changing frontal system has one the climate in the region.

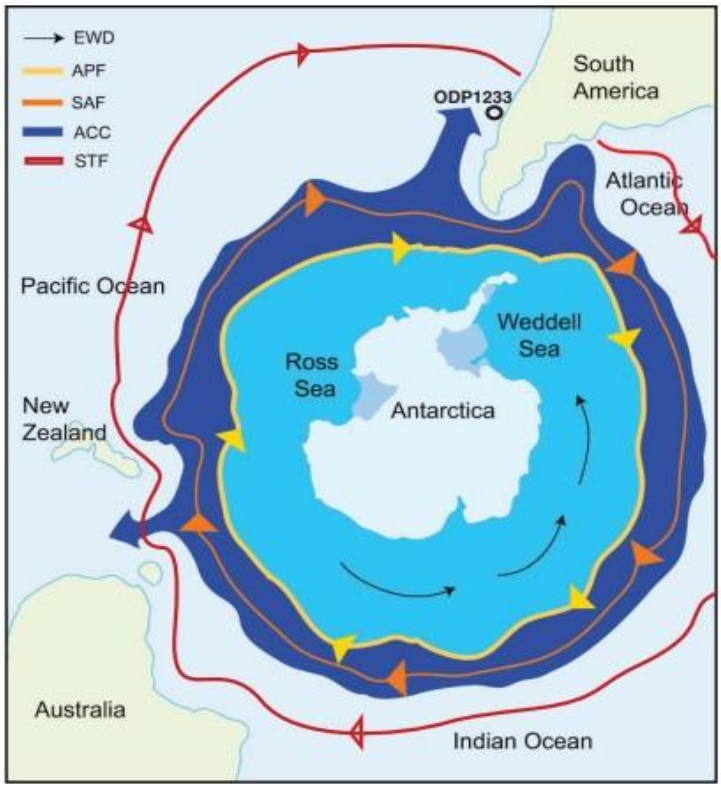

Figure 3.4: Simplified views of the frontal system surrounding Antarctica which also affects the climate observed at ODP Site 1233. ACC is coloured in dark blue with the Sub Antarctic Front (SAF) in orange. The Antarctic Polar Front (APF) separates ACC from the East Wind Drift (EWD) close to the Antarctic. Notice the two arrows showing flow of ACC into Pacific near Chile. After (Beers & Jayasundara, 2015)

3.3 Oceanographic setting

3.3.1 Water Masses

Surface water masses

The northern hemisphere has large continents surrounding the polar basin, partly isolating the Arctic Ocean, while the Southern Ocean has no large land barriers blocking the ocean and wind system, leading to strong wind and ocean currents around Antarctica, partly isolating the continent. The strong ocean currents surround Antarctica, the Antarctic Circumpolar Current (ACC), is strengthened by the wind systems around Antarctica.

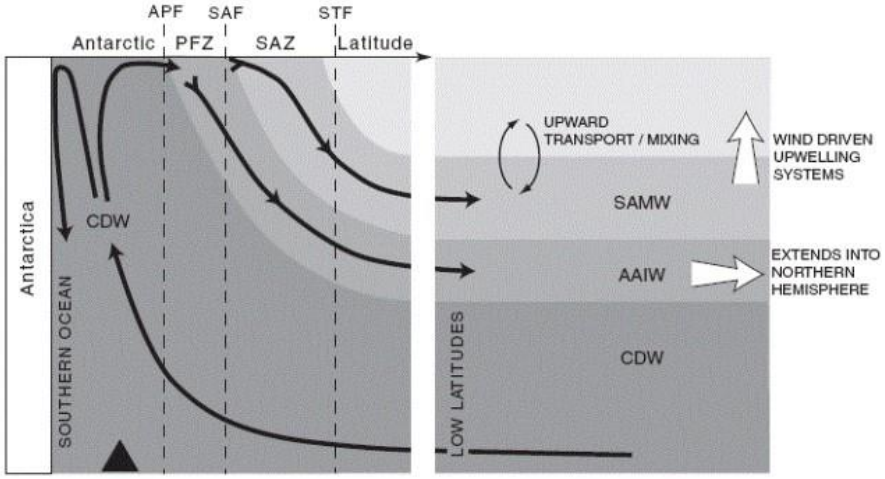

Figure 3.5: Simplified cross section of the Southern Ocean from the coast of Antarctica to the left and northward to the right. APF, SAF and STF shown with dotted lines. At the bottom, of the plot, the Circumpolar Deep Water (CDW) is transported from north and upwells near Antarctica due to wind-driven upwelling. Upwelled CDW is then transported north of the APF where AAIW formation occurs, and it is then transported northwards. North of the AAIW formation area and north of the SAF, is the formation area for Southern Ocean Mode Waters (SAMW) which sinks to intermediate levels but upwells further north due to mixing and wind. (Anderson et al., 2009)

Today, the ACC intersects the Chilean coast between 45˚S and 50˚ S, just south of ODP Site 1233 (fig. 3.6). This brings cold and nutrient rich subantarctic surface waters to the southern coast of Chile. Between 40˚ S and 45˚ S the ACC splits in two (fig. 3.6), the Cape Horn Current (CHC), which flows south and is part of the subpolar system (fig. 3.6), and the Peru-Chile Current, flowing northward as part of the subtropical gyre of the South Pacific (fig. 3.6, fig. 1.7) (Lamy et al., 2007). The intercept point of ACC, where it splits into two currents is

controlled by the position of the SWW (Hebbeln et at., 2000; Mohatdi and Hebbeln, 2004; Lamy et al., 2004). In the Chilean Fjord System, Chilean Fjord Waters (CFW) is transported north (fig. 3.6). This generally has a lower salinity than the nearby ACC because of the runoff from the Chilean rivers (Dowdeswell et al., 2016). ODP Site 1233 is situated (fig. 3.6) close to CFW which makes the surface waters less saline. This, however, makes this site once again ideally positioned to monitor changes in runoff from the Chilean mainland.

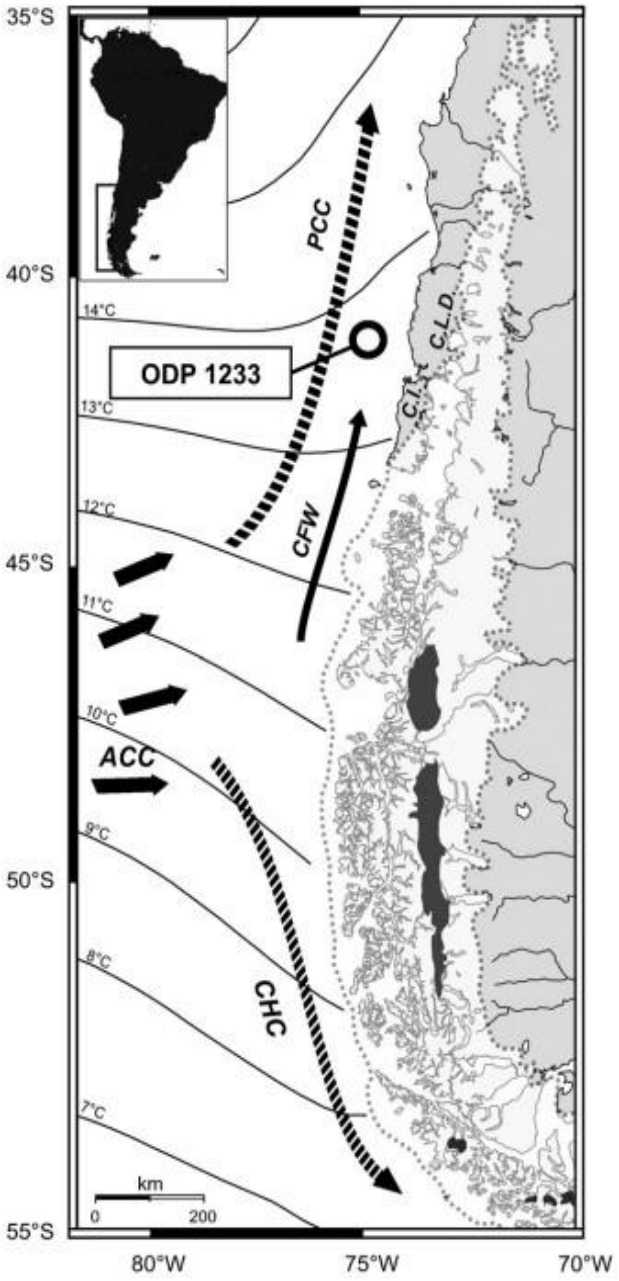

Figure 3.6: Representation of Surface water masses near the Chilean coast. ACC intercepts the coast from west and splitting into two currents. The northward flowing PCC and the southward flowing CHC transports water separates ways. CFW also moves northward with PCC near and at ODP Site 1233. Light gray shading represents the PIS reconstructed extent during the last glacial period. Dark grey shading represents PIS system today. ODP Site 1233 marked with black circle. After (Kaiser et al., 2007).

Intermediate water masses

The intermediate water masses with the largest extent globally is the Antarctic Intermediate Water (AAIW), which spreads into all the major oceans in SH and also spreading into the NH ocean basins in both the Atlantic Ocean and the Pacific Ocean (Figure 3.7). AAIW originates from the Polar Front Zone (PFZ) (Fig. 1.9) and is normally found between Circumpolar Deep Water (CDW) and Sub Antarctic Mode water (SAMW) in the Southern Ocean. Major AAIW formation occurs near the coast of Chile (Talley, 1999). From Antarctica and the Chilean Coast AAIW is subducted into the subtropical gyre (Talley, 1996). AAIW fills a large part of the global ocean and is the dominant water mass at depths between 800 m.b.s.l. and 1000 m.b.s.l. south of equator. ODP Site 1233 is situated at 838 m.b.s.l., right in the core of the AAIW. A common signature that distinguishes AAIW from other intermediate water masses are high silica values (Tsuchiya, 1989).

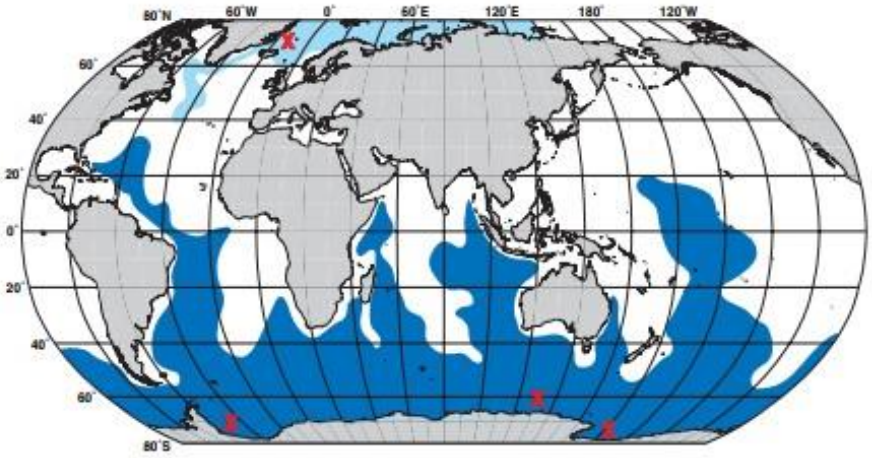

Figure 3.7: The spread of AAIW and North Atlantic Intermediate Water in the world's ocean. Dark blue represents AAIW spread. AAIW reaches furthest in the Atlantic, about 30N. Light Blu is North Atlantic intermediate waters. Red X's represents areas of intermediate water formation, in the Arctic and Antarctic regions. Modified after (Rahmstorf, 2006; L. D. Talley, 1999)

Upwelling

Oceanic upwelling occur when water from the deeper ocean rises to replace surface water which has been displaced, This upwelling process is known as Ekman transport, and it's driven by the Coriolis effect which set the water masses in motion perpendicular to the wind direction (to the left on SH, and right on NH) (Ekman, 1905). The SWW intercepts the Chilean coast

and is forced northwards and the accompanying Ekman transport pushes water from the coast, allowing deep-water to upwell to the surface. There are sites of coastal upwelling areas north of 1233, but where the deep-water originate from is still debated. Both AAIW, from the south, and the Gunther Undercurrent, from the north, have been suggested as sources (Mohtadi et al., 2008).

δ^{15}N measurements from Site 1233 suggests a southern source, favouring the AAIW as source water in the upwelling region (Martinez et al., 2006). On the other hand, Morales et al. (1996) claims that the northern regions of Chile have a northern source for upwelling, but also observes lower δ^{15}N values further south.

The upwelling supplies cold, fresh, and nutrient rich deep waters to the coast of Chile, which results in a region known for its high marine productivity (Berger et al., 1989), that plays an important role the rich fishing industries in the country (Alheit and Bernal, 1993). During the LGM, ODP Site 1233 experienced mostly onshore wind, and little upwelling has been observed during this period (Romero et al., 2006). Due to global warming, the SWW now have a slowly southward moving trend which can lead to a shift in the upwelling areas with a move towards upwelling further south, near the core site of 1233 (Aguirre et al., 2018).

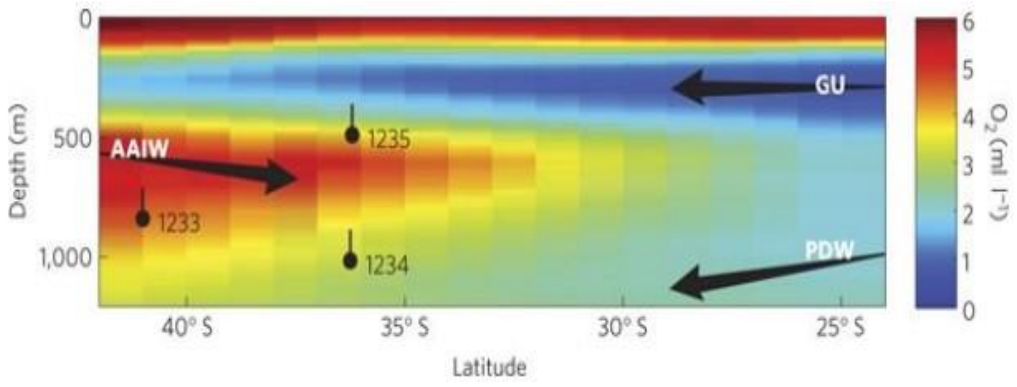

Figure 13.8: Stratigraphical profile of the dissolved oxygen content of the principal water masses in the ocean west of Chile from 40˚S to 25˚S. Oxygen-rich waters are red, and blue is oxygen-poor. From the North flows the Gunther Undercurrent (GU) at intermediate level and the Pacific Deep Water (PDW) flows at deeper water levels. From the South, AAIW, lies between the two northern source water masses. The black dots are locating ODP Sites 1233, 1234 and 1235 depths and the vertical lines on the black dots indicate the influence of the 130m sea level drop during LGM. From Muratli et al. (2010).

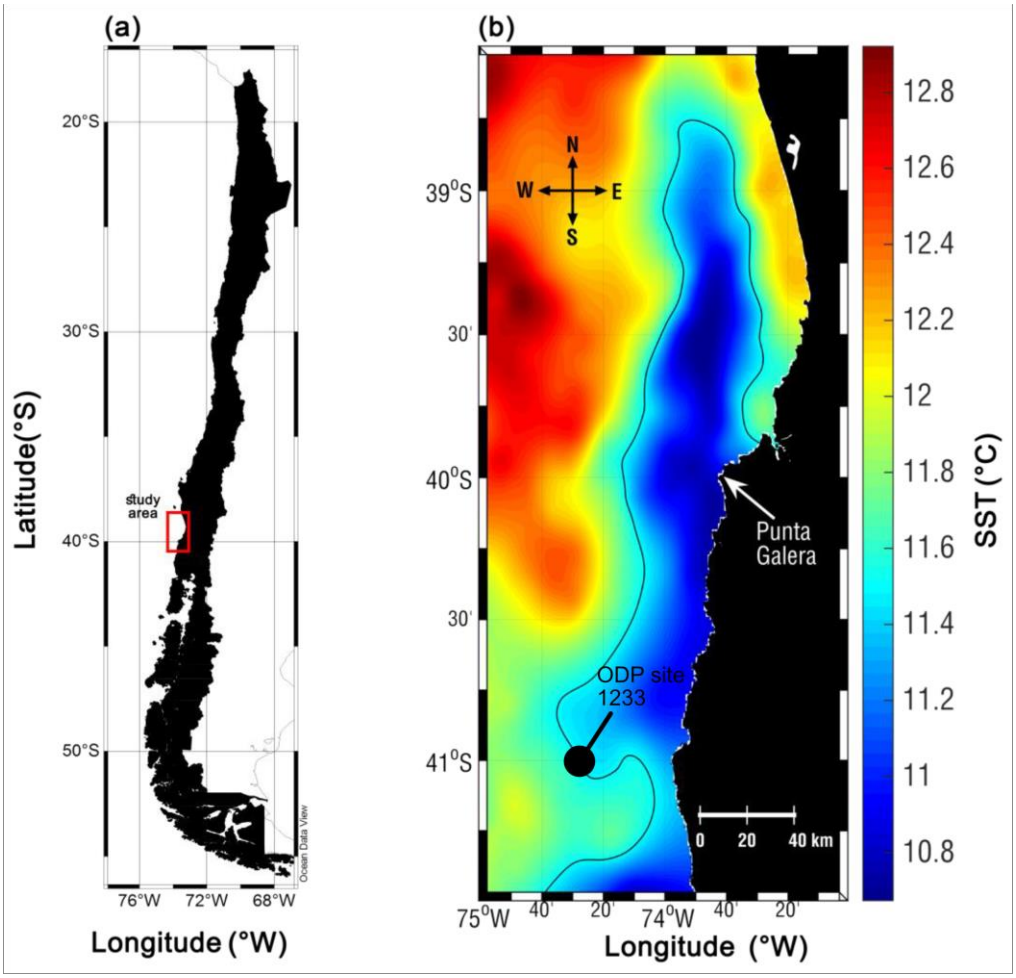

Figure 3.9: The right panel in this figure shows regions of large-scale upwelling shown with temperature deviation. Cold freshwater masses which upwell outside the coast of Chile is naturally much colder than the surrounding surface water due to long residence in the deep sea. Cold water is marked blue and warmer water is marked in green to red. The left panel is a large map where the upwelling area is marked with a red square. ODP Site 1233 is located at 41˚ 00'S;74˚ 27'W, just south of where the upwelling is most prominent. After (Pinochet et al., 2019).

3.4 The Patagonian Ice Sheet

The Patagonian Ice sheet (PIS) is one of the largest glaciers in the world, after the AIS and the Greenland Ice Sheet. Today it is a system of four glaciers, the Northern Patagonian Ice sheet (NPIS) from 46.4˚S to 47.5˚S, the Southern Patagonian Ice Sheet (SPIS) from 48.3˚S to 52˚S, the Gran Campo Nevada at 52.8˚S and the Cordillera Darwin icefield at 54.5˚S (Davies et al., 2020). In total, the Patagonian glacial system covers a total area of 22.718 km^2 (Davies &

Glasser, 2012) and a total volume of 5955±1191 km^3 equivalent to 15.1 ± 3.0 mm of sea level change (Carrivick et al., 2016). The Patagonian glacier system is the biggest temperate glacial system in the world. PIS is unique for its placement, e.g., normally glaciers thrive at much higher latitudes, but due to the wind system and precipitation increased by orographic precipitation, the PIS glacial system has been able to survive in relatively mild temperatures.

Given its placement in the SWW belt, the PIS has been studied extensively for the last decades. It has been suggested that mid latitude glacial systems are more prone to changes caused by global climate rather than regional climate (Boex et al., 2013). Changing climate can therefore be easily observed by retreat and advance of PIS, because precipitation is an important factor for PIS (Boex et al., 2013). Reconstructions from observed moraines from the PIS extent during the Last Glacial Maximum (LGM) indicates that a rapid retreat happened during Termination 1 (Denton et al., 1999; Garcıa et al., 2018; Hulton et al., 2002). The retreat happened at the same times as the SWW belt shifted southwards (Lamy et al., 2007; Moreno et al., 2015), thus transporting less moisture to the coast of Chile. This confirms that a southward shift in SWW belt leads to retreat of PIS, and due to PIS being temperate and fast flowing, retreat occurs over a short period of time (Lamy et al., 2007).

Today, the glacial system in Patagonia is experiencing rapid retreat due to a temperature increase of 0.5° C over the last 50 years (Pürtner et al., 2019). Modelling done by Hulton et al. (2002) suggest that PIS is very responsive to change in sea surface temperatures. The north-western part seems to be especially sensitive to temperature fluctuations (Lamy et al., 2004). The increasing temperature does not only cause melting, but precipitation falling like rain instead of snow is increasing as well (Rasmussen et al., 2007), reducing the accumulation of snow in the winter. Because of its size, the melting of PIS contributes to the global sea level rise, but nothing like the contribution from Antarctica and Greenland.

3.4.1 PIS during the last glaciation

During the last glaciation, PIS was a large glacier stretching 1800 km from 41° S to 56°S (Fig. 3.10). It is assumed that most of PIS south of the ODP Site 1233 terminated in the Pacific at the continental shelf (fig. 3.10). North of the Chilean Fjord System, PIS most likely terminated on land, and to the east in also terminated inland with glacial arms filling the valleys in the

east of Patagonia. During MIS 3 it has been observed that PIS had large variations (Kaiser et al., 2007). These large variations were caused by large scale climate variations causing the SWW belt to shift depending on temperature and climate (Darvill et al., 2015a; Garcia et al., 2018). Due to the shifting of SWW, the NPIS and SPIS had different timing for when they had their largest extent (Kaiser et al., 2007). SPIS most likely had its maximum during 48 Kyr BP during MIS 3 (Darvill et al., 2015b; Garcia et al., 2018) with SWW placed more southwards, while NPIS reached its maximum close to LGM (Kaplan et al., 2008). This suggests wetter climate near NPIS and drier closer to SPIS suggesting that SWW had a more northwards placement during LGM. During Termination 1 and MIS 4, PIS observations suggest a time lag between climate change and PIS retreat (Lamy et al., 2004), however during early MIS 3 the lag time is not observed, and fluctuations is almost synchronous with SST when PIS was much smaller than during LGM (Kaiser et al., 2007). Kaiser et al. (2007) even suggest that northern parts of PIS was absent during the early part of MIS 3.

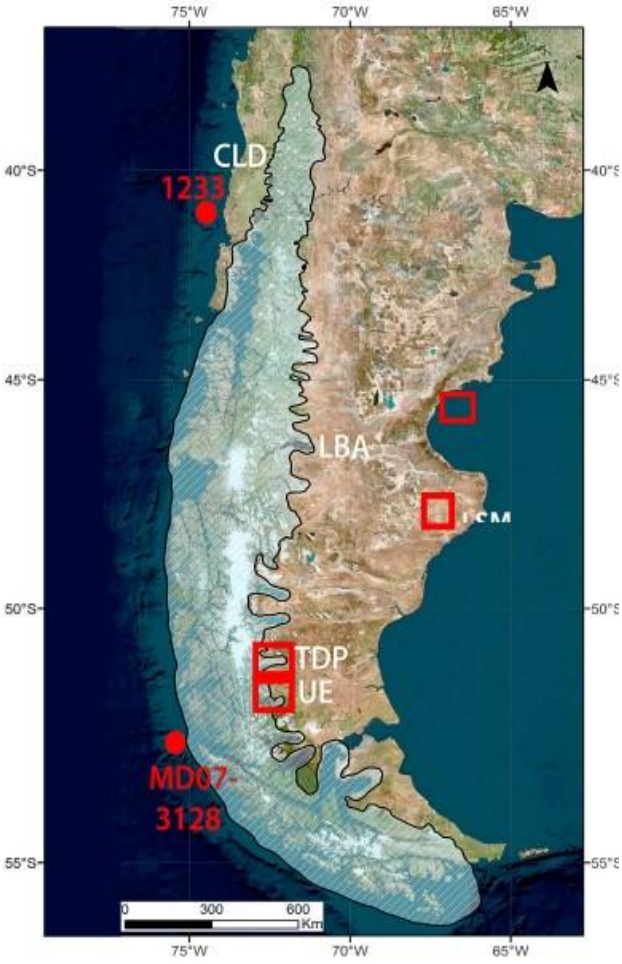

Figure 3.10: Illustration of the maximum extent of the Patagonian Ice Sheet (PIS) during LGM. PIS stretched ca 1800 km all the way south to Cape Horn on Tierra del Fuego. In the east PIS terminated on land in the valleys near the border between Chile and Argentina. In the west PIS mostly terminated in the ocean at the continental shelf, but also on land in the north. Torres del Paine (TDP) and Ultima Esperanza (UE) to the south, two valleys where end moraines have been studied. Location of ODP Site 1233 and Site MD07-3128 marked with a two red dots. After Garcıa et al., (2018)

PIS during A2

During A2 the SWW had a more southward placement, and Darvill et al. (2015) and Garcıa et al. (2018) argues that this has led to a SPIS maximum at 48 Kyr BP. A glacial advance based on a boulder sampled from Torres del Paine, valley in Argentina at the eastern termination of SPIS, using cosmogenic ^{10}Be exposure age, is dated to 43.7(± 1.9) Kyr BP (Garcıa et al., 2018). Two older boulders from Ultima Esperanza, a valley to the south of Torres Del Paine, has been dated to 49.5 (±2.4) Kyr BP with cosmogenic ^{10}Be exposure ages (Garcıa et al., 2018). Garcıa et al. (2018) interpreted these boulders to be a glacial advance at 48.0 (±1.6) Kyr BP. A later advance has been proposed at ca 45.6 Kyr BP in Rio Cullen, however this date comes with greater uncertainty (Darvill et al., 2015).

4. Material and methods

This chapter focuses on the process of preparing the samples for planktonic foraminiferal assemblage counts, lithic counts, and stable isotope analyses. Furthermore, the tools and analytical equipment used will be described. During the microscopy work, every planktonic foraminifer shell was identified and counted from the split samples, and this chapter will also provide a short introduction of the chosen foraminifera species and a rationale for selecting these species for further analyses. The microscopy laboratory at the Department of Earth Sciences at UoB was used for the planktonic foraminifera and IRD counts, and the FARLAB (Facility for advanced isotopic research and monitoring of weather, climate and biogeochemical cycling) was used for the stable isotope analysis.

ODP Site 1233

ODP Site 1233 was drilled as a part of the ODP Leg 202 expedition off the coast of southern Chile, near the Chilean fjord region. ODP, short for Ocean Drilling Program was a former phase of the current International Ocean Discovery Program. Site 1233 was drilled 38 km offshore, at 41°0.01'S 74°26.99'W. The drill site is in a small forearc basin on the continental slope and was drilled at 838 meters water depth. Sedimentation rates at the site location is estimated to be on average 100cm/ky (Shipboard Scientific Party, Leg 202, Chapter 4, 2003) which makes it ideal for high resolution climate reconstruction. Despite the high sedimentation rates at Site 1233, the site had an abundant microfossil fauna (Shipboard Scientific Party, Leg 202, Chapter 4, 2003) making it ideal for detailed studies. The site consists of four drill holes, 1233A, B, C and D from which a composite core a splice was generated to obtain full recovery down to 134 meters below sea floor.

4.1 Lithostratigraphy

The 136-m thick spliced core sequence from ODP site 1233 consists of a single lithological unit (Unit 1) defined based on visual core descriptions and smear slide analysis and is primarily dominated by clay and silty clay with varying amounts of calcareous nannofossils (Shipboard Scientific Party, Leg 202, Chapter 4, 2003). There are some rare interbedded

minor lithologies, including thin silt-rich layers and volcanic ash layers. High mean magnetic susceptibility below ~10mcd (below Holocene) are consistent with higher sedimentation rates and increased terrigenous sediment during the last glacial interval (Shipboard Scientific Party, Leg 202, Chapter 4, 2003). Quartz is highest at the top (~10), but decrease downcore, where feldspar increases, indicating increased terrigenous input from feldspar-rich volcanic rock from the Andes during the last glaciation (Shipboard Scientific Party, Leg 202, Chapter 4, 2003). Foraminifera, nannofossils and diatoms are abundant in the whole core (Shipboard Scientific Party, Leg 202, Chapter 4, 2003). The dominant lithology of Unit 1 is homogeneous nannofossil clay, nannofossil silty clay and nannofossil-bearing silty clay. Sediment colour ranges from dark olive-grey to dark grey (Fig. 4.1; Shipboard Scientific Party, Leg 202, Chapter 4, 2003).

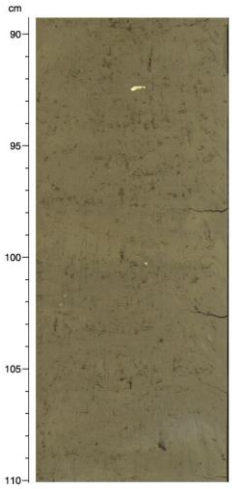

Figure 4.1. A representative interval showing the major lithology at Site 1233 (interval 202-1233-8H-5, 90-110 cm). Sediment colour ranges from dark olive grey to dark grey. (Shipboard Scientific Party, Leg 202, Chapter 4, 2003).

4.2 The Meters Composite Depth scale

Five boreholes at ODP Site 1233 were drilled using the advanced piston corer (APC) and a total of 135.73 meters of sediments were recovered, from which a composite depth scale, MCD, was generated (Shipboard Scientific Party, Leg 202, Chapter 4, 2003). The abbreviation" mcd" stands for "meters composite depth". When cores are recovered from the sea floor, a varying quantity of sediment is usually lost between the sections of each 9.5 meter

of core that is recovered because of ship heave. How much depends on the drilling conditions, but it is usually only a fraction of the volume of the sediment recovered, ranging from the equivalent of a few centimetres to a few meters of sediment. To overcome this, several boreholes are drilled and the correlation of the five cores at Site 1233 was done by correlating the magnetic susceptibility signal from each hole and splice in missing segments between the holes (Shipboard Scientific Party, Leg 202, Chapter 4, 2003). This means stratigraphically correlating and depth shifting cores relative to each other. The final splice avoided sediment disturbances at the top and bottom of each core which could have affected the reconstruction and interpretation of the proxy data down core. During the splicing, none of the core signal were stretched or squeezed. The MCD is based on stratigraphic correlation of whole-core Oregon State University (USO) Fast Track Magnetic Susceptibility data (OSUS-MS) collected shipboard at 5 cm depth intervals using 1-s integration times (Førde, 2008).

4.3 Laboratory work

ODP Site 1233 samples for this thesis were selected with 8 cm spacing, from 75.79 to 83.65 mcd. The sample spacing was sometimes changed to exclude samples that were previously used for stable isotope analyses (where high numbers of planktonic foraminifera were picked out) in order not to affect the planktonic foraminiferal assemblages (see Appendix). The spliced section from 75.79 to 83.65 mcd contains data from holes 1233B and 1233D. Sample preparations (drying and weighing bulk sediment samples, wet sieving, and moving the samples into sample glasses) were already done prior to this thesis at the sediment facilities of the Earth Surface Sediment Laboratory (EARTHLAB) at the Department of Earth Sciences, University of Bergen. The samples were first dried at 50◦C for approximately 24 hours to obtain the dry bulk weight, after which the samples were soaked in distilled water and left on a shaking table for 12 hours. Samples were then wet sieved into fractions (>63µm) and weighed again to prepare them for microscopy work.

4.3.1 Planktonic foraminiferal assemblages and lithic counts

Planktonic foraminiferal assemblages and lithic (IRD) counts were done using the >150 µm sample fraction. For this thesis project, only the planktonic foraminifera species were identified and counted. Benthic foraminifera were counted only to obtain the percentage of

the overall benthic assemblage for calculating IRD abundance. Lithic (Ice rafted debris, IRD) grains were counted, and the relative abundance (%) of IRD was derived from the counts of total foraminifera (planktonic and benthic) and IRD grains. The identification of planktonic foraminifera is done under a Leica stereomicroscope. The bulk dry sample (> 63 µm) was first dry sieved using a 150 µm-fraction sieve. To obtain the ideal 300 planktonic foraminifera count the sample was split and the number of splits was determined upon the sediment size. The sub sample was sprinkled evenly over a gridded picking tray and examined using the stereomicroscope. The number of counted foraminifera varied between 175 for a whole sample to 500 for a sample that was split multiple times. Every identifiable planktonic specimen was counted, and unidentified species were marked as ”other species”. A total of 90 samples spanning the 75.79 mcd to 83.65 mcd interval was counted.

The census counts-method for counting and determining foraminiferal assemblages was first tested by the Climate: Long range Investigation, Mapping, and Prediction (CLIMAP)-project (CLIMAP Project Members, 1976; CLIMAP Project Members, 1984) and later improved by the MARGO (Multiproxy Approach for the Reconstruction of the Glacial Ocean Surface) project (Kucera et al., 2005) . Since one gram of deep-sea sediments counts thousands of foraminifera (> 150 µm), quantitative analysis of the sediments to determine environmental surroundings are possible (Kucera, 2007)).

The planktonic foraminifera identified and counted at Site 1233 includes: *Neogloboquadrina pachyderma*, *Neogloboquadrina incompta*, *Globorotalia inflata*, *Glogeigerina bulloides*, *Globigerinita glutinata* and *Turborotalia quinqueloba* mainly, and minor amounts of *Globorotalia truncatulinoides, Orbulina universa, Globorotalia scitula* and *Globorotalia crassaformis*.

Here, samples were not recounted, which might increase the uncertainty of the foraminiferal assemblage and IRD data. Three samples (at 80.26, 83.06, 83.14 MCD) contained <100 foraminifera, and their results should be more carefully interpreted.

Figure 4.2: Counting equipment used in this project. A) Microscope (type) B) Counting tray consisting of 45 squares (1x1 cm). C) Sieve to separate the ≥ 150 um fraction. D) Tray used for moving sample between counting tray, sieve and sample container. E) The splitter used to divide the samples prior to counting (Figure 4.1 in Dahm-Johnsen, 2019).

4.3.2 Preparation for stable isotope analysis

For this study, the epifaunal benthic foraminifera *Cibicidoides wuellerstorfi* was used for stable isotope analysis. For this thesis, previously picked *C. wuellerstorfi* samples (by Kleiven, 2005), were prepared for stable isotope analysis. This included weighing, loading and cleaning the samples, and was done at the FARLAB, Department of Earth Science, UoB. For the

weighing process, C. *wuellerstorfi* specimens between 30 and 60 µg were selected (or, if large, broken into fragments to satisfy weight requirements) and placed in glass vials. Due to the large size of *C. wuellerstorfi* only one, or fractions of one, specimen was required for each analysis. The same samples (a total of 90 samples), which were used for planktonic foraminiferal assemblage and IRD counts, were also used for the stable isotope analysis, whenever possible. When specimens from the same depth were not available, a specimen from the closest adjacent depth was selected. After selection, the foraminifera shells were cleaned by adding a few drops of methanol (CH_3OH) and sonicating in an ultrasonic water bath for 10 seconds. After sonication, the methanol was carefully removed with a modified syringe and then dried in a heating cabinet at 50°C. Once dry, the samples were placed in a metal carousel ready for the Kiel IV automated carbonate device which was attached to the Finnigan MAT 253 mass spectrometer.

A problem that occurred during the runs was that some sample of *C. wuellerstorfi* would float on the acid bubbles created during digestion and be lifted in the vial where they attached to the side of the vials above the acid, resulting in non, or incomplete reaction of the sample. Every sample was carefully examined after each run and samples that had not reacted were rerun.

Standards

For data from a stable isotope analysis to be comparable to other data globally, an international carbonate reference standard is used. An in-house standard calibrated to the international standard can also be used. This standard reference is analysed in the same batch as the samples, in the principle called identical treatment, so samples and standards are treated and analysed as similarly as possible and any secondary influences on their values can be accounted, and corrected, for.

The original standard that defines the international reference scale, Pee Dee belemnite (PDB), is no longer available (entirely depleted). To acknowledge this, a new reference scale Vienna Pee Dee Belemnite (VPDB) was created by the International Atomic Energy Agency (IAEA) (Clark & Fritz, 1997).

One of the standards used for the stable isotope analyses in this study is NBS-18, distributed by the National Institute of Standards and Technology (NIST) and IAEA, a standard reference

used for every stable isotope run at the FARLAB. Another standard that was used is the Carrara Marble 12 (CM12), which is an in-house standard reference. The CM12 is calibrated to VPDB using NBS-19 and NBS-18 whose values are well established against VPDB. NBS-19 is run as a control with each run to assess the post correction, e.g., if the values come out correctly on the VPDB scale. Standards are weighed out to span the same (full) mass range of the samples.

Mass spectrometry

The mass spectrometer at the FARLAB, UoB, has a similar design to the original gas source mass spectrometer design of Nier (1940). The mass spectrometer, Thermo Finnigan MAT 253, consists of three essential parts: a source, a magnetic analyser and an ion collection system (Faure & Mensing, 2005). The mass spectrometer generates CO_2 gas, via an attached device called Kiel IV, when the carbonate samples and standards react with 100% phosphoric acid (H_3PO_4) at 70°C, after the method developed by McCrea (1950). During acid digestion of the carbonate, all carbon is converted to CO_2 and 2/3 of oxygen is converted (Equation 4.1). Any residual water is removed by letting sample gas pass through a tube kept at -80C with liquid nitrogen prior to the gas being transferred to the mass spectrometer.

The mass spectrometer allows a small amount of CO_2 to enter via a capillary inlet which is crimped to insure a turbulent (non-laminar) flow regime is maintained and kinetic fractionation is not introduced as the sample flows to the mass spectrometer. After entering the source, the CO_2 is bombarded with electrons to ionized them, then accelerated by a high voltage (10 Kv) electric field. The magnetic field then deflects the ions proportionally to the mass of the isotopes and ions of different masses (44, 45, 46) are counted by the collector cups.

$CaCO_3 + H_3PO_4 \leftrightarrow CaHPO_4 + CO_2 + H_2O$ Equation 4.1(McCrea, 1950)

Stable Oxygen Isotopes

Stable oxygen isotope analysis focuses on the difference between the lighter isotope ^{16}O and the heavier isotope ^{18}O, denoted $\delta^{18}O$ (Ruddiman, 2001). Foraminifera shells are made of carbonate (CaCO3; in the form of calcite in this case) and their $\delta^{18}O$ values are a common

proxy for paleoclimate reconstructions (Niebler et al., 1999). Foraminifera carbonate shells isotopic composition is a function of both the ambient seawater isotopic composition and the temperature at which calcification occurs. This relationship between seawater and carbonate shells led to the first use of stable oxygen isotope by Urey (1947) and later Epstein et al. (1953) derived an equation (Equation 4.2) for paleotemperature based on $\delta^{18}O$. However, since only modern day $\delta^{18}O$ of seawater is known, past changes in the $\delta^{18}O$ of seawater (local and global) must quantified or inferred before temperature can be determined.

$t(°C) = 16.5 - 4.3\delta + 0.14\delta^2$ Equation 4.2 (Epstein et al., 1953)

Seawater $\delta^{18}O$ varies due to fractionation which occurs during phase transitions (evaporation and condensation) and the transport of water in the hydrological cycle. The lighter ^{16}O is enriched in evaporated water (H^2O), which causes enrichment of the heavier ^{18}O in oceanic areas where there is net evaporation. The fractionation process increases as temperature decreases. The light isotope (^{16}O) is concentrated in precipitation and can be accumulated in snow and ice (formed from precipitation). Thus, the accumulation of large amounts of isotopically light (^{16}O enriched) ice on land (glaciation) leads to enriched ^{18}O values in the ocean (Rosman & Taylor, 1998).

Stable Carbon Isotopes

Stable carbon isotopes, denoted $\delta^{13}C$, reflect the ratio of the two stable carbon isotopes ^{12}C and ^{13}C. Ocean carbon isotopes vary depending on the total dissolved carbon in the ocean, primary production and ocean circulation. The isotopic value of the epifaunal species *C. wuellerstorfi* covaries the $\delta^{13}C$ of dissolved inorganic carbon (DIC) in the bottom water that the foraminifera calcify in (Curry et al., 1988; Duplessy, 1988). However, other (infaunal) species are less reliable recorders of bottom water $\delta^{13}C$ since carbon isotopes decrease within the sediment column due to the respiration of organic matter locally (Cooke & Rohling, 2001). Even epifaunal foraminifera may experience microhabitat influences in extreme productivity regimes (Schmittner et al., 2017)

The $\delta^{13}C$ of benthic foraminifera can record the biological production in the region and the ventilation of water masses. As organic matter preferentially incorporates the lighter ^{12}C

isotope, surface water with high nutrient (and carbon) uptake due to biological production will gradually become enriched in the heavier ^{13}C. When the organic matter is remineralized deeper in the water column the lighter ^{12}C is released back to the water (DIC pool) along with nutrients (Curry et al., 1988), and δ^{13}C of DIC decreases (Rohling & Cooke, 1999). This cycle of ^{12}C makes δ^{13}C values a good tracer of age in the oceans as longer isolation from the surface and gradual accumulation of respired carbon will decrease δ^{13}C. δ^{13}C is also used as a proxy for ventilation of water masses, due to the strong relationship between apparent oxygen utilization (AOU) and the δ^{13}C of DIC in the ocean (Eide et al., 2017).

4.4 Foraminifera

Foraminifera, often called forams, are small single-celled free-living marine animals, eukaryotes, which secrets a solid calcium carbonate skeleton, called tests, which is divided into a series of chambers, which increase in number during growth (Boudagher-fadel, 2015 s.1). Foraminifera appear in the fossil record during the Cambrian period and diversified from only benthic to benthic and planktonic species during the Jurassic period (Boudagher-fadel, 2015 s.4) Today, foraminifera occupy a wide range of marine environments from coastal to deep sea and from the surface to the bottom of the ocean. They are even found in brackish environments (Boudagher-fadel, 2015 s.1) Planktonic foraminifera lives either near or at the ocean surface but can be found down to 500 meters in the water column. Benthic foraminifera lives attached to a substrate at the bottom of the ocean (or in the ocean sediments) and are found at all depths. Foraminifera inhabit the shallow seas and oceans across the whole planet. The long evolution history of the foraminifera and their global spread means that they are of great value in paleoenvironmental, paleoclimatic and palaeoceanographic reconstruction and interpretation. Their calcium carbonate tests form in equilibrium with the surrounding ocean water and capture the prevailing oxygen and carbon isotopic signature of the ocean, hence they provide valuable information about the past climate and environment. Different species of foraminifera also favours different climate. Some species thrive in the cold polar waters, others prefer warm tropical waters, and some prefer regions of high biological productivity in the upwelling zones.

4.4.1 Planktonic Foraminifera

The distribution of foraminifera in the world oceans share similarities with SST gradients, suggesting a strong relationship between SST and planktonic foraminiferal abundance. In this thesis, the foraminifera will be presented after their ecological and geographical distribution in the modern ocean following the provinces outlined in Kucera (2007).

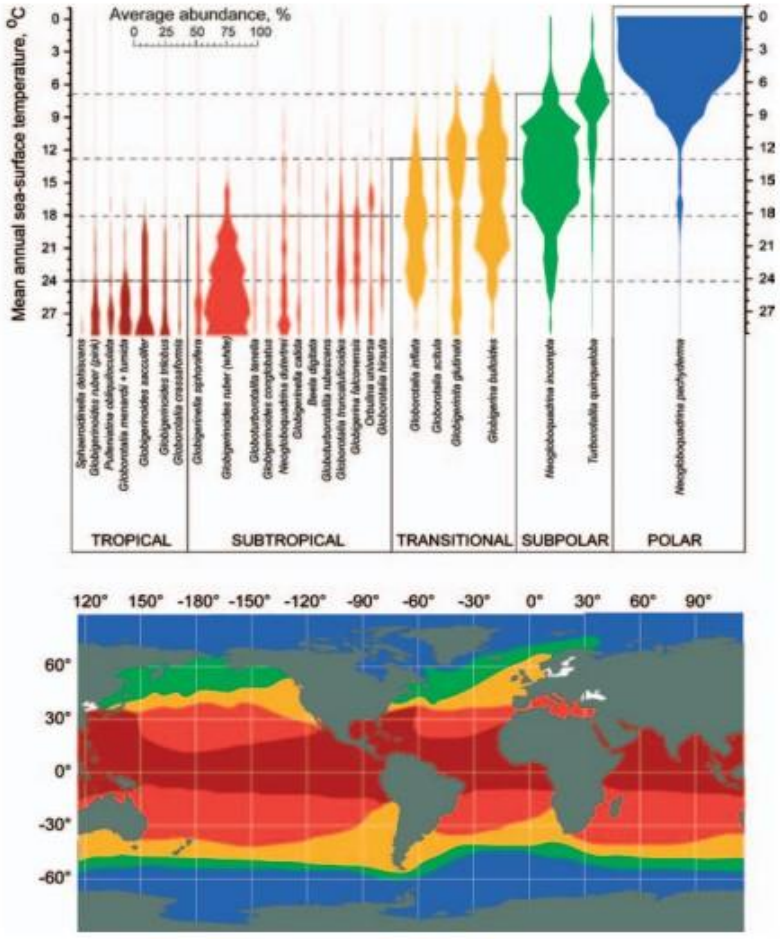

Figure 4.3: Map depicting the five main climatic provinces for average latitudinal distribution of modern planktonic foraminifera and accompanying graph showing the average abundance in % of their distribution in each province. The figure shows where modern planktonic foraminifera species thrive and also, which climate zone they prefer. For instance, the blue colour indicate the high latitude polar climate zones, that are dominated by *Neogloboquadrina pachyderma*, whereas the dark red colour, which is the tropical region, has a much wider spectre of species. Figure from (Kucera, 2007).

Polar species

Neogloboquadrina pachyderma (Ehrenberg, 1861)

Neogloboquadrina pachyderma (hereafter, *N. pachyderma*) is a foraminifer dwelling in the upper parts of the water column of the ocean. *N. pachyderma* is the dominating planktonic foraminifer species in the polar oceans, both the NH and SH, and is almost the only living species of foraminifera in the coldest waters (Kucera, 2007; Tolderlund et al., 1971). It thrives in the Southern Ocean, preferring the colder ocean surface waters and it tends to be dominant up to 12˚C (Niebler et al., 1999). *N. pachyderma* tends to avoid low salinity waters (< 32‰) and in Antarctica it has been observed in sea ice where brine salinities reach >80‰ (Dieckmann et al., 1991; Michael, 1996). *N. pachyderma* is consistently present through the glacial and interglacial cycles during the Quaternary period (Bauch et al., 1997).

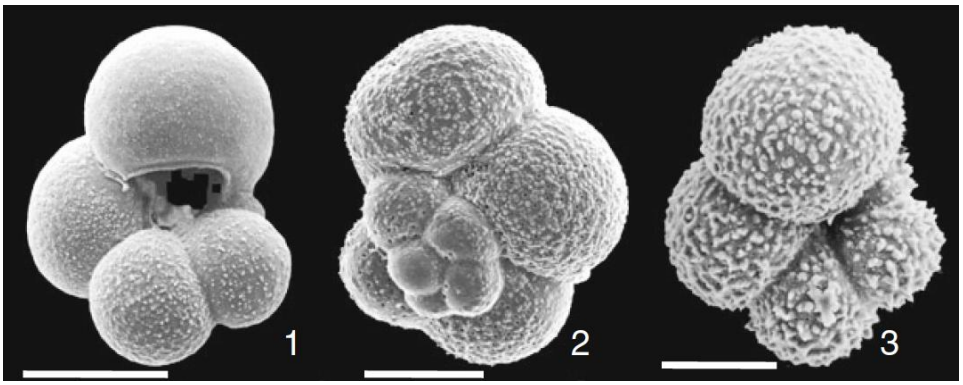

Figure 4.4: SEM images of *N. pachyderma*. (1) umbilical view, (2) spiral view, (3 umbilical view, showing the increasing crust formation. Scale bars: 100 µm (Schiebel and Hemleben, 2017)

It is not entirely certain at which depth *N. pachyderma* calcifies, but most studies suggest between 50- and 100-meters water depth (Kohfeld et al., 1996; Reynolds & Thunell, 1986). However, deeper calcification depths (100-200 m) have been observed (Bauch et al., 1997; Niebler et al., 1999), especially for upwelling regions (Darling et al., 2017; Greco et al., 2019; Ivanova et al., 1999), suggesting a variable depth habitat. *N. pachyderma* has also been

associated with high chlorophyll content (Kohfeld et al., 1996). In the southern hemisphere, the peak blooming of *N. pachyderma* occurs over a few weeks of austral summer and this accounts for nearly 95% of the annual flux (Jonkers et al., 2010). *N. pachyderma* is easily recognisable by its four-chamber structure in the final whorl (fig. 4.4), and it has a distinct sinistral (left) coiling (Darling et al., 2006).

Subpolar species

Neogloboquadrina incompta (Cifelli 1861)

Neogloboquadrina incompta (hereafter *N. incompta*) appears remarkably like *N. pachyderma*, and the only thing physically separating them is their coiling direction. *N. pachyderma* and *N. incompta* were previously thought to be the same species, but recent genetic studies showed that they were two different species (Darling et al., 2006; Darling et al., 2004; Darling et al., 2000). *N. incompta* prefer temperatures from subpolar to temperate climate (8-21˚C) (Fig. 4.5) (Tolderlund et al., 1971). *N. incompta* is the most abundant planktic foraminifera along the Chilean margin (Marchant et al., 2004; Marchant et al., 1998). In the North Atlantic, it mostly calcifies above the pycnocline (> 50 m), preferring warm and shallow waters (Morley et al., 2017). A link to chlorophyll has also been observed, as highest *N. incompta* abundances coincide with the chlorophyll maximum zone (Bergami et al., 2009). Maximum flux of *N. incompta* occurs during blooming season from July - January (at 30˚S) (Hebbeln et al., 2000; Marchant et al., 1998).

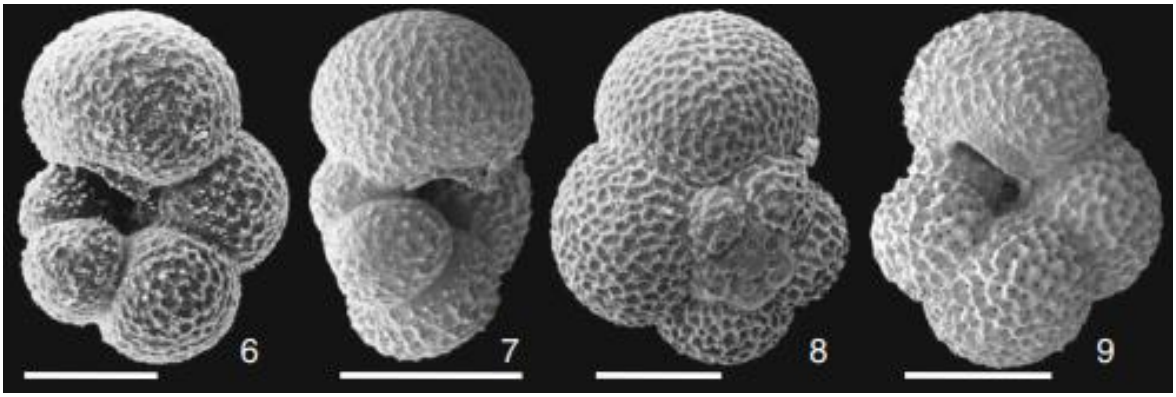

Figure 4.5: SEM image of *N. incompta*, (6 and 9) umbilical view, (7) lateral view, (8) spiral view. Scale bars: 100 µm

Coiling direction in Neogloboquadrina

N. pachyderma is used as a paleoclimate indicator with its coiling counterpart *N. incompta* (Bandy, 1960; Boltovskoy, 1973; Ericson, 1959; Ericson et al., 1955). The coiling ratio is often used as a proxy for sea surface temperature change (sinistral coiling dominates polar ocean while dextral dominates subpolar to transitional (Kucera, 2007)). The left and right coiling forms of *N. pachyderma* were regarded as ecophenotypes for a long period but are now known from observations (Brummer & Kroon, 1998) and molecular genetic studies to be two distinct species. *N. pachyderma* is the left coiling / sinistral form whilst the right coiling/dextral, warmer water form is now named *N. incompta*, following the recommendation of Darling et al. (2006). However, the coiling direction is still used as a climate indicator, and the easiest way to visually distinguish *N. incompta* from *N. pachyderma*.

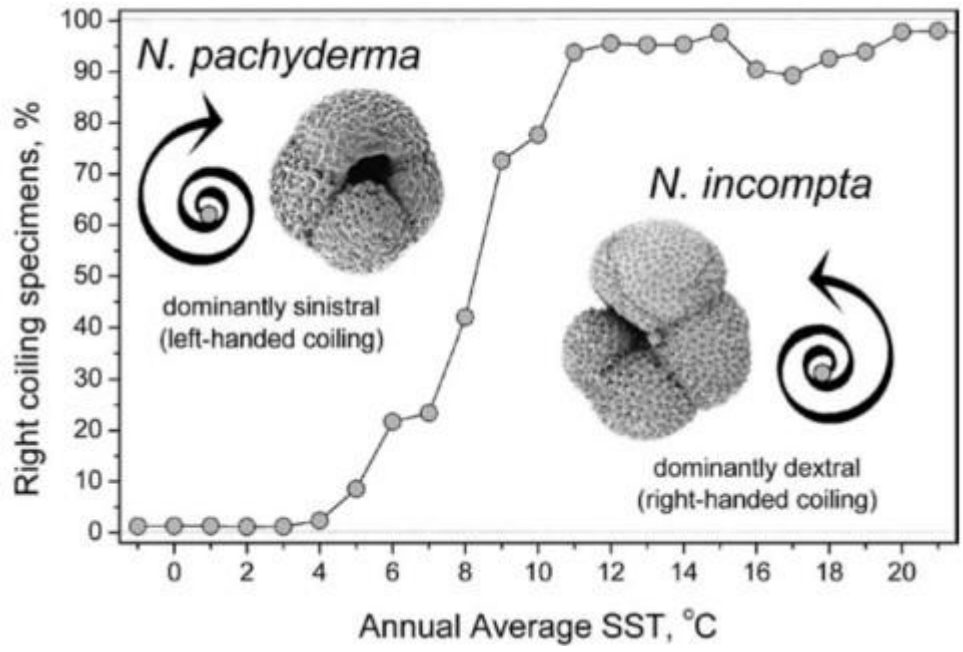

Figure 4.6: Average abundance of *N. pachyderma* versus *N. incompta* with respect to sea surface temperatures. *N. pachyderma* dominates the low SST found in the polar regions, while *N. incompta* abundance increases rapidly from 6° - 8°C and dominates above 8°C. Figure from (Kucera, 2007).

The coiling ratio of *N. pachyderma* is calculated as the percentage of sinistral coiling variety (*N. pachyderma*) in total *N. pachyderma* (sinistral + dextral coiling, i.e., *N. incompta*), and used as a proxy for SST variability.

Turborotalita quinqueloba (Natland, 1938)

Turborotalita quinqueloba (hereafter *T. quinqueloba*) is a planktic foraminifera species which thrives in the subpolar zone (fig. 4.3). *T. quinqueloba* has been found between 1˚ and 21˚C, but it prefers temperatures colder than 12˚C (Be and Tolderlund, 1971). In the near surface waters around Antarctica, it is most abundant in temperatures between 1 to 5˚C (Tolderlund et al., 1971). *T. quinqueloba* is a good indicator for frontal movements (Johannessen et al., 1994; Wright & Flower, 2002), and its relative abundance can be used to infer the proximity of SAF/PF relative to core sites (De Deckker et al., 2012). *T. quinqueloba* is presumed to be a near surface dweller (B´e & Hutson, 1977; Carstens et al., 1997), and it does not undergo much secondary calcification at depth, which means it is ideal to reflect conditions near the surface (Simstich et al., 2003). *T. quinqueloba*, together with *N. pachyderma*, may function as a proxy for dominant haline conditions and regions with absent thermal stratification in the ocean (Simstich et al., 2003). *T. quinqueloba* is distinguished by five chambers and with a large cap on the largest chamber (fig. 4.7)

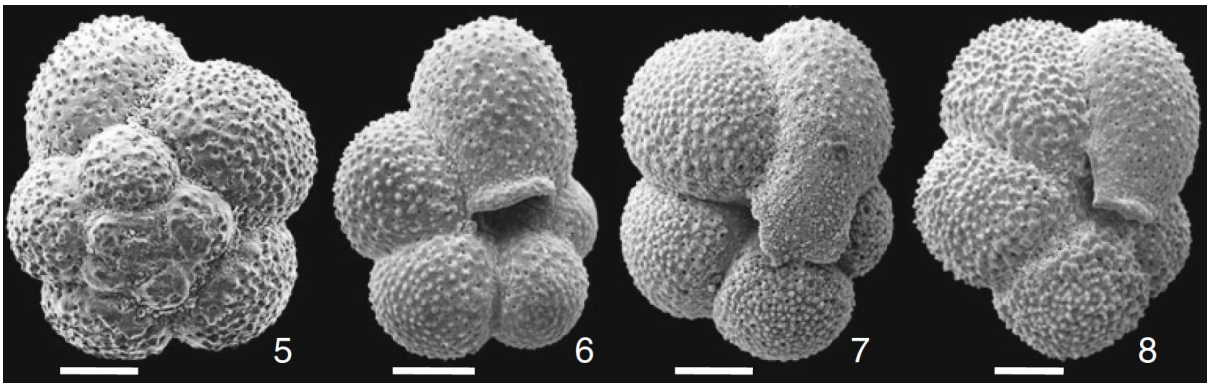

Figure 4.7: SEM images of *T. quinqueloba.* (5) spiral views , (6, 7 and 8) umbilical views, showing different apertural features seen in *T. quinqueloba*. Scale bars: 50 µm (Schiebel and Hemleben, 2017)

Transitional species

Globigerina bulloides (d'Orbigny, 1826)

Globigerina bulloides (hereafter *G. bulloides*) is one of the most dominant planktonic foraminifer species in subpolar to subtropical waters (Tolderlund et al., 1971). *G. bulloides* also prefers waters with low salinity and its peak abundance is found between 3˚C and 19˚C (Tolderlund et al., 1971). *G. bulloides* generally thrives in temperate, subpolar, upwelling and environments with high productivity (Sautter & Thunell, 1991; Spero & Lea, 1996; Thiede, 1975), and generally found in the upper 100 m (Fairbanks et al., 1982). Niebler et al. (1999) suggests mean calcifications depths between 0-50 m, making *G. bulloides* one of the most used planktonic foraminifera in reconstructions of surface ocean properties (Field, 2004). Blooming of *G. bulloides* occurs during austral summer (January) during times of highest SSTs (Marchant et al., 1998).

G. bulloides is easily recognizable with its four distinct chambers in the last whorl and a wide opening/aperture on its umbilical side. The last chamber is the largest chamber (figure 4.8) and the chambers become smaller in a circular inward fashion.

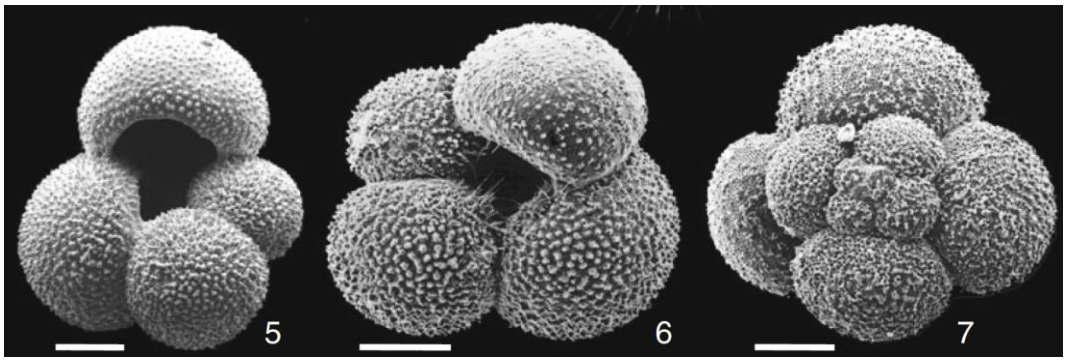

Figure 4.8: SEM images of *G. bulloides*. (5 and 6) umbilical views, (7) spiral view. Scale bars: 100 µm (Schiebel and Hemleben, 2017)

Globigerinita glutinata (Egger, 1893)

Globigerinata glutinata (hereafter *G. glutinata*) is a planktic foraminifera which thrives in nutrient-rich upwelling zones in the subpolar zone (Cayre et al., 1999; Naidu & Malmgren, 1996; Ottens & Nederbragt, 1992; Tolderlund et al., 1971). The preferred temperature range

of *G. glutinata* is betweeen 14˚C and 30˚C, but it has been found to tolerate temperatures as low as 3˚C (Cayre et al., 1999) The species is over 30 million years old and hence one of the longest living species of planktic foraminifera known (Pearson et al., 2018). It is distinguished from other sorts of the Globigeriniforms by the glutinata-type microperforate smooth wall texture (Parker, 1962; Pearson et al., 2018). *G. glutinata* usually consist of three larger globular shaped chambers and one half-chamber (Pearson et al., 2018), with an opening/aperture that covers part of the half chamber (fig. 4.9). Sometimes, this opening can be covered by a cover called "bulla" (Pearson et al., 2018). The last formed chamber or bulla is usually thinner than the other chambers (Parker, 1962). The bulla can vary in size, from almost covering noting to looking like a whole chamber (Parker, 1962; Pearson et al., 2018). *G. glutinata* share similarities with other species of the Globigerinitidae family and can sometimes be difficult to distinguish from other species of the same genus. Parker (1962) hypothesis that *G. glutinata* is still evolving from the Globigerinitidae family.

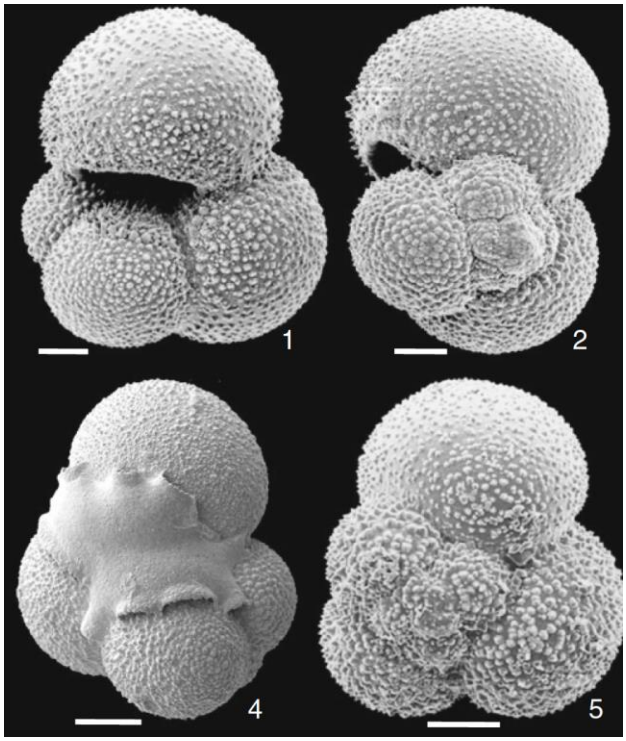

Figure 4.9: SEM images of *G. glutinata* (1) umbilical view, without bulla, (2) lateral view, without bulla (4) umbilical view, with bulla, (5) spiral view. Scale bars: 50 µm (Schiebel and Hemleben, 2017)

Globorotalia inflata (d'Orbigny, 1839)

Globorotalia inflata (hereafter *G. inflata*) is frequently found in the transitional zone, between subpolar and subtropical waters, and its abundance rapidly decreases outside this zone (Tolderlund et al., 1971). SSTs in the transitional zone (i.e., between 35°S and 45°S in SH) varies from 13°C to 19°C, where *G. inflata* is found in high abundances (Tolderlund et al., 1971). *G. inflata* is found in high quantities at subtropical upwelling environments, but it is not considered to be a typical upwelling indicator species (Deuser et al., 1981; Fairbanks et al., 1980; Ravelo et al., 1990; Van Leeuwen, 1989). *G. inflata* is a deeper dwelling planktonic foraminifer, it inhabits the upper 200 m of the ocean column (Be, 1960; Fairbanks et al., 1980), and isotope data indicates equilibrium with near surface water (Deuser et al., 1981). *G. inflata* may be a victim of secondary calcification in the deeper parts of the ocean during sinking, which can alter the isotope composition (Deuser et al., 1981). *G. inflata* is recognized by three to four chambers in its last whorl, a rather flat spiral side, and convex umbilical side (Schiebel and Hemleben, 2017). Schiebel and Hemleben, 2017 also remarks that fossil tests of G. inflata often has a shiny appearance caused by crystalline calcite veneer.

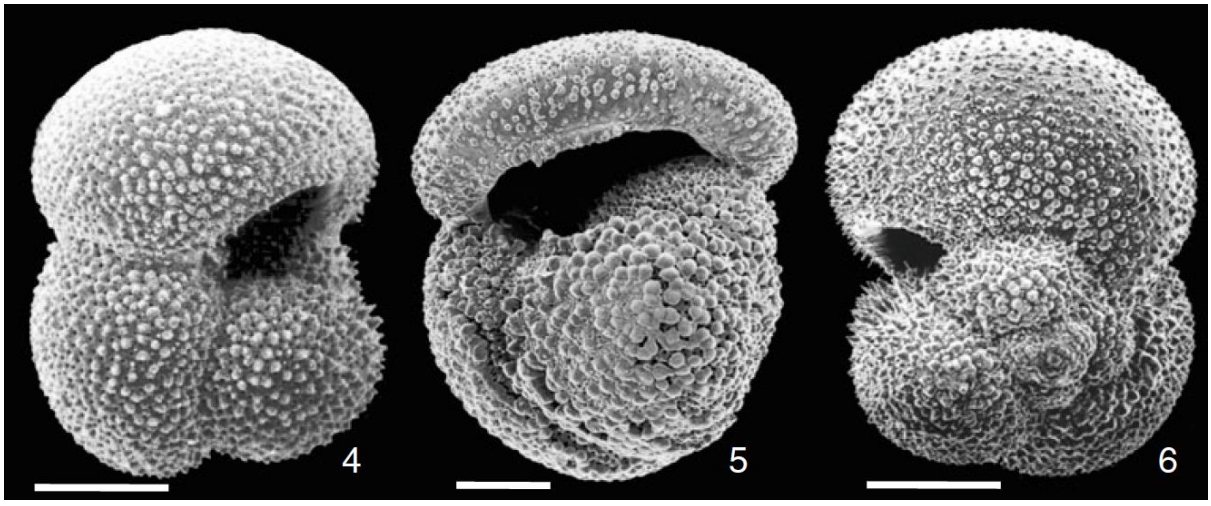

Figure 4.10: SEM images of *G. inflata.* (4) umbilical view, (5) lateral view, showing aperture in details, (6) spiral view. Scale bars: 100 µm (Schiebel and Hemleben, 2017)

4.4.2 Benthic foraminifera

Cibicidoides wuellerstorfi (Schwager, 1866)

Cibicidoides wuellerstorfi (hereafter *C. wuellerstorfi*) is an epifaunal benthic foraminifera, that lives above the sediments at the ocean floor. *C. wuellerstorfi* incorporates the bottom water chemistry in its carbonate shell, mostly unaffected by the pore water chemistry in the sediments (Wefer & Berger, 1991), but spreading to shallow infaunal habitat has been observed (Fontanier et al., 2006; Wollenburg & Mackensen, 1998). This property to incorporate the bottom water properties makes *C. wuellerstorfi* an excellent record for stable isotope proxies. δ^{13}C values in

C. wuellerstorfi has been observed to be close to equilibrium (Graham et al., 1981; Grossman, 1987; Wefer & Berger, 1991). δ^{18}O in *C. wuellerstorfi* does not display equilibrium with ambient seawater, but has a constant offset which still makes it suitable for use as a reliable proxy (Graham et al., 1981).

Figure 4.11: *C. wuellerstorfi* from spiral view (6), apertural view (7) and umbilical view (8). From Holbourn and Henderson, 2002)

4.5 Lithic counts

Ice Rafted Debris (IRD) are small mineral grains (>150 µm) found at the ocean floor. These fragments originate from glacial deposits which calves at the ocean (in fjords and along the coast). The amount of IRD found in marine sediment samples is used as an indicator of the

presence and variability of glaciers and ice sheets. When glaciers calve into the ocean, they generate floating icebergs that are transported by prevailing surface winds and surface ocean currents. When these icebergs reach warmer waters, they melt and the lithic material in the iceberg sink to the bottom of the seafloor (Fig. 4.12). The minerogenic composition in the IRD deposits depends on the source rock on land, and it must also be considered that different minerals usually occur in different fractions due to differential weathering of soft or hard rocks. Previous studies show distinct IRD maxima during peak glacial conditions, during deglaciation and during the Heinrich events (Heinrich, 1988) in the Northern Hemisphere (Bond et al., 1992; W. S. Broecker, 1994; Kleiven et al., 2002; W. F. Ruddiman, 1977). Southern Hemisphere IRD records should represent the same, however it has not been studied in the same extent as NH.

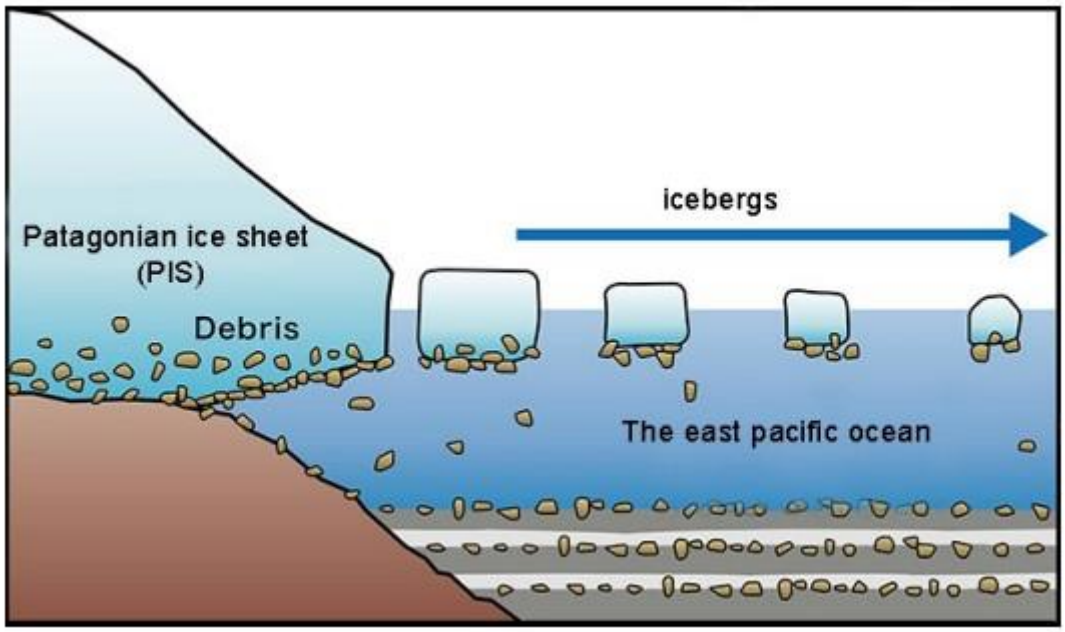

Figure 4.12: Simplified overview of the IRD deposition (JAMSTEC, 2015).

The presence of IRD is frequently used as an indicator for ice sheet variability, both waxing and waning, and hence it can be used as an indicator for changing climatic conditions. During the last glacial period, the Northern Hemisphere experienced rapid climate variability, i.e., the Danschgaard-Oeschger cycles, and often related to these were the occurrence of large IRD deposits, known as Heinrich Events, after Heinrich (1988). The sediment during Heinrich Events showed a large difference in chemistry then sediment deposited before and after the Heinrich Events (W. S. Broecker, 1994). Another composition changes of the sediments found

from Heinrich Events are the decreasing abundance of foraminifera (Bond et al., 1992; W. S. Broecker, 1994) where there are usual thousands per gram in normal ocean sediment, they drop to hundreds or less per gram during Heinrich Events. To obtain a potential record of ice rafted debris (IRD) transported to the core site during the study interval, only lithic fragments or lithics, pieces of rock that have been eroded down to sand grains, were counted. In this study, the relative abundance of IRD is calculated as a percentage (IRD %), i.e., the number of IRD grains in total entities (planktonic and benthic foraminifera).

5. Chronology

Accurate dating is of critical importance in paleoclimatic studies. Without reliable age-constraints it is impossible to constrain if climatic events happened synchronously or if certain events led or lagged others. The data obtained from counting foraminifera species and the stable isotope values provide valuable information about the changing oceanography and climate at ODP site 1233 downcore, but these data plotted versus core depth does not inform anything about at which timescales the climate variability occurs. To plot the data on an age scale, an age model must be constructed. In the following chapter, the establishment of the ODP 1233 age models is presented. For this study, spanning Antarctic warming A2, the age model by Førde (2008) and Kleiven et al., (2007) is used.

5.1 Previous age models used at ODP site 1233

Radiocarbon dating is frequently used in geological dating of marine deep-water cores, due to the large presence of carbonaceous sediments. The naturally occurring unstable carbon isotope 14 (^{14}C) has a half-life of 5780+-40 years (Libby et al., 1961), and using conventional methods (Accelerator Mass Spectrometry), radiocarbon dating is reliable to about 40 Kyr BP (Ruddiman, 2001).

The first age model for ODP site 1233 was published by Lamy et al., (2004), for the interval between 10.55 and 64.81 mcd, which represented 8 – 40 Kyr BP, spanning the deglaciation and the last glacial period. Lamy et al., (2004) constructed the age model using 17 AMS ^{14}C dates as well as the midpoint of the Laschamp geomagnetic excursion (41 Kyr BP) that is well registered in the in ODP 1233 sediments (Lund et al., 2007). Due to increasing uncertainties in the oldest AMS ^{14}C dates, the age model beyond the Laschamp excursion, was extrapolated to 50 Kyr BP by assuming constant sedimentation downcore after 41 kyr. This first study from ODP 1233 exhibited a clear Antarctic timing of the independently dated paleoclimate signals (Alkenone SSTs) when compared to the Byrd ice core (Blunier and Brook, 2001; Lamy et al., 2004). In 2005, Kaiser et al., (2005) proposed a revised age model for Site 1233, specifically for the interval older (<41 Kyr BP) than the Laschamp excursion. Kaiser and co-workers

(2005) used the alkenone SST signal from ODP site 1233 and tuned it to the layer-counted Byrd ice core age scale. The AMS ^{14}C dated Alkenone SST signal and the Antarctic temperature variability in the Byrd ice core correlate well for the interval younger than 40 Kyr BP (Kaiser et al., 2005), and the same relationship continues downcore, allowing the age scale tuning, i.e. determining chrono-stratigraphic tie points by assigning temperature minima and maxima values of the alkenone SST from ODP site 1233 to glacial stadials and interstadials in the Byrd ice core respectively.

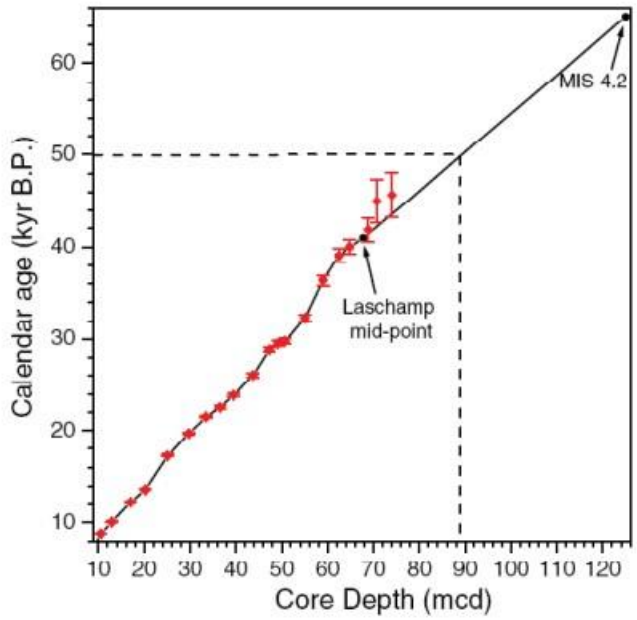

Figure 5.1: The age control points used by Lamy et al. (2004) at ODP site 1233 for the age model. The 17 AMS^{14}C (red crosses) and Laschamp Magnetic excursion. Note the three AMS^{14}C dates beyond Laschamp Magnetic excursion which was ignored. (Lamy et al., 2004)

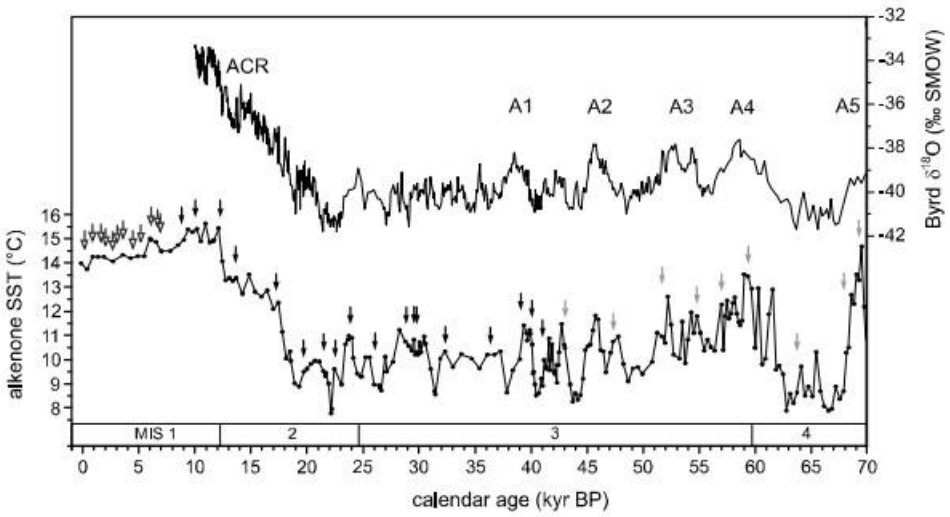

Figure 5.2: Age model generated by Kaiser et al. (2005). AMS ^{14}C dates are used until the Laschamp excursion (41Kyr BP) and for the older part of the record the age model is constructed by tuning the alkenone SST record to the Byrd ice core δ^{18}O record. Open arrows represent Holocene correlation with core GeoB33131. Black arrows are AMS ^{14}C dates and grey arrows represent alkenone SSTs tuned to Byrd ice core.

5.2 A new tuned age model spanning A1 and A2

Førde (2008) pointed out that the alkenone SST signal at ODP site 1233 may be strongly affected by the local climate and surface ocean conditions in the Chilean fjord region. As mentioned in the background chapter, the region has heavy yearly rainfall, and thus rivers and fjords have a strong freshwater discharge. To overcome this, Førde (2008) constructed a new high-resolution δ^{18}O record using the benthic foraminifera, *Uvegerina peregrina (*hereafter *U. Peregrina)*, which is an infaunal species (i.e., lives within the sediments) (Fontanier et al., 2006), thus unaffected by SST changes. Unlike the alkenone SST data by Lamy et al., (2004) and Kaiser et al., (2005) that was analysed every 15-20 cm, Førde's benthic stable isotope record was measured every 4 cm, providing significantly higher resolution. To look for a better tuning target than the low-resolution Byrd ice core, Førde used the European project for ice coring in Antarctica (EPICA) core drilled in 2006 in Dronning Maud Land, hereafter denoted EDML. (EPICA community members, 2006). EDML is 2500 m long and goes back 150 Kyr and provides one of the highest-resolution ice core records, obtained outside Greenland that extends well beyond the last glacial maximum (Steig, 2006). EDML has

furthermore been tuned to the Greenland ice core record by pattern of millennial-scale atmospheric methane fluctuations (EPICA community members, 2006; Blunier et al., 2007), allowing a comparison between the two hemispheres.

Below is a short description on the process used by Førde (2008) to tune the *U. peregrina* $\delta^{18}O$ signal with the EDML isotope signal to construct an age model for A1, a method which was continued over A2 in Kleiven et al., (2007, 2014).

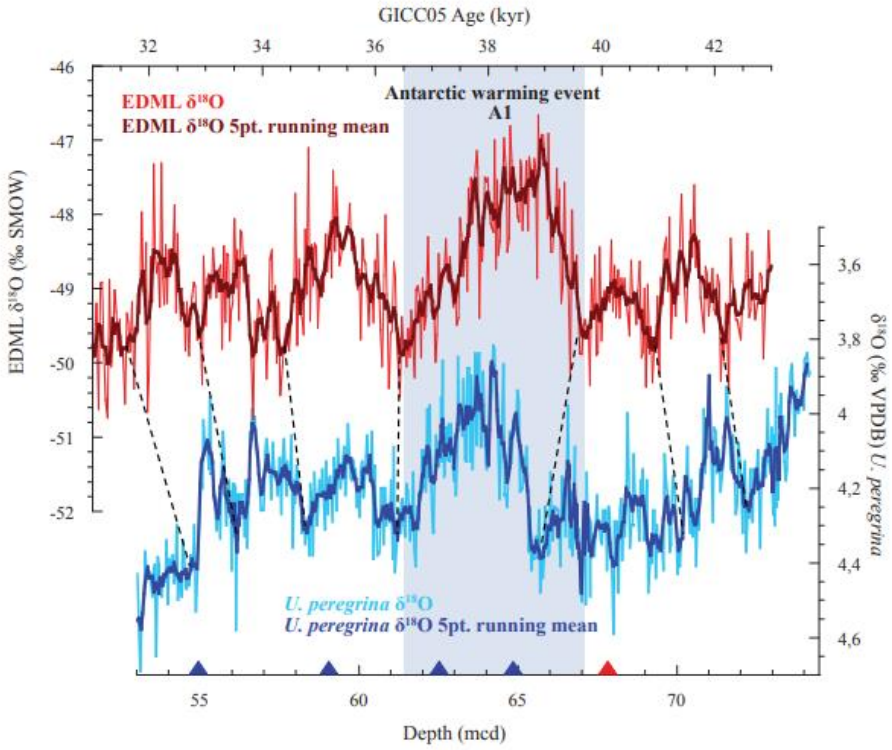

Figure 5.3: The lower panel shows the $\delta^{18}O$ record of the benthic foraminifera *U. peregrina* from ODP Site 1233 plotted versus depth. The Antarctic warming event A1 (Blunier and Brooke., 2001) is shaded blue. The upper panel exhibits the EDML $\delta^{18}O$ record plotted versus age. The EDML age model (EPICA community members, 2006; EPICA community members, 2010) is plotted on the new Greenland Ice Core Chronology 2005 (GICC05) that is based on annual layer counting (Andersen et al., 2006). The light red curve represents the unsmoothed $\delta^{18}O$ from EDML, and the light blue curve shows the $\delta^{18}O$ from ODP Site 1233. The dark red and dark blue curve is the 5-point running mean for both records respectively. The stipled lines represents $\delta^{18}O$ maxima used for tuning. The blue triangles show the AMS ^{14}C ages after Lamy et al. (2004) and the red triangle represent the Laschamp Excursion (Lund et al., 2007). Figure is from Førde (2008). For tuning of the new age model presented by Førde (2008) $\delta^{18}O$ maxima (cold) (fig. 3.3) were used as corelation points. From figure 3.3 six warm periods and seven cold are visible. Førde (2008) used four AMS^{14}C dates for interpolation between ODP site 1233 and EDML. Figure 3.4 shows the tuned age model between ODP site 1233 and EDML.

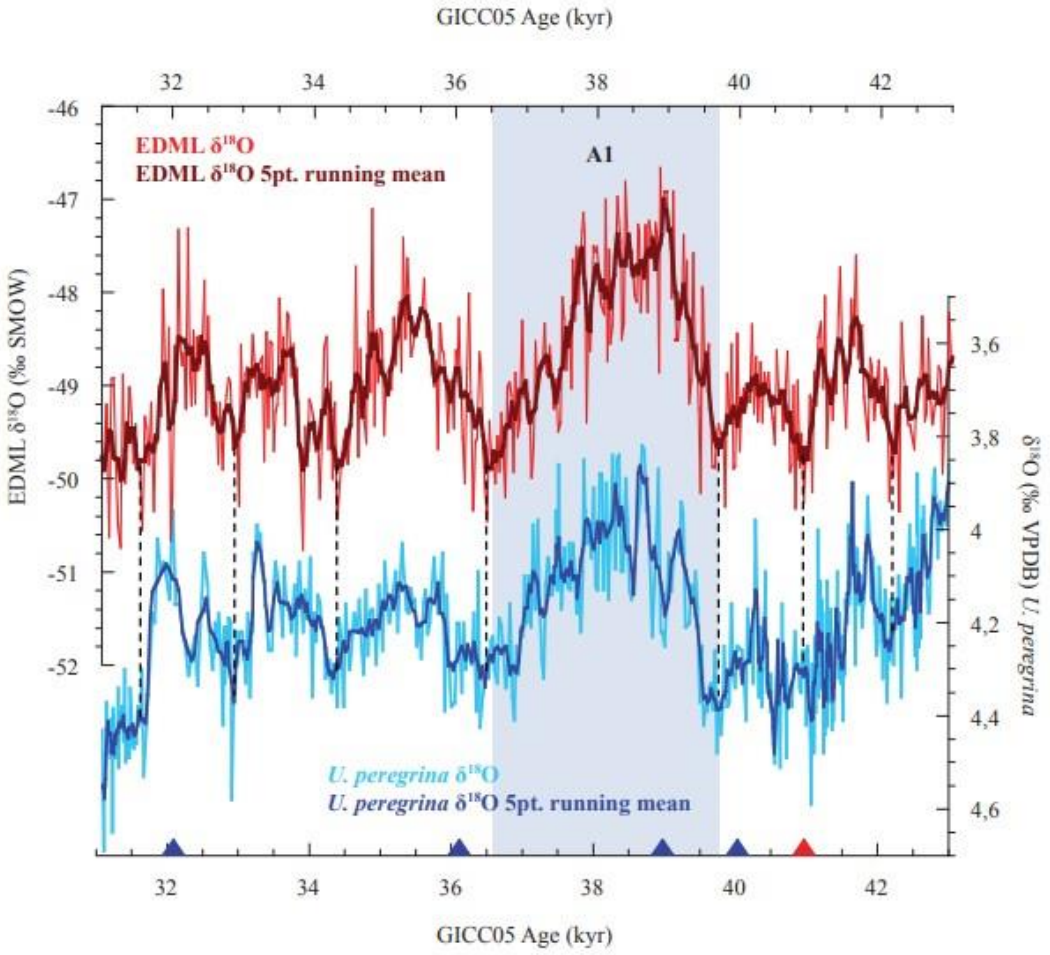

Figure 5.4: The $\delta^{18}O$ record of the benthic foraminifera *U. peregrina* from ODP Site 1233 plotted versus age compared to the EDML $\delta^{18}O$ record (EPICA community members, 2006; EPICA community members,2010) plotted versus age. The light red curve represents the unsmoothed $\delta^{18}O$ values from EDML, and the light blue curve shows the unsmoothed $\delta^{18}O$ values from ODP Site 1233. The dark red and dark blue curve is the 5-point running mean for the $\delta^{18}O$ records. The dotted lines represent $\delta^{18}O$ maxima, which can be matched between the two records. The blue triangles show the AMS^{14} ages from Lamy et al., (2004) and the red triangle represent the Laschamp Excursion (Lund et al., 2007). Figure 5.9 from Førde (2008)

To construct a new age model, Førde (2008) used $\delta^{18}O$ maxima (cold events) clearly identified in both records as corelation points. Both records display six warm intervals (including A1) and seven cold intervals. When tuning, the Laschamp event remained a fixed stratigraphic marker in ODP 1233 at 41 Kyr BP. In addition, the four AMS ^{14}C dates had age uncertainties that increased with increasing core depth; ± 0.39 Kyr, 0.58 Kyr, 0.75 Kyr and 0.79 Kyr respectively (Kaiser et al., 2005) and hence could only be adjusted within their error. Figure 3.2 shows the EDML $\delta^{18}O$ record plotted versus age and the ODP 1233 $\delta^{18}O$ record plotted versus the tuned age model.

The interpolation done by Førde (2008) assumed constant sedimentation rates between the age control points. For the A2 event of ODP 1233, the study interval for this thesis, Kleiven et al., (2007, 2014) continued the tuning between the EDML ice core $\delta^{18}O$ and the benthic $\delta^{18}O$ signal from ODP 1233 down to 50 Kyr B.P. (Figure 3.3) Both Førde (2008) and Kleiven et al., (2007, 2014) concludes that the *U. peregrina* $\delta^{18}O$ record matches the EDML $\delta^{18}O$ record on millennial to centennial scale, revealing a clear Antarctic timing of temperature changes during the study interval.

Figure 3.5 shows the age model generated by Førde (2008) extended in to A2. For the age correlation to this study interval two tie points from Kleiven et al (2007, 2014) and Førde (2008) at the isotopic minima at ~43.2 and ~48.5 (fig. 3.5 dashed lines) is used and then constant sedimentation rates are assumed for the whole interval. Sedimentation rate average 220 cm/Kyr (Euler, 2010) at ODP site 1233 during MIS 3 and 160 cm/kyr of A2 (Euler, 2010). The A2 warm interval was sampled every 8 cm on average which corresponds to a resolution of ~52 yrs with a sample spacing of 8 cm.

The few tie points during A2 makes the uncertainty of the age model greater.

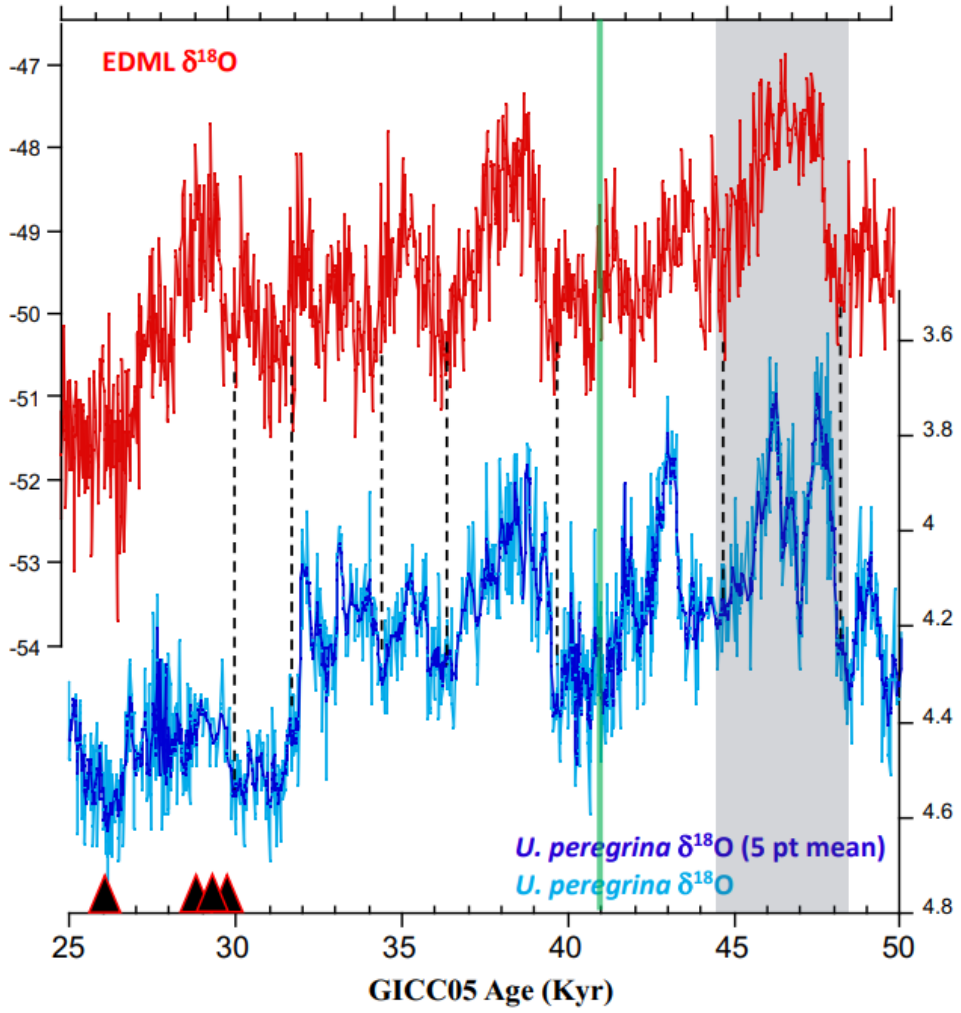

Figure 5.5: The benthic $\delta^{18}O$ record of *U. peregrina* from ODP site 1233 plotted versus age compared to the EDML Ice Core $\delta^{18}O$ record (EPICA community members, 2006; EPICA community members,2010) spanning 25-50 kyr (Kleiven et al., 2007, 2014) The black triangles represent AMS^{14} dates after (Kaiser et al., 2005), the green line represent the Laschamp Magnetic excursion at 41 kyr(Lund et al., 2007) and the black dashed lines represents the tuning points to the oxygen isotopes of the EDML ice core age scale (Kleiven et al., 2007, 2014; Førde 2008). Grey shading represents the study interval in this thesis, spanning from ~44 to ~49 Kyr BP.

6. Results

In this chapter the results from the high-resolution stable isotope analysis, the planktonic foraminiferal assemblages and the IRD counts are presented. The data produced in this thesis, with sedimentary samples from ODP Site 1233, spans from 76.19 to 83.65 mcd and represents an age interval from ~43.9 Kyr BP to ~48.8 Kyr BP. The study interval spans Antarctic Warming Interval 2 (A2). The planktonic foraminiferal counts (assemblages) from the most abundant species from ODP Site 1233 are presented. These include *N. pachyderma, N. incompta, G. bulloides, T. quinqueloba, G. inflata* and *G. glutinata*. The *N. pachyderma* sinistral coiling ratio is calculated as the percentage of sinistral coiling variety of *N. pachyderma* in total *N. pachyderma* (sinistral + dextral, i.e., *N. incompta*), and presented as a proxy for SST. Ice Rafted Detritus (IRD) counts are also presented. In addition, high resolution stable isotope analysis (δ^{18}O and δ^{13}C) has been measured on the epibenthic species *C. wuellerstorfi*. The stable isotope analysis, planktonic foraminiferal assemblages and IRD counts are all performed on the same samples, with 8 cm resolution throughout the study interval. Based on the age model used in this thesis (Chapter 4), this corresponds to a sample spacing/resolution of 52 years on average.

ODP site 1233 has previously been studied by several researchers and master students at UoB (Table 4.1). In this chapter however, I will only present data produced in this master thesis study. Later, in the discussion chapter, these new data will be compared with previous studies from ODP site 1233 (Table 6.1). All assemblage counts, IRD counts, and stable isotope measurements are listed in the Appendix.

ODP Site 1233 Data	References	Resolution
Uvegerina peregrina $\delta^{18}O$ and $\delta^{13}C$	Førde(2008) Kleiven AGU (2007, 2014)	4cm/26yrs
Globigerina bulloides $\delta^{18}O$ and $\delta^{13}C$	Euler(2010)	4cm/26yrs
Neogloboquadrina incompta $\delta^{18}O$ and $\delta^{13}C$	Euler(2010)	4cm/26yrs
Alkenone based SSTs	Lamy et al., 2004, Kaiser et al., 2005	320yrs
Cibicidoides wuellerstorfi $\delta^{18}O$ and $\delta^{13}C$	this study	8cm/52yrs
Planktonic foraminiferal assamblages counts	this study	8cm/52yrs
Ice rafted debris counts	this study	8cm/52yrs

Table 6.1: Data produced in this thesis and data produced in earlier research project and master thesis at ODP site 1233 spanning A2. The mean sample resolution is shown in the right column.

6.1 Stable Isotope Results

In this section the results for oxygen and carbon isotopes from the epifaunal benthic foraminifera *C. wuellerstorfi* from ODP site 1233 over A2 are presented—reconstructing the physical and chemical properties of the AAIW that intersects the seafloor at the core site. The data are first plotted versus depth (mcd), then versus age (Kyr BP). The focus will be on the smoothed (3-point mean) record, because it provides a more general and robust measure of the average intermediate water conditions., but the higher variability of the non-smoothed record will also be described in this section.

A decrease of 1‰ in $\delta^{18}O_{calcite}$ is equal to a 4.2°C increase in temperature (Ruddiman, 2001), or a decrease in salinity of 1.47 p.s.u. in the South Pacific (Craig and Gordon, 1965). The isotopes values in the text and all figures are given in permille relative to the VPDB standard.

6.1.1 Oxygen isotope results

Figure 6.1 displays the $\delta^{18}O$ signal of *C. wuellerstorfi* from ODP site 1233 plotted versus depth (mcd). The study interval spans from 76.19 mcd to 83.65 mcd, spanning the entire A2 warm event. The y-axis has been reversed for better indication of warmer/fresher (peaks) and colder/saltier (troughs) temperatures and salinity. The non-smoothed $\delta^{18}O$ record has range of 0.89‰ over the entire study interval, with a minimum value of 3.22 ‰, at 81.61 mcd, and a maximum value of 4.11 ‰, at 80.69 mcd. The smoothed $\delta^{18}O$ record exhibit a total range of 0.61‰, with minimum value of 3.32‰ at 81.37 mcd, and maximum of 3.93‰ at 83.06 mcd.

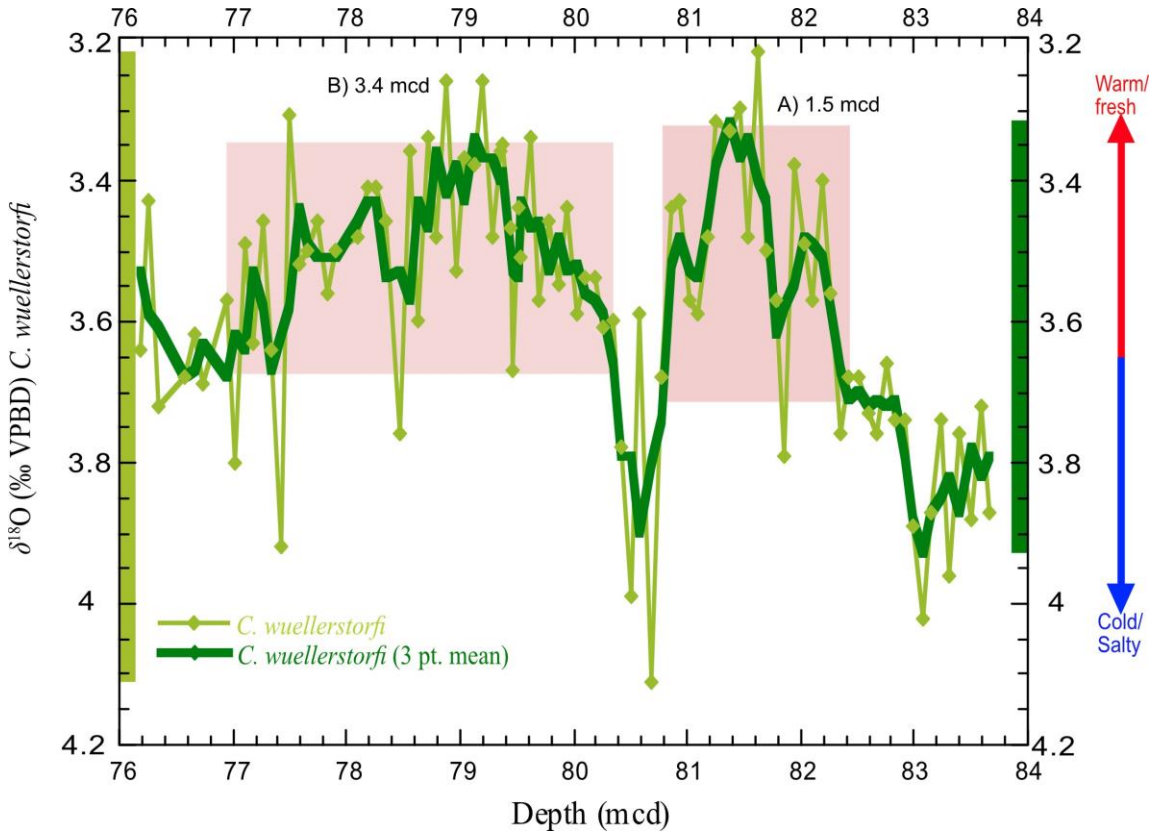

Figure 6.1: Oxygen isotope record of *C. wuellerstorfi* from ODP site 1233 plotted versus depth (mcd). The light green line is the non-smoothed record, and the dark green bold line is the smoothed (3-point mean) record. The total range of variability in the non-smoothed (left) and smoothed (right) signal on the y-axis are shown in their respective colour. Red shading displays the two prominent cycles of decreasing and increasing $\delta^{18}O$ values over the study interval.

The general trend of the benthic $\delta^{18}O$ record exhibit two distinct cycles (shaded red in Figure 6.1) of decreasing – increasing oxygen isotope values. Peak A spans ~1.5 mcd (~82.5 - ~81 mcd) with a range (decrease – increase) of ~0.4‰. Peak B spans 3.4 mcd (~80.4 - ~77.0 mcd) with a range (decrease – increase) of ~0.3‰. Superimposed on these two distinct peaks are $\delta^{18}O$ variations that exhibits amplitudes ranging between 0.1‰ and 0.5‰. Their significance and robustness are validated by the fact that several of these perturbations occur over several data points. The increase in $\delta^{18}O$ values from ~79 mcd to ~76.5 mcd displays more gradual increase, (occurring over a larger section of the core) when compared to the more abrupt (occurring over a shorter section of the core) increase from 81.2 to 80.5 mcd.

To account for the rate and timing of the observed oscillations spanning the study interval, the new proxy records are hereafter plotted on the age model described in chapter 5. Figure 6.2

displays the smoothed and non-smoothed *C. wuellerstorfi* δ^{18}O record from ODP site 1233 plotted versus calendar age thousands year B.P. (Kyr BP). According to the age model, the study interval from 76.19 mcd to 83.65 mcd spans the age interval from ~48.8 Kyr to ~44.0 Kyr BP, corresponding to the A2 warming event identified in the Antarctic ice cores.

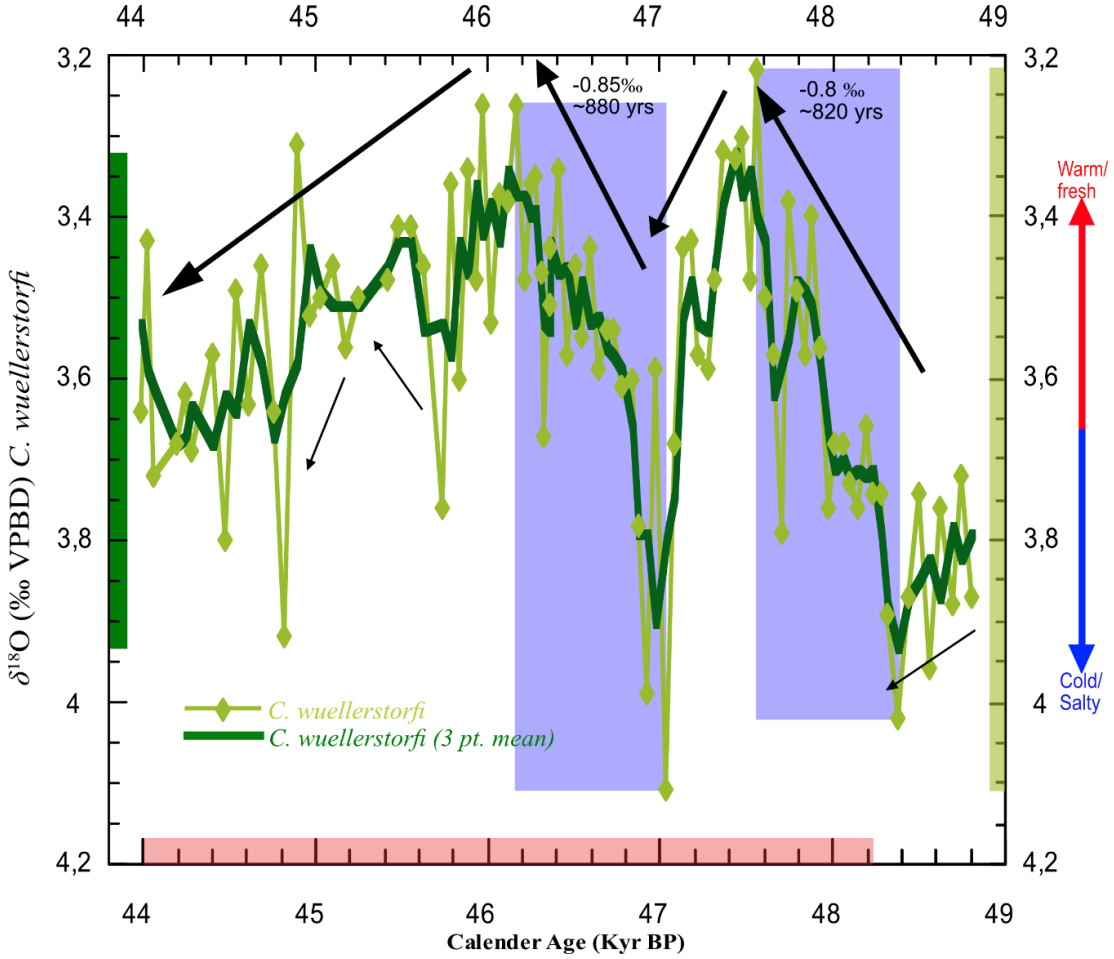

Figure 6.2: The oxygen isotope record of *C. wuellerstorfi* at ODP site 1233 plotted versus age (Kyr BP). The light green line is the non-smoothed record, and the darker green line is the smoothed (3-point mean) record. The total range of variability in the non-smoothed (left) and smoothed (right) signals are shown on the y-axis in their respective colours. Black large arrows indicate major trends in the dataset, whereas smaller black arrows indicate minor trends in the dataset. The light blue shaded bars display two periods with large and rapid decrease in δ^{18}O values. Red horizontal bar shows A2 interval (48.23 – 44.0 Kyr BP) (Euler 2010).

The double-peak pattern of decrease-increase in δ^{18}O over A2 occurs on millennial time scales and superimposed on this are distinct fluctuations occurring on centennial time scales. There are two large centennial variations occurring over A2, both with a rapid initiation taking place

over just a few centimetres of sediment core. The first large decrease in $\delta^{18}O$, at the start of A2 (marked by a shaded blue box in figure 6.2), is initiated at ~48.4 Kyr BP and lasts for ~820 years, reaching a minimum value of 3.22‰ at ~47.6 Kyr BP, a decrease of ~0.8‰ (indicating a temperature increase of 3.63°C).

From the minimum value at ~47.6 Kyr BP, there is an abrupt increase in the $\delta^{18}O$ record from ~47.4 Kyr BP to the maximum $\delta^{18}O$ values of 4.11‰ at ~47.0 Kyr BP. The next major decrease in $\delta^{18}O$ values (also marked by a blue box in fig 4.3) starts at ~47.0 Kyr BP and last ~880 years until ~46.1 Kyr BP, with a total decrease of 0.85‰ (indicating a temperature increase of 3.86°C). From ~46.2 Kyr BP there is a gradual slow increase in the $\delta^{18}O$ values, lasting until the termination of A2 at ~44 Kyr BP There are also several minor, yet significant, $\delta^{18}O$ variabilities throughout the interval (see thin black arrows in figure 6.2). One occurring at the start of the A2 interval (48.8-48.4 Kyr BP), just prior to the first large decrease in $\delta^{18}O$ values. The other is a decrease-increase cycle, from ~ 45.7 Kyr BP to ~ 44.8 Kyr BP, superimposed on the long-term increase in $\delta^{18}O$ values before termination of A2.

6.1.2 Carbon isotopes results

Figure 6.3 shows the *C. wuellerstorfi* $\delta^{13}C$ record from ODP site 1233 plotted versus depth (mcd). *C. wuellerstorfi* $\delta^{13}C$ displays close relations with the ambient water masses (Graham et al., 1981), which makes *C. wuellerstorfi* an ideal benthic foraminifer for reconstructing past changes in benthic $\delta^{13}C$.

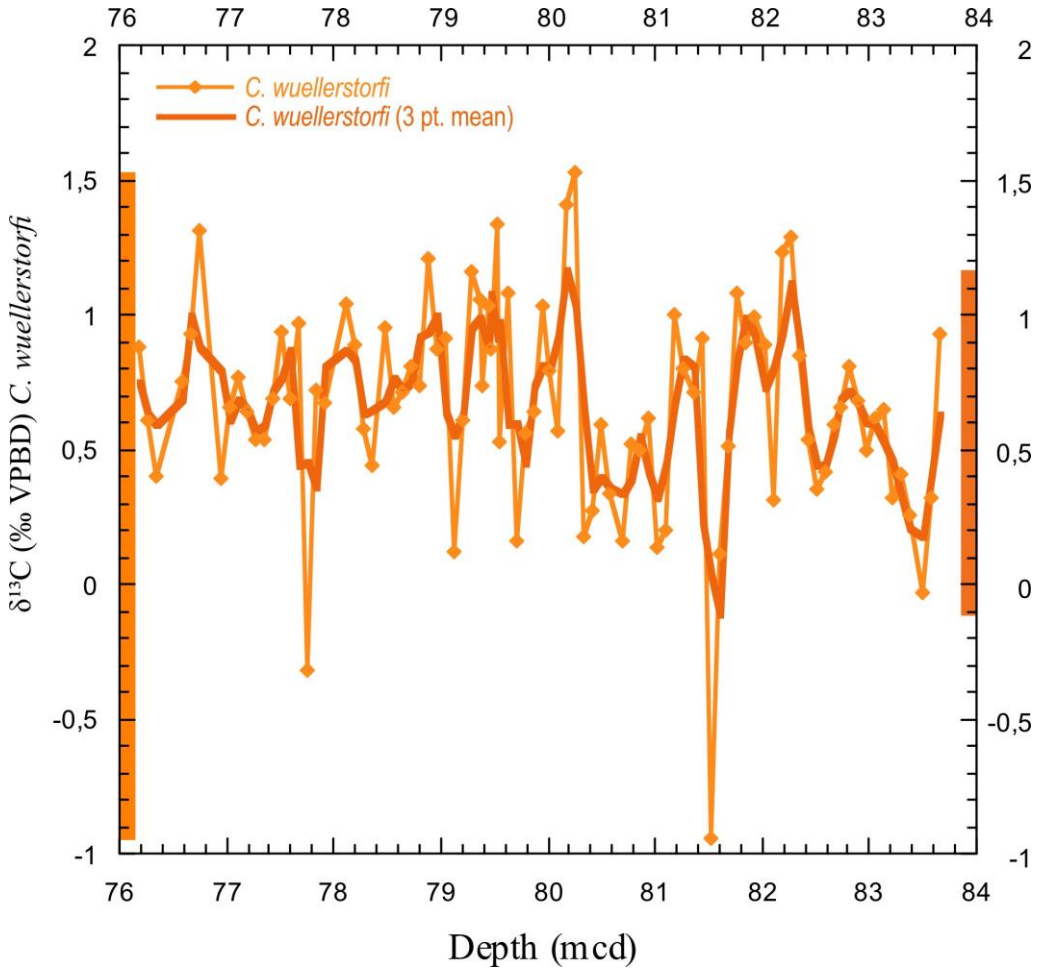

Figure 6.3: The carbon isotope record of *C. wuellerstorfi* at ODP site 1233 plotted versus depth (mcd). The light orange line is the non-smoothed record, and the darker orange line is the smoothed (3 pt. mean) record. Total range of variability in non-smoothed (left) and smoothed (right) on the y-axis are shown in their respective colour.

The $\delta^{13}C$ trend over the study interval displays a high frequency variability with an amplitude of ~ 0.5‰ in both the smoothed (3 pt. mean) and the non-smoothed $\delta^{13}C$ record. The nonsmoothed signal also exhibit two distinct decreases. The first distinct decrease occurs at 81.5 mcd and the other at 77.8 mcd. The non-smoothed record has a total range of 2.47‰, with the highest value of 1.53‰ at 80.26 mcd and lowest value of -0.94‰ at 81.53 mcd. The smoothed (3 pt. mean) record has a much lower range (1.28‰), with highest value of 1.17‰ at 80.18 mcd and lowest value of -0.11‰ at 81.61 mcd.

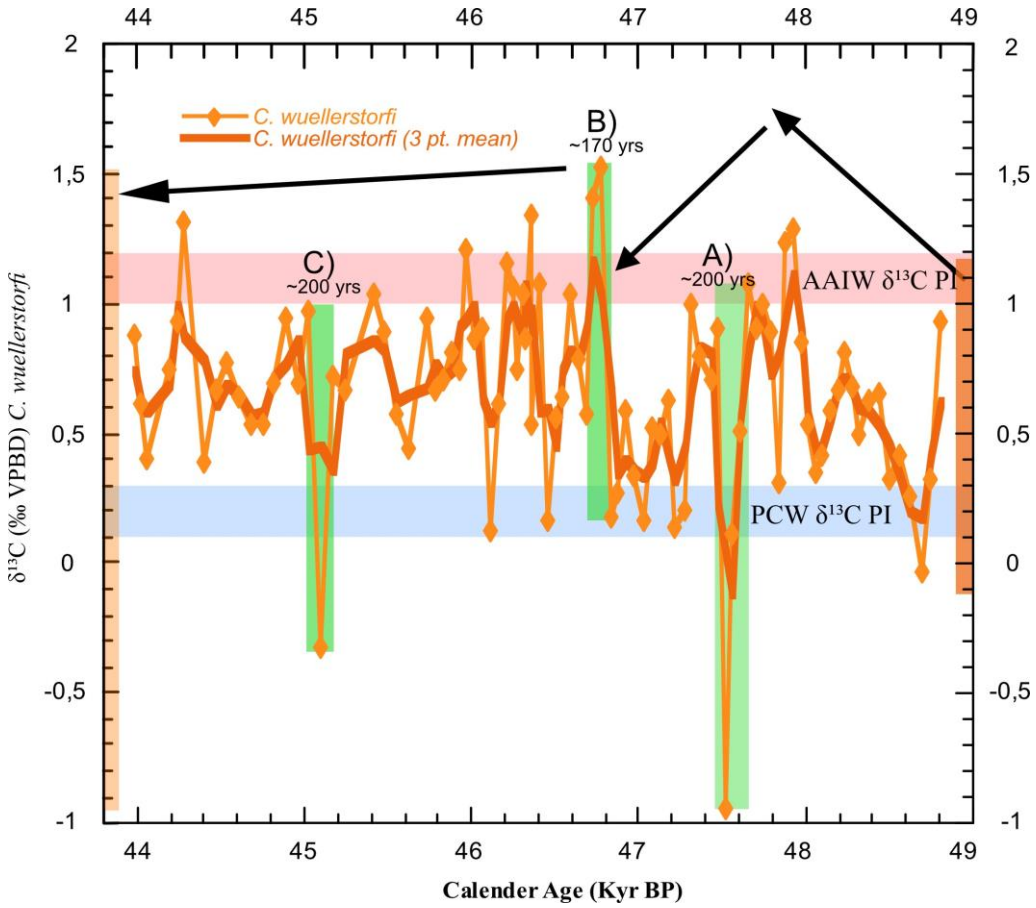

Figure 6.4: The carbon isotope record of *C. wuellerstorfi* at ODP site 1233 plotted versus age (Kyr BP). The light orange line is the non-smoothed record and darker orange line is the smoothed (3 pt. mean) record. Total range of variability in non-smoothed (left) and smoothed (right) on the y-axis are shown in their respective colours. The large black arrows display the long-term trend, and the light green vertical bars display periods of large and rapid change in the δ^{13}C record. The red horizontal bar shows preindustrial (PI) δ^{13}C values of the AAIW whereas the blue horizontal bar shows PI δ^{13}C values of the Pacific Central Water (PCW) (Eide et al., 2017).

Figure 6.4 displays the *C. wuellerstorfi* δ^{13}C record at ODP site 1233 plotted versus age (Kyr BP). The δ^{13}C record exhibit a distinct multi-centennial to centennial scale oscillation during the entire A2 warm event. These fluctuations are superimposed on a trend of increase of ~0.9‰ (from ~48.8 -47.9 Kyr BP) and a decrease of ~0.8‰ (from ~47.9 - 46.8 Kyr BP) (black arrows in figure 4.5). In addition, the δ^{13}C signal display a slightly decreasing trend (black arrow from ~46.8 Kyr BP to the termination of A2 with the higher frequency variability superimposed on it. The δ^{13}C signal exhibit a higher frequency spanning the first 1 Kyr from ~46.8 Kyr BP to ~45.8 Kyr BP, followed by a lower, more subdued frequency towards the termination of A2.

In figure 6.4 the three green vertical boxes highlight the three most rapid and distinct changes (A-C) in $\delta^{13}C$ values spanning the study interval. The first (A) rapid change happens at ~47.6 - ~47.4 Kyr BP and displays a decrease of 2.03‰ and then increase of 1.94‰ over a period of ~200 years. The second (B) rapid change occurs at ~46.8 - ~46.6 Kyr BP and displays an increase of 1.35‰ and then a decrease of 0.93‰ over ~170 years. The third (C), and last rapid change in the $\delta^{13}C$ record happens at ~45.2 - ~45.0 Kyr BP, displaying a decrease of 0.97‰ and then an increase 1.29‰ over ~70 years.

The thick red and blue bars in figure 4.5 displays the pre-industrial (PI) $\delta^{13}C$ of AAIW (red) and PCW (blue). As shown in figure 6.4, the $\delta^{13}C$ record mostly exhibit variability with values between the preindustrial AAIW and PCW estimates, although some exceptions occur. The rapid decrease-increase intervals (green boxes) all have $\delta^{13}C$ values either below PCW (A and C) or above AAIW (B).

6.2 Relative abundances of planktic foraminiferal species

This section presents the relative abundance of the most abundant planktic foraminiferal species found at ODP site 1233 spanning the A2 interval. Changes in the relative abundance is often tied to changes the ocean dynamics, to frontal system or fluvial runoff from land. In the following descriptions, the focus will be on the smoothed (3 pt. mean) records, but larger decreases or increases in the non-smoothed records will also be commented. The census counts are grouped in species categories after Kucera (2007), based on their ecology and geographical distribution in the modern ocean. Grouping of species, or the "faunal zones" (Tolderlund and Be, 1971), share similarities with SST gradients, suggesting a strong relationship between SSTs and planktonic foraminiferal abundances (Kucera, 2007).

6.2.1 Polar species

The polar species found at ODP site 1233 consist of *N. pachyderma*, which is a species that dominates the polar waters in both hemispheres (Kucera et al., 2007).

N. pachyderma relative abundance (%)

Figure 6.5 displays the relative abundance of *N. pachyderma* at ODP site 1233 over the A2. The y-axis has been inverted to better show how changes in relative temperature are related to changes in relative abundance of *N. pachyderma*.

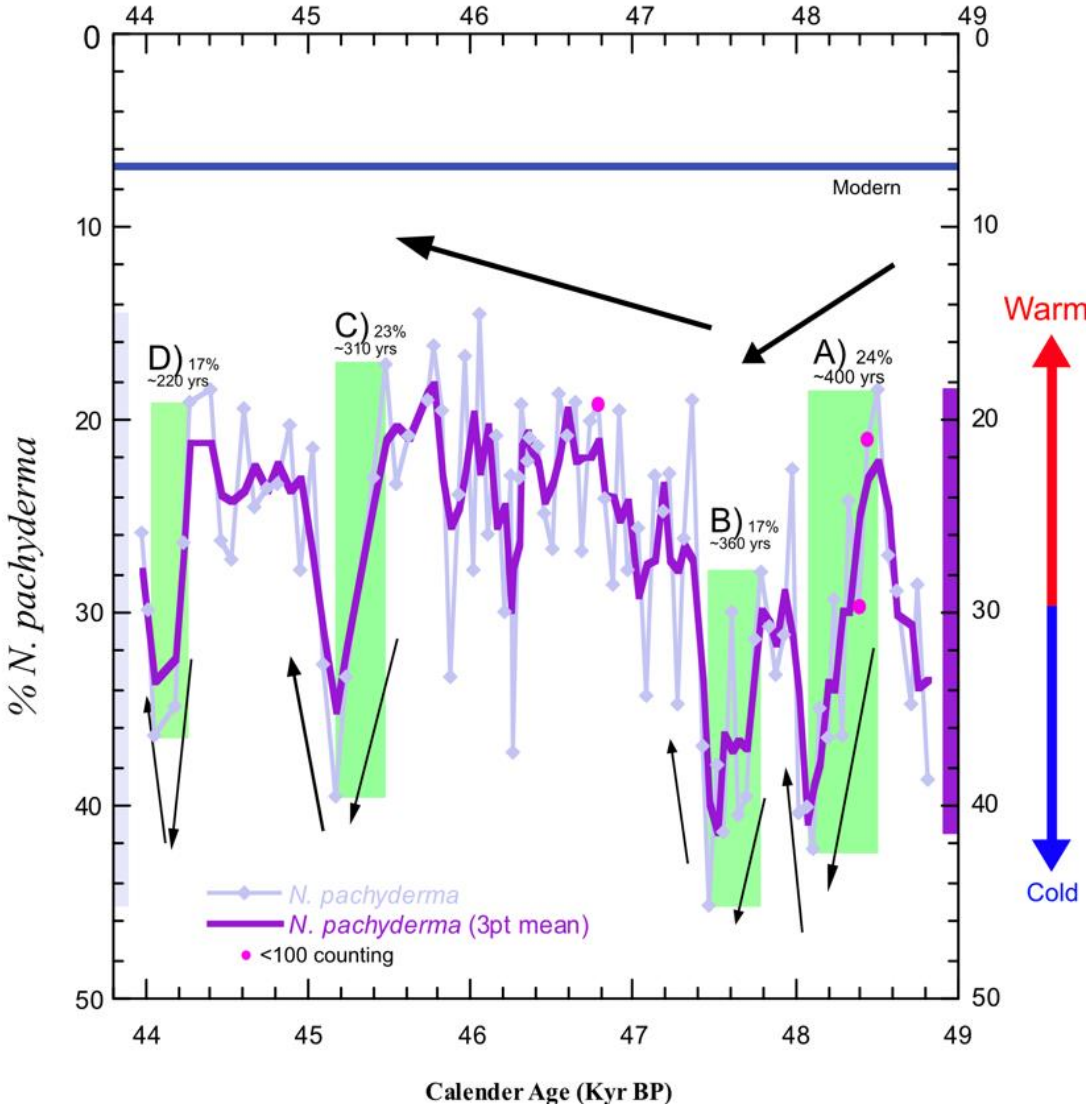

Figure 6.5: The relative abundance of *N. pachyderma* at ODP site 1233 plotted versus age (Kyr BP). The light purple line is the non-smoothed record, and the dark purple line is the smoothed (3 pt. mean) record. Pink circles represent samples where the total planktic foraminifera abundance was less than 100 species. The total range of variability in non-smoothed (left) and smoothed (right) values are shown on the y-axis in their respective colours. The Green vertical bars indicate intervals with the largest decreases in *N. pachyderma* abundance. The long black arrows represent long-term trends and shorter black arrows represent short-term trends. The red and blue arrows to the right represent the near surface temperature regimes based on the *N. pachyderma* abundance. The blue thick horizontal bar represents the modern day mean relative abundance of *N. pachyderma* (6.8 %) is based on core top data from core RR9702A-24MC-, close to ODP Site 1233 (Mix et al 1999).

The relative abundance of *N. pachyderma* in the non-smoothed record, range from ~14% (~46.1 Kyr BP) at its lowest, to ~45% (~47.4 Kyr BP) at its highest, a total range of ~41%. The smoothed (3 pt. mean) record has a value ranging from ~18% (~45.8 Kyr BP) at its lowest to 42% (~47.5 Kyr BP) at its highest, exhibiting a total range of ~24%. Rapid fluctuations in the percent values occur on multi-centennial scale, with superimposed more rapid smaller fluctuations occurring on centennial scale. The general trend of the relative abundance of *N. pachyderma* across the A2 is that of four distinct intervals where the abundance of *N. pachyderma* rapidly reach between 35-40%. In addition, there is a 2000-year interval from 47.4 to 45.4 Kyr BP and a shorter 800-year interval from 45 to 45.8 Kyr BP both with an average *N. pachyderma* abundance of ~25% and both with distinct superimposed 5-10% multi-centennial variability.

The green vertical bars on figure 6.5 highlights the four most prominent rapid increases in *N. pachyderma* relative abundance in the non-smoothed signal. The first two (A and B) occur early in the A2 interval, whilst the last two (C and D) occur late in A2. The first (A) rapid increase occurs from ~48.5 Kyr BP to ~48.1 Kyr BP, spanning ~400 years, with an increase of ~24% in *N. pachyderma* abundance. The second(B) increase starts at ~47.8 Kyr BP and peaks at ~47.4 Kyr BP with a rapid increase of 17% in *N. pachyderma* abundance that occurs in a two-step pattern over 360 years. The third (C) increase starts at ~45.5 Kyr BP and reaches its peak at ~45.2 Kyr BP spanning ~310 years with a total increase of ~23%. The fourth and final distinct increase (D) starts at ~44.3 Kyr BP and reaches its peak at ~44.5 Kyr BP, spanning ~220 years with a total increase of ~17%.

The increase in relative abundance of *N. pachyderma* from 48.5 to 48.1 contains two samples with less than 100 species counted (both at ~48.4 Kyr BP) and should consequently be more carefully interpreted. However, the lowest abundance (~22%) at the start of the first increase period (~48.5 Kyr BP) contained far more than 100 counted shells, providing a statistically robust lowest value.

6.2.2 Subpolar species

The subpolar species found in the A2 samples from ODP site 1233 consist of *N. incompta* and *T. quinqueloba.*

N. incompta relative abundance (%)

Figure 6.6 shows the relative abundance of *N. incompta* plotted versus age spanning the A2 warming interval. The non-smoothed signal displays a range from ~9% at ~44.2 Kyr BP, as its lowest, to as high as ~54% at ~45.6 Kyr BP, exhibiting a total range of ~45 %. The smoothed (3 pt. mean) exhibits a range of 34 % with ~14% at ~44.2 Kyr BP as its lowest, to ~48 % at ~45.6 Kyr BP as its highest value in the interval.

The general trend for the *N. incompta* counts spanning A2 starts with a distinct increase from 22 to 48% initiated at the start of A2 at 48.8 Kyr BP and spanning almost three millennia until ~46.2 Kyr BP. Superimposed on this trend is distinct multi-centennial scale variability with an amplitude of ~10% to ~15%. The interval with highest % values of *N. incompta* (46.2 to 45.6 kyr BP) exhibit a double peak with values close to 50%, separated by a short interval with a rapid drop (10%) in *N. incompta.* Between ~45.6 Kyr BP and ~44.0 Kyr BP, the *N. incompta* abundance exhibit a decreasing trend, interrupted by two distinct decreases at ~45.2 Kyr BP and ~44.3 Kyr BP respectively.

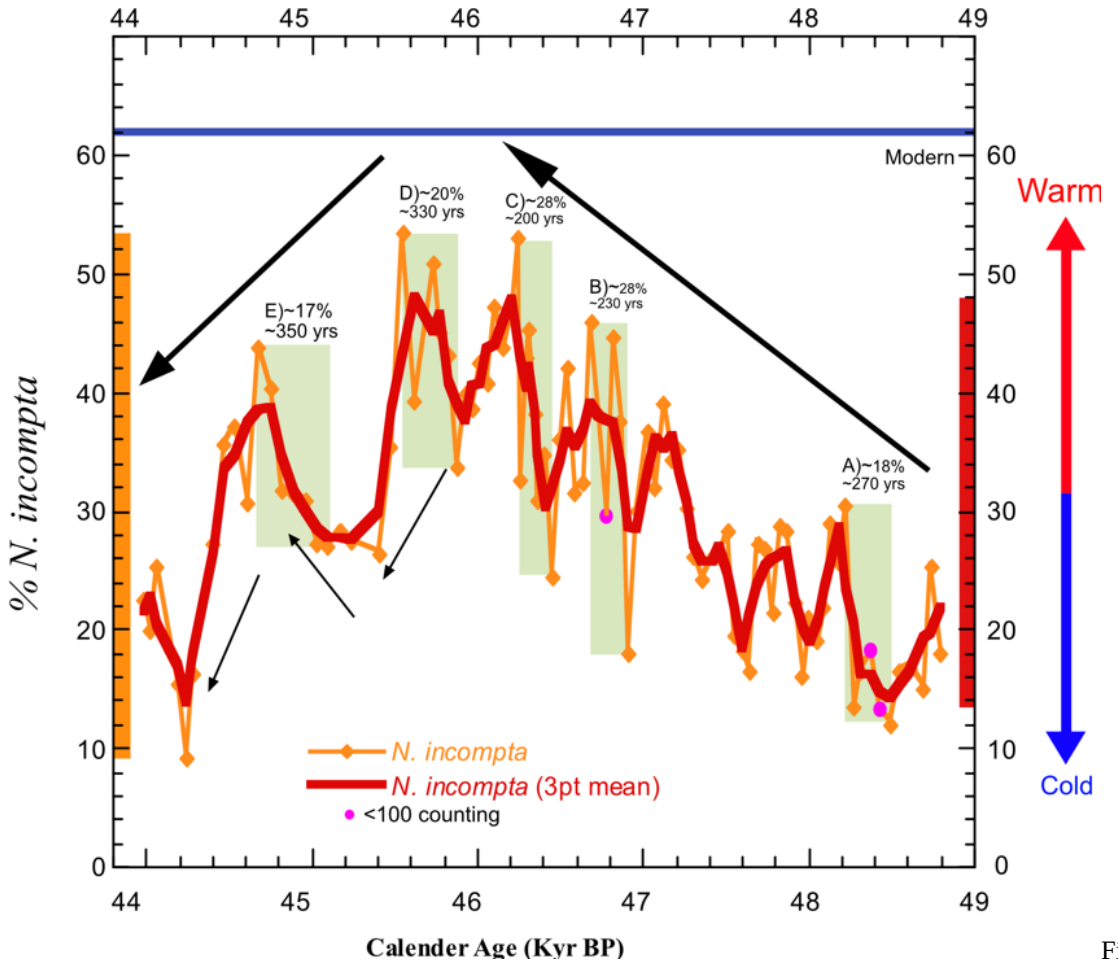

Figure 6.6: The relative abundance of *N. incompta* at ODP site 1233 plotted versus age (Kyr BP). The orange line depicts the non-smoothed record and the red line depict the smoothed (3 pt. mean) record, respectively. The pink circles represent small samples where the total planktic foraminifera abundance was less than 100 species. The total range of variability for the non-smoothed (left) and smoothed (right) values are shown on the y-axis in their respective colours. The light green vertical bars highlight the largest increases in *N. incompta* abundance. The long black arrows represent long-term trends, and the thin short black arrows represent shorter, more rapid trends. The red and blue arrows to the right represent the near surface temperature regimes based on the *N. incompta* abundance. The blue thick horizontal bar represents the modern day mean relative abundance of *N. incompta* (62 %) is based on core top data from core RR9702A-24MC-, close to ODP Site 1233 (Mix et al 1999).

In figure 6.6, the five green bars (A-E) highlight the five most distinct and most rapid increases in the relative abundance of *N. incompta*. The first three rapid increases (A-C) occur during the long-term increase (from ~44. to ~46.0 Kyr BP). These increases occur over ~200 - ~300 years and shows an increase of 18% to 28% in *N. incompta*. The fourth (D) increase punctuate the interval with highest abundance at ~46.0 Kyr BP, with a 20% increase in ~ 300 years. The fifth, and last marked increase occurs during the decrease in relative abundance of *N.*

incompta towards the end of A2. This last increase is at 45 Kyr BP and exhibit a 17% increase that takes place over ~350 years.

T. quinqueloba relative abundance (%)

Figure 6.7 shows the relative abundance of *T. quinqueloba* over the A2 event plotted versus age. *T. quinqueloba* is frequently used as a proxy for ocean front movements (Johannessen et al., 1994; Wright & Flower, 2002). For instance, increased abundances of *T. quinqueloba* has been used as an indicator for subantarctic and Antarctic water masses, and to infer the proximity of SAF/PF relative to core sites (De Deckker et al., 2012)

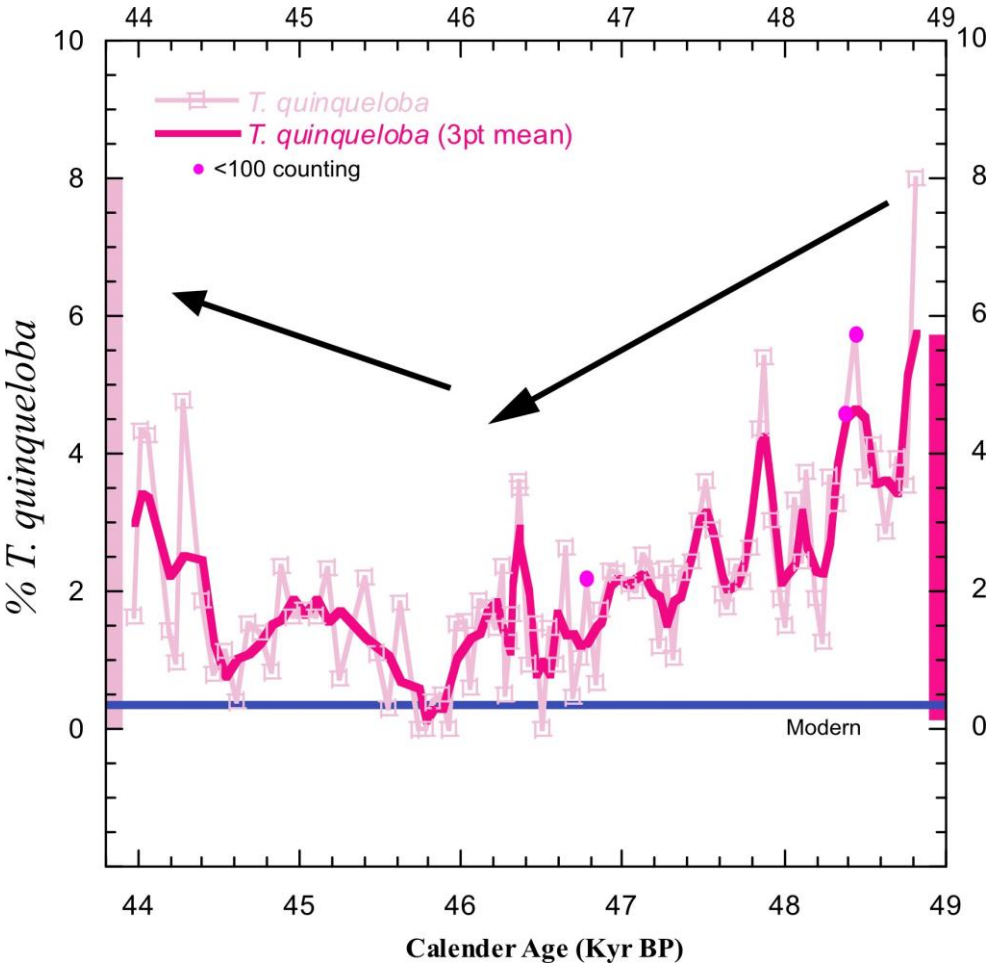

Figure 6.7: The *T. quinqueloba* relative abundance at ODP site 1233 plotted versus age (Kyr BP). The light pink line depicts the non-smoothed record and the pink line depict the smoothed (3 pt. mean) record, respectively. The pink circles represent small samples where the total planktic foraminifera abundance was less than 100 species. The total range of variability for the non-smoothed (left) and smoothed (right) values are shown on the y-axis in their respective colours. The black arrows represent long-term trends. The blue thick horizontal bar represents the modern day mean relative abundance of *T. quinqueloba* (0.8 %) is based on core top data from core RR9702A-24MC-, close to ODP Site 1233 (Mix et al 1999).

The relative abundance of *T. quinqueloba* at ODP site 1233 is relatively low and exhibit a variability between 0 to ~8%. The highest abundance of *T. quinqueloba* in the non-smoothed record is ~8% at ~48.8 Kyr BP, the start of A2. No *T. quinqueloba shells* was not present in the ODP 1233 samples at ~45.8, ~45.9 and ~46.5 Kyr BP.

The smoothed record displays a range from ~6%, at ~48.8Kyr BP to ~0% at 45.7 Kyr BP. The general trend of *T. quinqueloba* relative abundance in the study interval is initiated with a decreasing trend from ~48.8 Kyr BP to ~45.8 Kyr BP. Superimposed on this trend is high frequency, low amplitude variability. The frequency is on centennial timescales in the smoothed curve with amplitudes around ~1-~2%. At ~45.8 Kyr BP the *T. quinqueloba* relative abundance exhibit a slow increasing trend towards the termination of the A2 interval at ~44.0 Kyr BP. This trend ranges from the lowest value of ~0% relative abundance to ~3% relative abundance. There is also high frequency, low amplitude variability superimposed on this increasing trend.

6.2.3 Transitional species

Following the category of Kucera (2007), the transitional species thrive in a broad range of SSTs and are most abundantly found in the temperate regions (i.e., subpolar to subtropical). They are, *G. bulloides, G. glutinata, G. scitula and G. inflata.* The transitional species at ODP site 1233 found during this study consist of *G. bulloides, G. glutinata* and *G. inflata.*

G. bulloides **relative abundance (%)**

The relative abundance of *G. bulloides* at ODP site 1233 is often used as an indicator for upwelling and hence the changes in relative abundance downcore can indicate geographic displacement or changes in intensity for the upwelling along the Chilean coast near ODP site 1233 over the study interval.

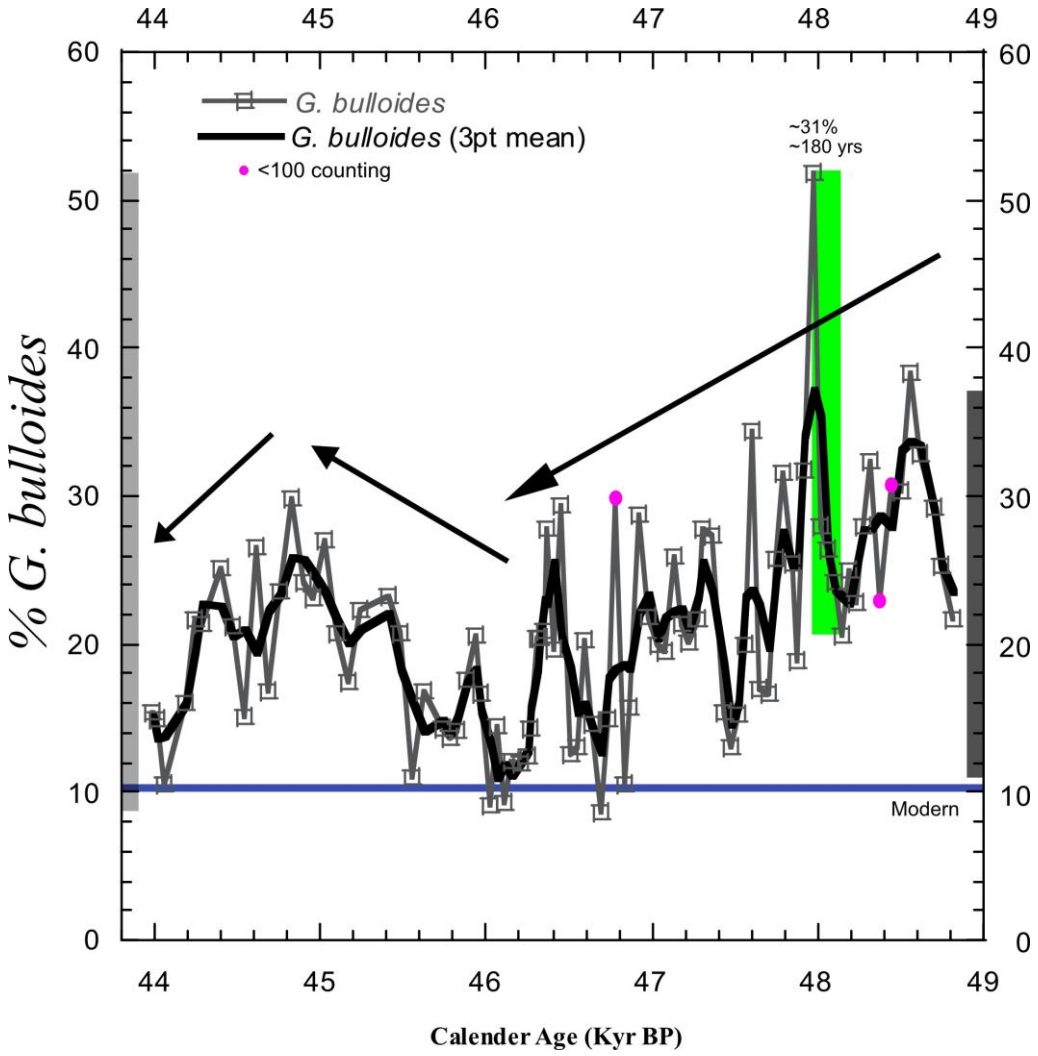

Figure 6.8: The *G. bulloides* relative abundance at ODP site 1233 plotted versus age (Kyr BP). The grey line depicts the non-smoothed record and the black line depict the smoothed (3 pt. mean) record, respectively. The pink circles represent small samples where the total planktic foraminifera abundance was less than 100 species. The total range of variability in the non-smoothed (left) and smoothed (right) values are shown on the y-axis in their respective colours. The green bars highlight the largest increase in *G. bulloides*. The blue arrows represent long term trends in the values. The blue thick horizontal bar represents the modern day mean relative abundance of *G. bulloides* (~10 %) is based on core top data from core RR9702A-24MC-, close to ODP Site 1233 (Mix et al 1999).

The non-smoothed record of the relative abundance of *G. bulloides* ranges from ~52% at ~48.0 Kyr BP, to as low as ~8% at ~46.7 Kyr BP, exhibiting a total range of ~44% spanning the A2 interval. The smoothed (3 pt. mean) record exhibit a range of ~26%, with a highest value of ~37% at ~48.0 Kyr BP and a lowest value of ~11% at ~46.1 Kyr BP.

The general trend of *G. bulloides* relative abundance at ODP site 1233 over A2 is like the trend of *T. quinqueloba.* Starting with a decrease in abundance from ~48.8 Kyr BP towards ~46.0 Kyr BP with centennial variability superimposed, exhibiting amplitudes varying from 2-10%. From ~46.0 Kyr BP to ~45.0 Kyr BP the abundance of *G. bulloides* increase, followed by a slight decreasing trend from ~45.0 Kyr BP to ~44.0 Kyr BP. Superimposed on this increase-decrease interval from 46.0 to 44.0 Kyr BP, are distinct centennial scale fluctuations with an amplitude of ~5%.

There is one very distinct and rapid peak in *G. bulloides* abundance over A2, which starts at ~21% (48.1 Kyr BP) and reaches its peak of ~52% over ~180 years (see green highlighted box in figure 4.9).

G. glutinata relative abundance (%)

Figure 6.9 show the *G. glutinata* relative abundance. *G. glutinata* is another indicator for nutrient-rich upwelling zone (Cayre et al., 1999; Naidu & Malmgren, 1996; Ottens & Nederbragt, 1992; Tolderlund et al., 1971). The highest value of *G. glutinata* is ~19% (~44.3 Kyr BP) and the lowest is ~1% (~46.8 Kyr BP).

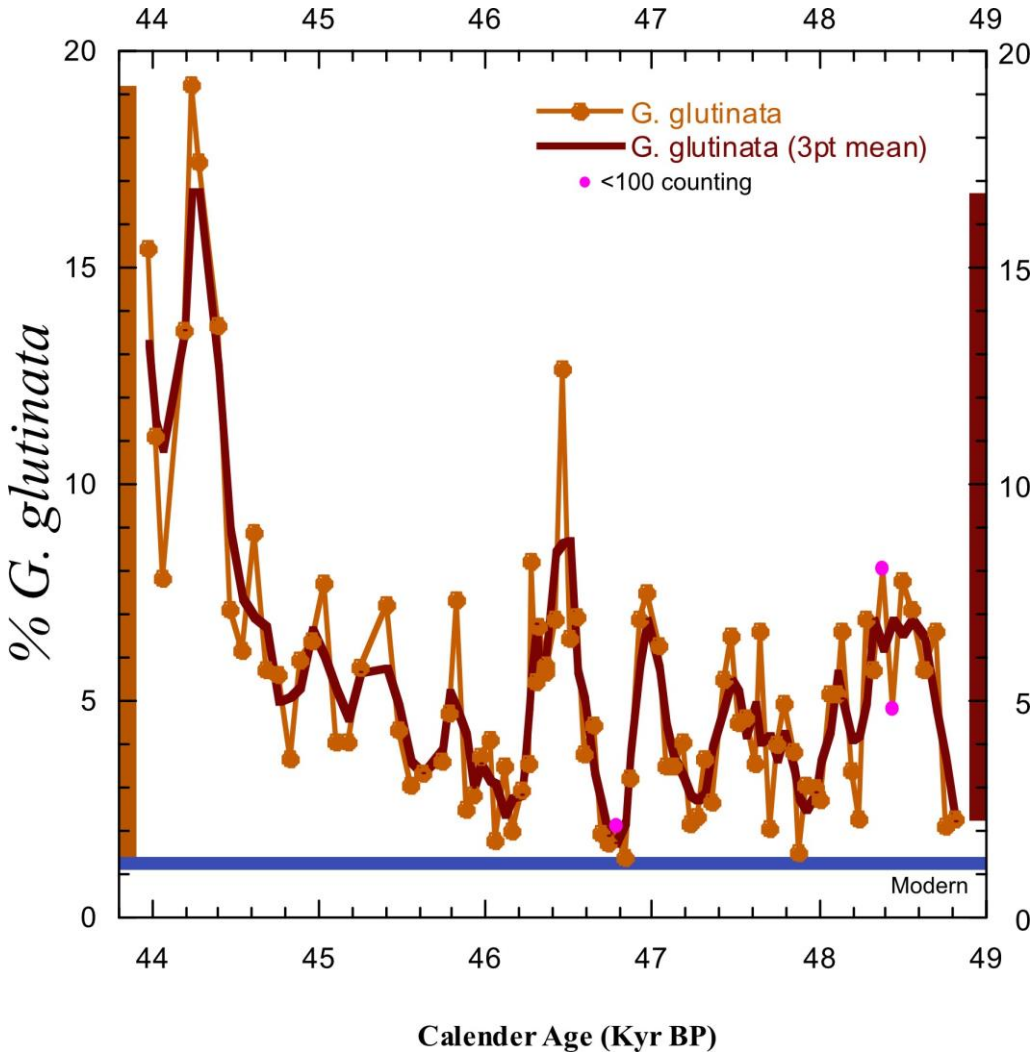

Figure 6.9: Th *G. glutinata* relative abundance at ODP site 1233 plotted versus age. The brown line represents the non-smoothed record, and the dark brown line represents the smoothed (3 pt. mean) record, respectively. The pink circles represent small samples where the total planktic foraminifera abundance was less than 100 species. The total range of variability in the non-smoothed (left) and the smoothed (right) values are shown on the y-axis in their respective colours. The blue thick horizontal bar represents the modern day mean relative abundance of *G. glutinata* (~1.1 %) is based on core top data from core RR9702A-24MC-, close to ODP Site 1233 (Mix et al 1999).

The smoothed (3 pt. mean) *G. glutinata* record exhibit centennial scale variability across the whole A2 interval, with varying amplitudes. From ~49.0 Kyr BP to ~44.6 Kyr BP the relative abundance varies repeatedly between values close to 1% and 8% in the smoothed (3 pt. mean) record. Near the termination of A2 (44.6 Kyr BP to 44.0 Kyr BP), there is an increase in the relative abundance, from ~6% at 44.6 Kyr BP to ~17% at ~44.3 Kyr BP.

G. inflata relative abundance (%)

Figure 6.10 shows the relative abundance of *G. inflata*. *G. inflata* thrive in nutrient rich upwelling zones at higher latitudes. The highest value of *G. inflata* in the study interval is ~25% (46.6 Kyr BP) and the lowest is ~1% (48.1 Kyr BP).

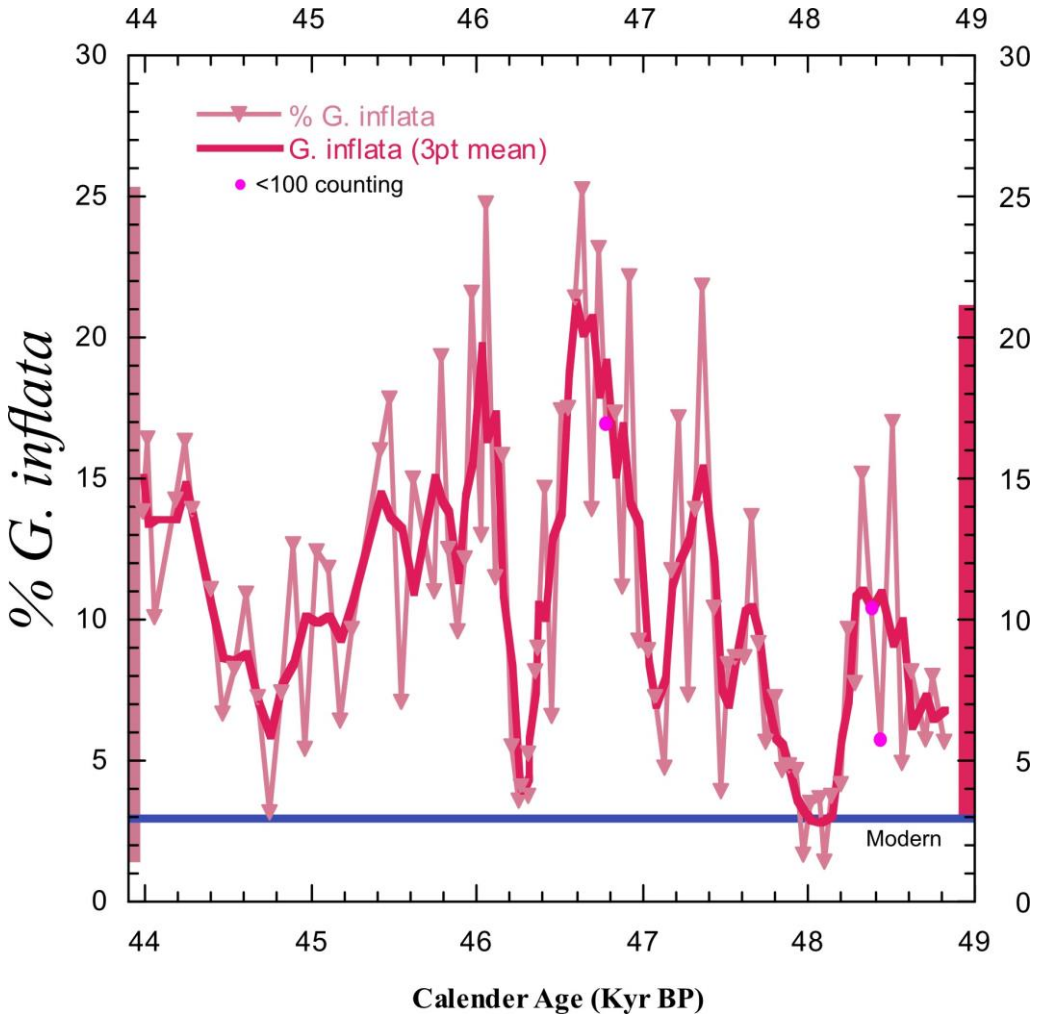

Figure 6.10: The *G. inflata* relative abundance at ODP site 1233 plotted versus age. The light pink line represents the non-smoothed record, and the pink line represents the smoothed (3 pt. mean) record, respectively. The pink circles represent small samples where the total planktic foraminifera abundance was less than 100 species. The total ranges are displayed in the y-axis with their respective colours for both the non-smoothed (left) and the smoothed (right) values. The blue thick horizontal bar represents the modern day mean relative abundance of *G. inflata* (~3 %) is based on core top data from core RR9702A-24MC-, close to ODP Site 1233 (Mix et al 1999).

The general trend of *G. inflata* exhibit large and variable abundance values throughout the study interval occurring on centennial time scales. There is a rise in values starting at near

modern abundances of 3% at ~48.0 Kyr towards 21% ~46.5 Kyr BP. This rise is punctuated by two distinct drops in abundances. The largest drop in G. *inflata* abundance is from 21% to 3%, which occurs over 300 years in the middle of A2 (~46.5 Kyr BP - ~46.2 Kyr BP). Following a rapid rise in abundance from 3% to 19 % over the next 200 years, the G. *inflata* abundance drops to 6% towards 44.4 Kyr BP with a slight increase towards the end of the study interval.

Combined planktic foraminifera species abundance (%)

In figure 6.11 all the planktic foraminifera counts done at ODP site 1233 over A2 are plotted versus age, including also the remaining planktic foraminifera (i.e., the transitional to subtropical species that are found in minor amounts), presented as «other planktic». From figure 6.11 it is evident that *N. pachyderma* exhibit low abundance, when *N. incompta* exhibits high abundance. This is also demonstrated in figure 4.13 (below) which shows the *N. pachyderma* sinistral (NPS) coiling ratio. However, the increasing trend in relative abundance of *N. incompta* occurs slower than the decreasing trend of N. pachyderm (from start of A2 until ~46.0 Kyr BP).

The *G. bulloides* and *T. quinqueloba* relative abundances shown in figure 6.11 also displays a similar pattern with a decreasing trend in the first half of A2 (49.0 Kyr BP - 46.0 Kyr BP), followed by an increasing trend in the last half of A2 (46.0 Kyr BP - 44.0 Kyr BP).

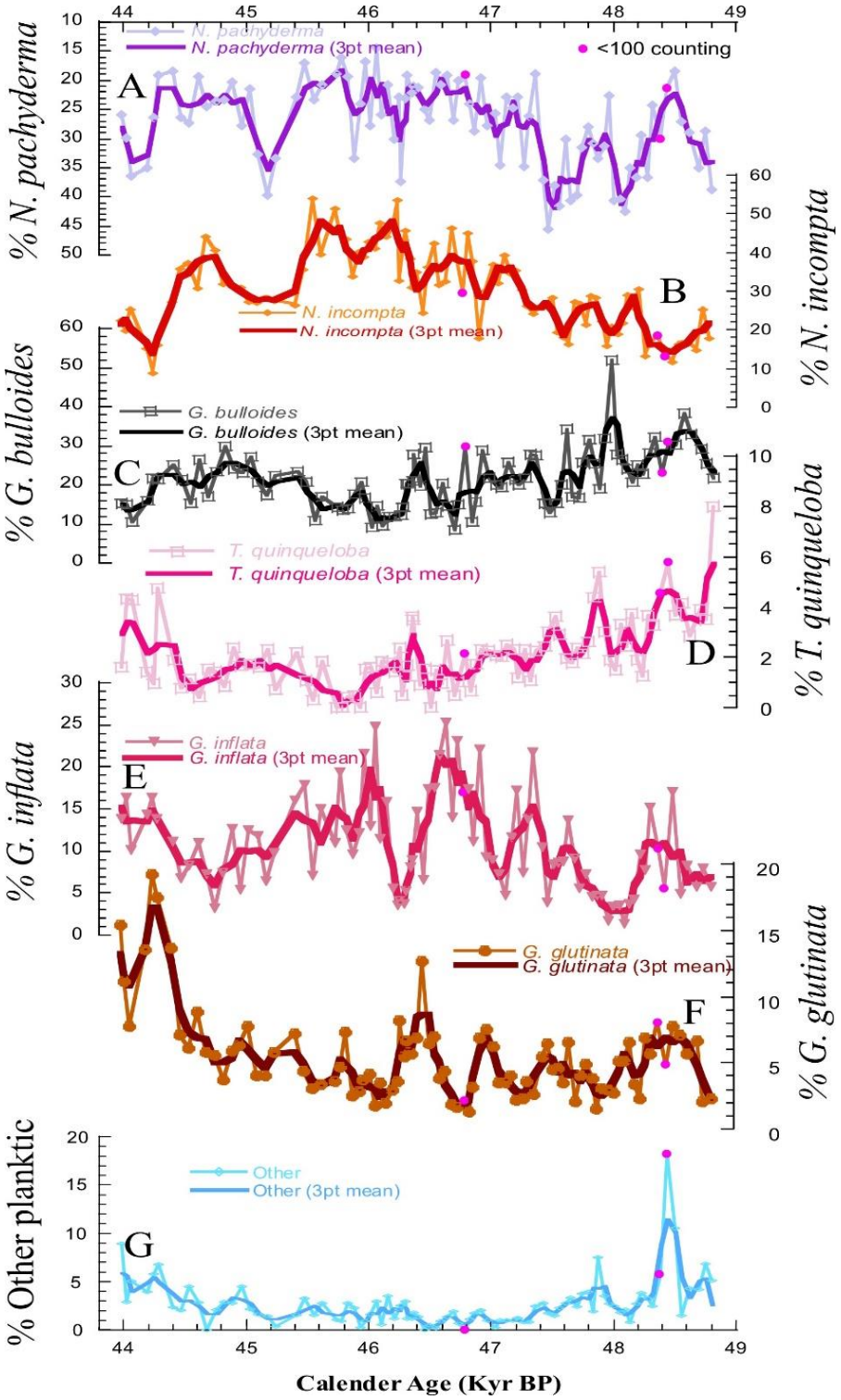

Figure 6.11: The planktic foraminifera species relative abundance at ODP site 1233 plotted versus age (Kyr BP): (A) *N. pachyderma* plotted in purple, (B) *N. incompta* plotted in red, (C) *G. bulloides* plotted in black, (D) *T. quinqueloba* plotted in light pink, (E) *G. inflata* (plotted in reddish pink, (F) *G. glutinata* plotted in brown and (G) Other planktic species (*Orbulina universa, Globorotalia crassaformis, Globorotalia scitula, Globorotalia truncatulinoides*) plotted in blue. The Non-smoothed records are in lighter colour and the smoothed (3 pt. mean) records are in darker colour. The pink circles in all data plots represent samples with less than 100 species counted.

Both *G. glutinata* and *G. inflata* exhibit high amplitude variability when *N. incompta* exhibit high values, across the middle of A2, but the high variability of *G. glutinata,* which can be observed near the termination of A2 does not correlate with the high *N. incompta* abundances.

G. bulloides and *T. quinqueloba* exhibit some small similarity with *N. pachyderma,* in that the highest abundance values of both species occur during high *N. pachyderma* abundance variability, and respectively, the lowest values of these species occur during low *N. pachyderma* abundances.

The other planktic counts are also presented in figure 6.11. These combine all other planktic foraminifera species which were counted in this study (excluding the most common species described in subsections 1-3) and consists of the transitional to subtropical species: *Orbulina universa, Globorotalia crassaformis, Globorotalia scitula, Globorotalia truncatulinoides* (see Kucera., 2007). The highest abundance of other species is recorded during the start (48.8 Kyr BP) and the termination (44.0 Kyr BP) of A2, and an overall low is recorded during the middle of A2, where the combined total of other species does not exceed 5%. It should be noted that two of the highest percentages of other planktic (these samples were dominated by *G. truncatulinoides*) are recorded in samples containing less than 100 planktic foraminifera, and therefore the peak observed at the start of A2 should consequently be interpreted more carefully.

6.3 *N. pachyderma* sinistral coiling ratio (%)

Figure 6.12 shows the *N. pachyderma* sinistral (NPS) Coiling ratio (%) plotted versus age (Kyr BP). NPS coiling ratio has been used as an SST proxy based on the observation that planktic foraminifera assemblage's changes with SST (Bauch et al., 2003), and is calculated as the percentage of sinistral coiling variety of *N. pachyderma* in total *N. pachyderma* (sinistral + dextral, i.e., *N. incompta* (Darling et al., 2006)). The y-axis has been inverted to better display how changes in NPS coiling ratio indicates changes in SST.

The NPS coiling ratio plotted in Figure 6.12 exhibits high frequency variability over the A2 study interval. The non-smoothed record shows a total range of ~47% with its lowest value of ~ 26% (~45.8 Kyr BP) and its highest value of ~73% (~44.2 Kyr BP). The smoothed (3 pt. mean) shows a range from ~28% (~45.8 Kyr BP) to ~67% (~44.2 Kyr BP), providing a

total range ~39%. There is centennial variability present both during the high (cold) intervals as well as the low (warm intervals). The general trend of the smoothed (3 pt. mean) NPS coiling ratio exhibit generally high values with centennial scale variability from ~48.8 to ~47.6 Kyr BP after which there is a transition to low values. Superimposed on this decreasing trend are fluctuations with distinct centennial scale frequency with ~5 - ~10% amplitude. Starting at ~45.8 Kyr BP the NPS coiling ratio exhibit a multi-millennial increase with a two-step rise back to high values. The dominating centennial scale variability is clearly visible in both the smoothed (3 pt. mean) record and the non-smoothed record.

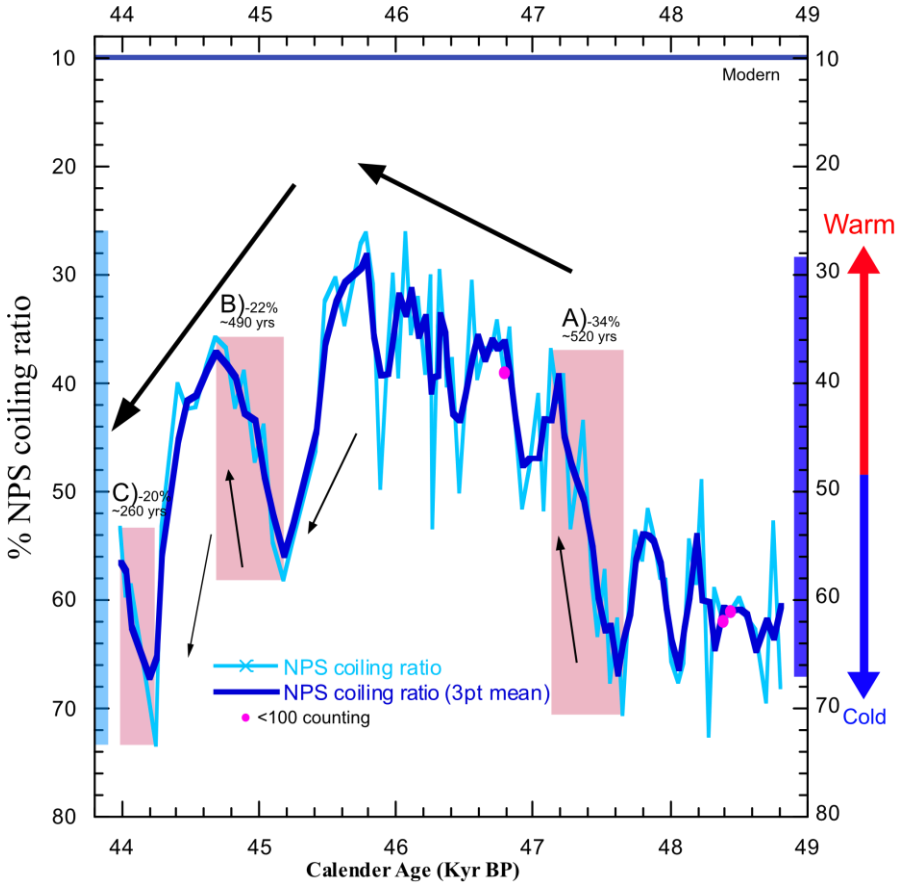

Figure 6.12: Changes in NPS coiling ratio at ODP site 1233 plotted versus age (Kyr BP). The light blue line depicts the non-smoothed record and the dark blue line depict the smoothed (3 pt. mean) record, respectively. The pink circles represent small samples where the total planktic foraminifera abundance was less than 100 species. The total range of variability in the non-smoothed (left) and smoothed (right) values are shown on the y-axis in their respective colours. The red bars highlight the largest decreases observed in the NPS coiling ratio. The large black arrows represent long-term trends, whereas the smaller black arrows represent short-term trends. The red and blue arrow on the right represent relative temperature changes indicated by the NPS coiling ratio. The blue thick horizontal bar represents the modern day mean relative NPS coiling ratio (10 %) and is based on core top data from core RR9702A-24MC-, close to ODP Site 1233 (Mix et al 1999).

During A2 there are three short term, multi-centennial scale, with high amplitude decreases which is marked with red bars in figure 6.12 (A-C). The first distinct decrease(A) starts at ~47.7 Kyr BP and ends at ~47.1 Kyr BP, spanning ~520 years with a decrease of ~34 %. This major decrease is superimposed on the already decreasing trend which happens during the first half of A2. The two last distinct decreases (B and C) in NPS coiling ratio happens during the increasing trend during the last half of A2 (~45.2 Kyr BP and ~44.2 Kyr BP). They are a part of the distinct two-step millennial scale fluctuations over this interval and occur over ~ 490 (B) and 260 years (C), with a decrease in coiling ratio of 22 % and 20% respectively.

6.4 Ice rafted debris (IRD) counts (%)

Figure 6.13 displays the abundance of IRD at ODP site 1233 plotted versus age. The IRD abundance is very low throughout the entire study interval, and most of the samples did not contain any lithic grains. The highest abundance of IRD is ~3.6%, at ~45.6 Kyr BP, exhibited in the non-smoothed record in figure 6.13.

The general trend of the IRD record starts with low values from the start of A2 (~48.8 Kyr BP) to ~47.0 Kyr BP. At ~47.0 Kyr BP there is a gradual increase and IRD peaks in abundance at ~45.5 Kyr BP (3.6%). At ~45.5 Kyr BP IRD abundance decreases again back to values near zero at ~44.9 Kyr BP. From ~44.9 Kyr BP there are no traces of IRD at ODP site 1233 over the remainder of A2.

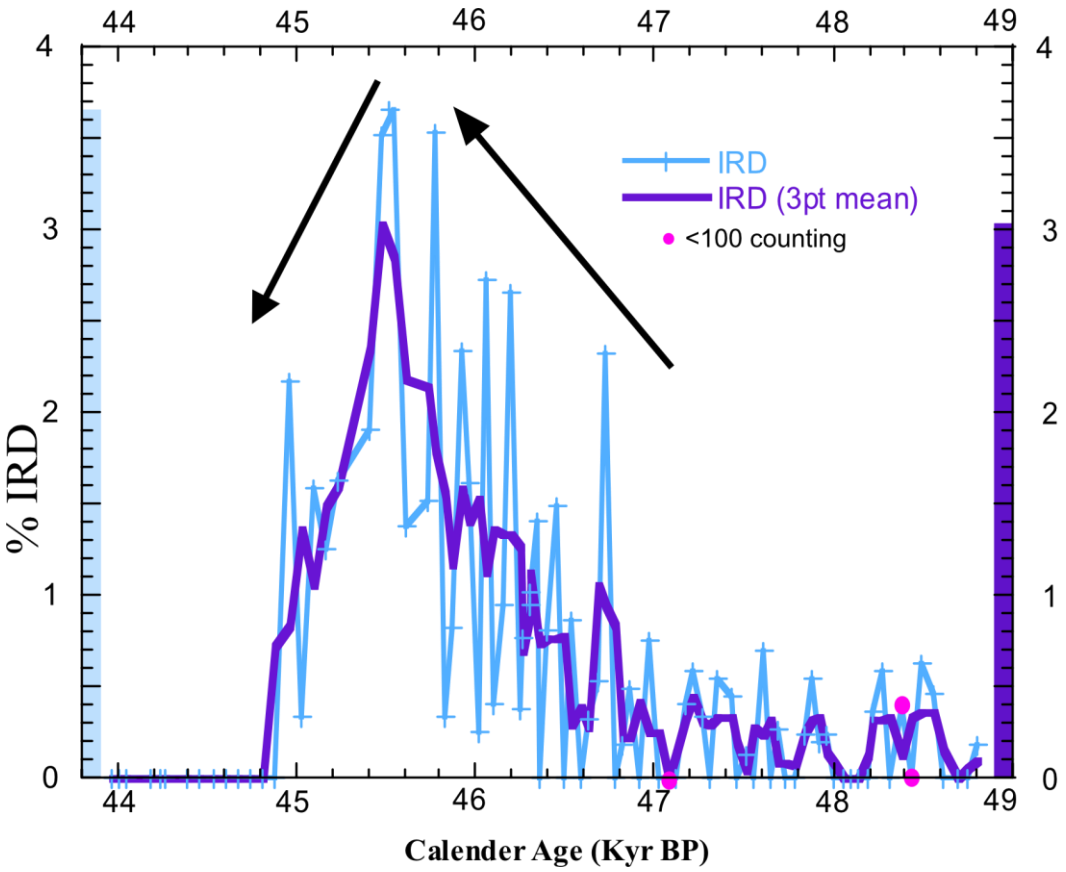

Figure 6.13: The IRD record at ODP site 1233 plotted versus age (Kyr BP). The light blue line shows the non-smoothed record and the purple line show the smoothed (3 pt. mean) record, respectively. The pink circles represent very small samples where the total planktic foraminifera abundance was less than 100 species. The total range of variability in the non-smoothed (left) and the smoothed (right) values are shown on the y-axis in their respective colours.

7. Discussion

In this chapter the data produced during this study will be interpreted and discussed together with previous results at ODP Site 1233 and in the broader region (SE Pacific). Foraminiferal assemblages and stable isotope data indicates large temperature and climate variability in the SE pacific during the A2 warm event. Temperature proxies from this study are highly consistent with temperature proxies from other studies suggesting the results provide robust constraints on past temperature changes.

Consistent with the result chapter, the data will be presented with a 3 pt. mean smoothing, while the isotope data from prior studies (Euler 2010, Førde 2008) will be plotted with a 5 pt. mean due to higher resolution in those data (4cm spacing vs 8cm in this thesis).

7.1 Surface Ocean and climate variability

ODP Site 1233 off the western coast of Chile, is an ideal core location for studying surface ocean and climate variability in the Southeast Pacific. Ocean properties at the study area are strongly controlled by the tropical front movements, upwelling along the coast and large amount of runoff from the continent from rivers and glaciers. All these factors may change the temperature, nutrient concentrations, and salinity in the ocean, causing changes in the planktonic foraminiferal assemblages.

7.1.1 Modern abundances

In order to understand how the climate and environment during the A2 interval was different when compared to today, we start with a closer look at modern foraminiferal assemblages derived from core top data in SE Pacific (Kucera et al., 2005). Figure 7.1 shows the modern-day distribution of the most significant planktonic foraminiferal species (that was selected and counted in this study) in the present-day South Pacific.

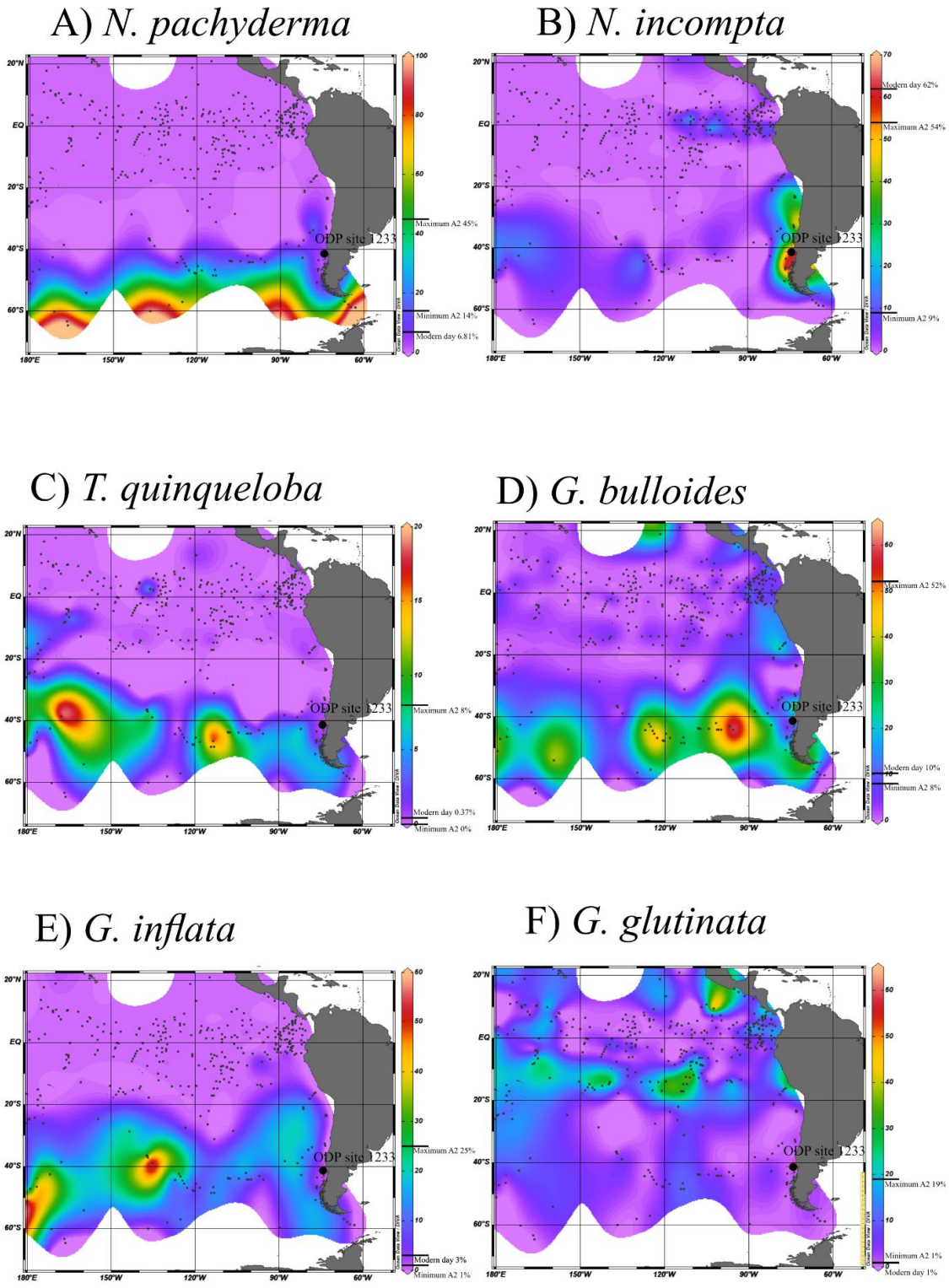

Figure 7.1: Maps of modern distributions of planktonic foraminifera assemblages in the SE Pacific (after Kucera et al., 2005). A) *N. pachyderma* B) *N. incompta* C) *T. quinqueloba* D) *G. bulloides* E) *G. inflata* F) *G. glutinata*. The maps were plotted using Ocean Data View (R. Schlitzer, 2021) ODP Site 1233 is marked with a black circle. Small black dots mark the locations of core top samples used in the MARGO Project planktonic foraminifera census count database for the modern Pacific Ocean (Kucera, Weinelt, Kiefer, Pflaumann, Hayes, Weinelt, Chen, Mix, Barrows, Cortijo, et al., 2005a)

Polar species

Figure 7.1A shows a relatively low abundance of the polar species, *N. pachyderma* at Site 1233 (6.8%), and increasing abundance further south towards Antarctica, displaying a strong association with temperature and its latitudinal gradient in the SE Pacific. The modern annual mean SST of 14°C at Site 1233 (WOA, 2018) is above where *N. pachyderma* thrives, which is consistent with such low values today when compared to values up to 45% during A2 (fig. 6.6). If *N. pachyderma* is only interpreted as a temperature proxy, this suggests a drastic cooling at Site 1233. Indeed, a similarly high abundance of *N. pachyderma* (as during A2) is found at 60°S in the modern Southern Ocean.

North of Site 1233, there is an area with higher abundances (closer to 20%), which is the same area which the upwelling zone is situated today. This increased abundance in the upwelling zone indicates that *N. pachyderma* thrives in cooler upwelling regions, and, like temperature, can deviate from the general N-S pattern due to local processes. *N. pachyderma* has been found to migrate and dwell much deeper in upwelling zones (Darling et al., 2017; Ivanova et al., 1999) when compared to polar regions, and Wu and Hillaire-Marcel (1994) suggests one reason for this is temperatures closer to optimum range. The potential for *N. pachyderma* to occupy a deeper dwelling habitat (e.g., in upwelling zones) must be considered when comparing assemblage results with the alkenone based SST reconstructions at Site 1233 from Kaiser et al., (2005, 2007).

Subpolar species

The modern annual SST of 14°C at Site 1233 (WOA, 2018) is much better suited for the subpolar *N. incompta* than for the polar *N. pachyderma*. The high abundance from core top data seems to be heavily related to the high amount of land derived nutrients due to extremely high precipitation of the Chilean coast (Mohtadi et al., 2005), displayed in figure 7.1B as a high abundance in the regions most influenced by continental runoff (cf precipitation information in background chapter) and a sharp decrease further offshore. Today's abundance

(60%) is higher than that found in A2 (average of ~30%) suggesting A2 was less ideal for *N. incompta* relative to today, or relative to other species.

The subpolar species *T. quinqueloba* shows very low abundance from core top data close to Site 1233. Annual SSTs near Site 1233 today is around 14˚C (WOA, 2018) and probably too high for *T. quinqueloba* to thrive. Further south, near the boundary to the Southern Ocean, there are locations of higher *T. quinqueloba* abundance (Figure 7.1c). In the Southern Ocean the abundance is reduced to nearly zero, probably due to near total dominance of *N. pachyderma*.

Transitional species

The transitional species *G. bulloides* displays a modern abundance of 10% close to Site 1233. From fig. 7.1d it is evident that *G. bulloides* thrives north of Site 1233, where the modern-day upwelling cell is located, as expected given its frequent use as an upwelling indicator (Thiede, 1975; Sautter & Thunell, 1991; Spero & Lea, 1996). *G. bulloides* might be skewed towards upwelling conditions and less towards mean conditions if it favors an upwelling habitat. *G. bulloides* also displays higher values south and west of Site 1233 which may indicate that the modern ocean properties at Site 1233 is not ideal for *G. bulloides*.

Both *G. inflata* and *G. glutinata* show very low percentages (1%) in the modern core top database close to Site 1233. *G. inflata* displays higher values further off the coast, indicating a more suitable environment offshore. Fig. 7.1f shows that *G. glutinata* favours warmer waters, found in higher abundances to the north, between 20˚S and the equator.

7.1.2 SSTs and planktonic foraminiferal assemblages during A2.

Increased nutrient availability

The *N. pachyderma* % exhibit large fluctuations on multi-centennial scale during the study interval, and both the highest and lowest abundance occurs during times of high SSTs (alkenones, planktonic δ^{18}O, Fig. 7.2). This provides further indication that *N. pachyderma* % variations may not solely reflect temperature (at the surface) but that also other hydrographic properties influence its abundance. Previous studies have suggested *N. pachyderma* to be an indicator for upwelling at the coast of Chile (Mohtadi and Hebbeln, 2004; Mohtadi et al., 2005). In order to assess this possibility (and whether *N. pachyderma* peaks over the A2 reflect increased upwelling), the timing of *N. pachyderma* peaks are compared to other indicators of climate and environmental conditions such as the abundances of the upwelling favouring species *G. bulloides* and *T. quinqueloba*, as well as planktonic (*G. bulloides* and *N. incompta*) and benthic (*C. wuellerstorfi* and *U. peregrina*) foraminiferal δ^{13}C records.

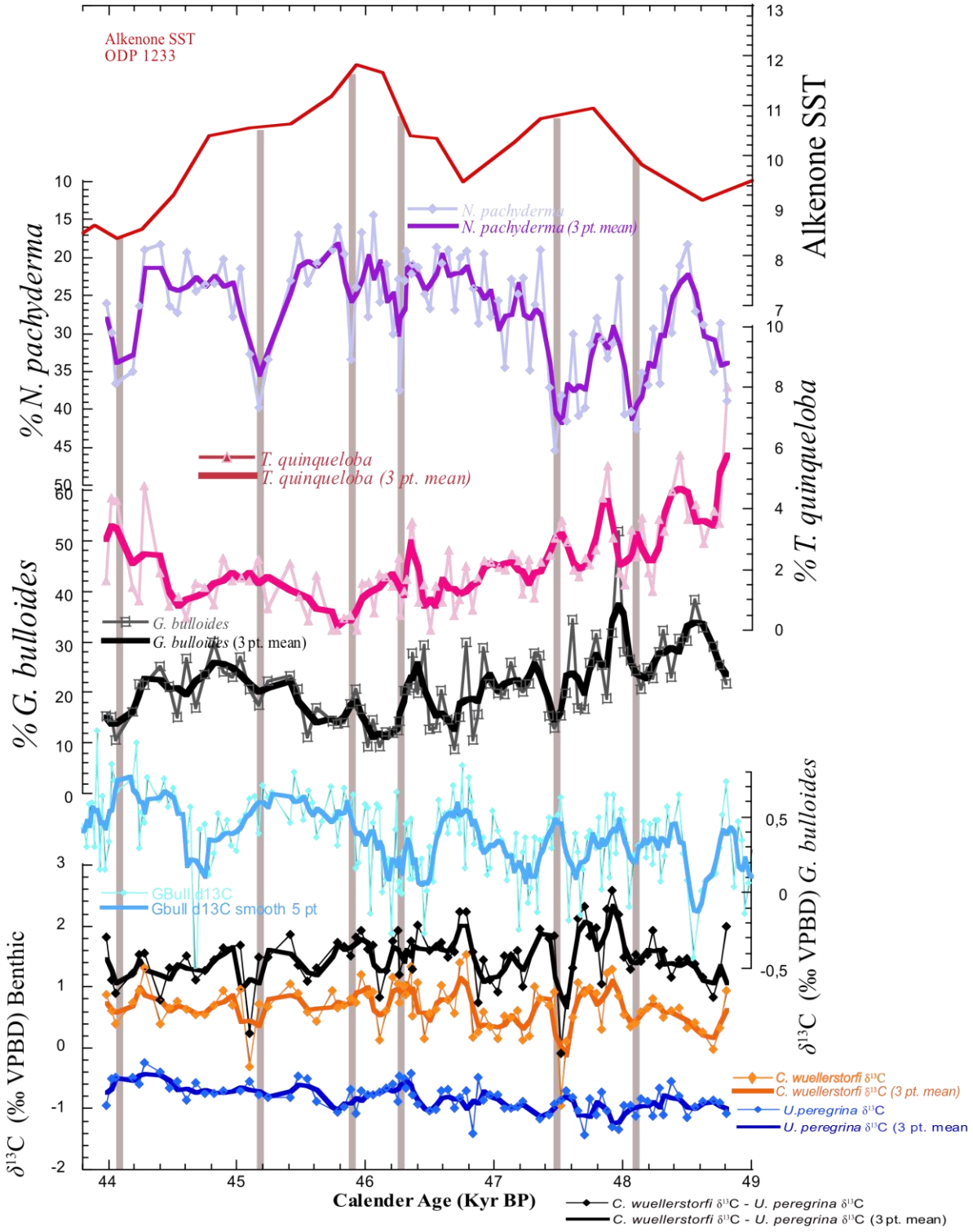

Figure 7.2: Alkenone SST (Kaiser et al., 2005) (red) plotted together with N. Pachyderma% (purple), T. quinqueloba (pink), G. bulloides (black), $\delta^{13}C$ records of G. bulloides (light blue), benthic $\delta^{13}C$ records (C. wuellerstorfi (orange) and U. peregrina (blue)) and the difference between the two benthic records (black). Gray columns mark the *N. pachyderma* % peaks.

Here we explore six distinct peaks in the *N. pachyderma* % record for indications of upwelling. The first distinct *N. pachyderma* peak (48.1 Kyr BP) could indicate upwelling conditions (higher *G. bulloides* % and lower planktonic and benthic $\delta^{13}C$ indicating increased nutrients due to upwelling). However, the reminding peaks (~47.5 Kyr BP, ~47.0 Kyr BP, ~46.3 Kyr BP, ~45.2 Kyr BP and ~44.1 Kyr BP) does not share this coherent behaviour between the different proxies. In general, there seems to be no coherent signal between the upwelling indicators, which suggests that upwelling conditions at Site 1233 during A2 was unlikely. This is in line with previous studies which claim that the upwelling region at 38°S never migrated to Site 1233 during MIS 3 (Martinez et al., 2006; Pisias et al 2006).

However, *G. bulloides* and *T. quinqueloba,* which are subpolar species, are found in higher abundances throughout the A2 than in the modern ocean, even though temperatures are lower over A2. Hebbeln et al. (2000a) suggest that the high nutrients/low chlorophyll levels found south of 40°S makes the conditions at Site 1233 better suited for *G. bulloides*. The higher nutrient levels found at Site 1233 (Hebbeln et al., 2000a) can be explained by a closer proximity to SAF (fig. 7.3) where eddy fluxes increase the nutrient availability (Straub, 1993; Munday et al., 2013). Increased *T. quinqueloba* abundances (together with increased *N. pachyderma,* which has proved to also indicate closer proximity to fronts (De Deckker et al., 2012)) can indicate a SAF that is more proximal to the core location. High *T. quinqueloba* % at the start and during the termination of A2 may indicate that SAF was most proximal to Site 1233 during the coldest periods, and has shifted slightly poleward during the A2 warming, consistent with slightly southward atmospheric shift during warm intervals (Kohfeld et al., 1996; Pisias et al., 2006; Lamy et al., 2007; Kaiser et al., 2005).

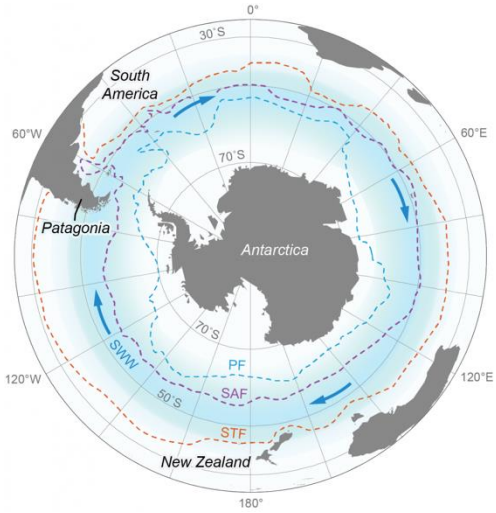

Figure 7. 3. Westerly Winds and ocean fronts around Antarctica. PF (Polar Front) SAF (Subantarctic Front). STF (Subtropical Front) SWW (southern Westerly Winds) (Antarcticglaciers.org)

This puts some limits on potentially where the SWW were positioned during A2 since today's wind location results in upwelling just to the North of the core location (~41°S) as well as within the Antarctic divergence, far to the south. Although the position of the winds is difficult to determine, both a northward and southward shift have been suggested based on models and proxy data alike (Kohfeld et al., 1996; Pisias et al., 2006; Lamy et al., 2007; Kaiser et al., 2005). Our fauna results suggest that the winds, and related upwelling zone, were likely not to the south of their current position. Instead, the general increase in polar species (*N. pachyderma*) and nutrient favouring species (*G. bulloides*) over A2 (relative to today) suggest the circumpolar current and its related fronts (increased *T. quinqueloba* and *N. pachyderma*) and nutrients, were closer to the site, consistent with a modest equatorward shift in the westerlies which the majority of previous studies suggest (Kohfeld et al., 1996)

N. incompta variability.

The *N. incompta* abundance does show increased values during A2, as is expected for increasing temperature. In addition to temperature influences, *N. incompta* displays high relative abundance in modern day Chilean coast regions (fig. 7.1B**)**, which has low sea surface salinity, due to high runoff from the continent. During PIS meltwater fluxes, large amounts of sediment may reduce the abundance of *N. incompta* (Kaiser et al, 2007). However, meltwater pulses with lower amounts of sediment, containing land driven nutrient, may indeed increase

abundance in *N. incompta* for the same reason it thrives proximate to the Chilean coast today (Mix et al., 1999).

As mentioned previously, Euler (2010) proposed that the $\delta^{18}O$ *G. bulloides* variability is due to a roughly equal mix of changes in temperature and in the $\delta^{18}O_{seawater}$ (e.g., local salinity changes). As *G. bulloides* is a near surface dweller, it may be the best available recorder of changes in $\delta^{18}O_{seawater}$ in surface waters over A2. Since glacial meltwater has a very low $\delta^{18}O$ signal, Euler (2010) and Johnsen (2019) suggest that the large fluctuations in the $\delta^{18}O$ record from *G. bulloides*, relative to those recorded in other species, may be indicative of meltwater fluxes from the nearby PIS. However, Euler (2010) also points out that the Fe signal (Kaiser et al., 2005, 2007) and the $\delta^{18}O$ signal from *G. bulloides* in Site 1233 does not match and claims that this can be related to particularly strong sediment fluxes during times when the PIS was large and proximal to the core site.

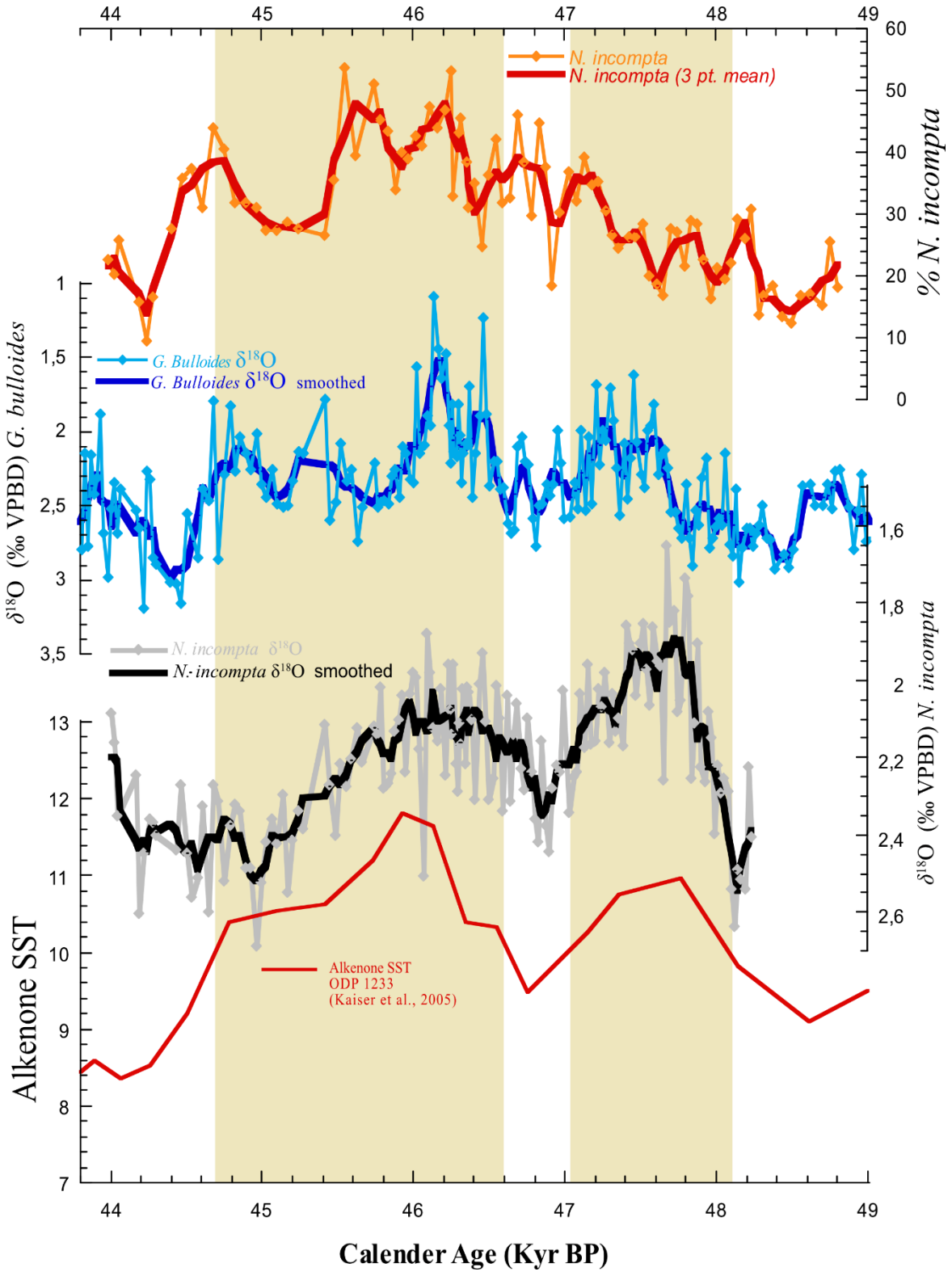

Figure 7.3: From top: *N. incompta % of total assemblage* (red) plotted together with *G. bulloides* δ^{18}O (blue), *N. incompta* δ^{18}O (black) and alkenone SST (red). The two shaded areas show Alkenone SST above 10˚C.

Figure 7.3 displays the *N. incompta* % record and *G. bulloides* δ^{18}O record and reveals several intervals that exhibit a negative covariance between *N. incompta* % and *G. bulloides* δ^{18}O

values. This would be consistent with a common influence on both records by freshwater (and glacial meltwater) runoff, decreasing *G. bulloides* δ^{18}O and increasing *N. incompta* %. Interestingly, the *N. incompta* δ^{18}O record shows strong similarity to the alkenone SST record suggesting that, despite its preference for near coastal sites with potential influence of freshwater, temperature may still exert a dominant control on its isotopic composition. Indeed, the temperature changes of 2-3° indicated by alkenones over the twin peaks of the A2 warming event would be sufficient to explain nearly all the oxygen isotopic variability (0.4-0.6‰) observed in the record. This suggests that *N. incompta* δ^{18}O records near sea surface temperature better than *G. bulloides* δ^{18}O during A2 consistent with the findings of Euler (2010).

Coiling ratio as a temperature proxy

The Coiling ratio between *N. pachyderma* and *N. incompta* (*N. pachyderma* /(*N.pachyderma+N.incompta*)) have been successfully used as a SST proxy ((Bauch et al., 2003) in the North Atlantic Ocean. However, both *N. pachyderma* and *N. incompta* is strongly influenced by nutrient-rich waters and meltwater as discussed above. From Figure 7.4 it is evident that the coiling ratio% shows large differences from *N. incompta* δ^{18}O and alkenone SST.

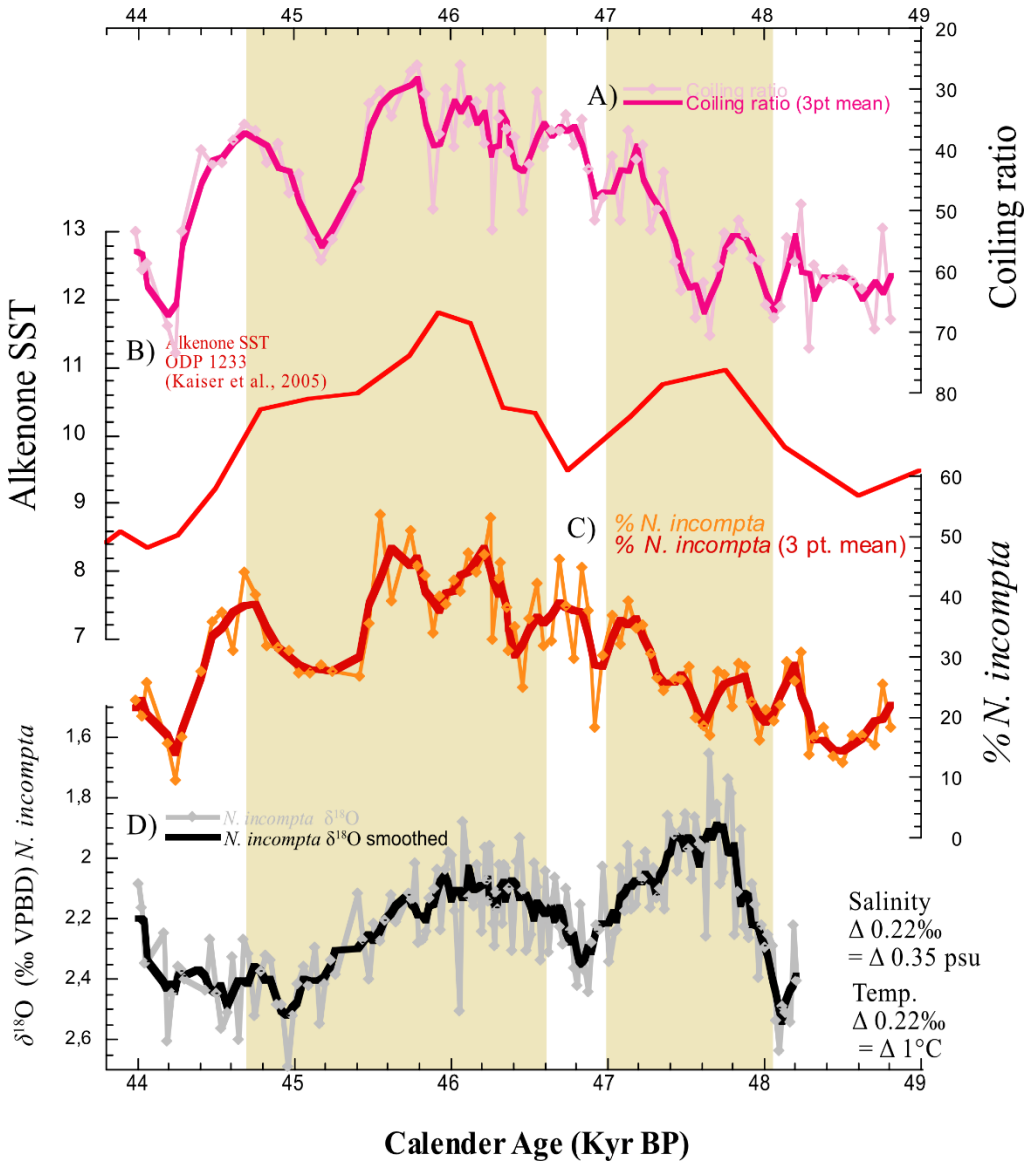

Figure 7.4: A) Coiling ratio% (*N. pachyderma*/(*N.pachyderma+N.incompta*)) (pink) plotted together with B) Alkenone SST (red), C) *N. incompta* (red/orange) and D) *N. incompta* δ^{18}O (black). The two shaded areas show Alkenone SSTs above 10˚C.

The high SST in alkenone and planktonic δ^{18}O minima at ~47.5 Kyr BP is happens at the same time as one of the highest coiling ratios %, which is the opposite of expected, if the coiling ratio is only related to SST. The data does however show SST warming from ~47.0 Kyr BP to ~45.5 Kyr BP, but this interval does not share a similar pattern as the alkenone SST and δ^{18}O record of *N. incompta*. The dissimilarity (with planktonic δ^{18}O and alkenone SST) suggests a non-temperature overprint that must be due to other hydrographic factors.

7.2 Climate variability and Patagonian Ice Sheet (PIS) fluctuations over A2

Today, the Patagonian Icefields are experiencing the quickest mass loss of all the major icesheets in the world (IPCC, 2021; IPCC, 2019) and is a major contributor to rising global sea level the last 50 years (Zemp et al., 2019). This is a result of the ongoing global warming, which increases both sea and air temperature (IPCC, 2019). The primary conditions shaping the Patagonian Icefields are a complex mix of precipitation, strong westerlies, and Andean topography (Sagredo and Lowell., 2012; Bravo et al., 2021), and understanding these processes are crucial for predicting how the Patagonian Icefields will respond to future climate change. Given the short period of time we have direct observations of the glacier, we must rely on paleo reconstructions back in time to the last glacial period to study the Patagonian Ice Sheet (PIS) and learn how the ice responded to different climatic forcings.

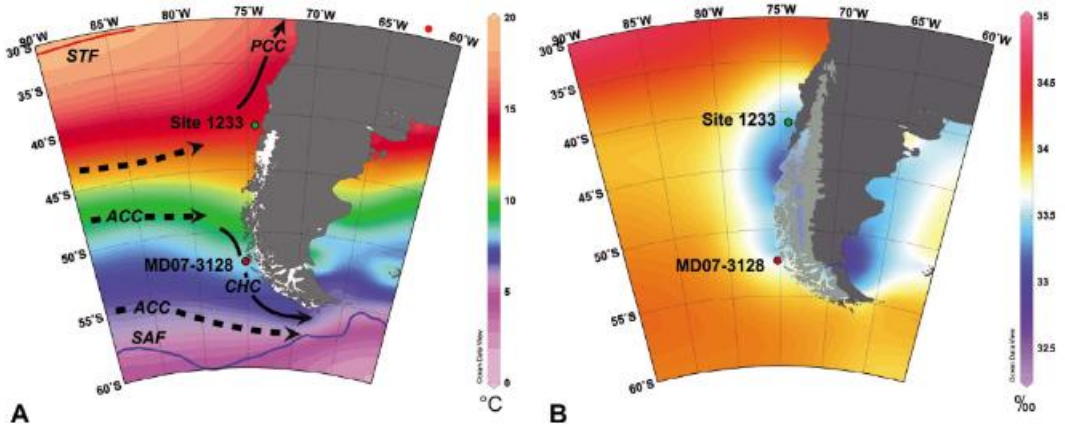

Figure 7.5 Core setting for ODP Site 1233 versus the PIS and major oceanic frontal systems: A) modern ocean surface circulation after Strub et al. (1998), with mean annual SST (WOA 2009) with the modern-day Patagonian Icefields in white. B) Annual sea surface salinity in the SE pacific. Maximum extent of PIS in grey (Hollin and Schlling. 1981). Figure after Caniupán et al., (2011)

The eastern side of NPIS (fig. 7.5) was mainly restricted to “alpine-style” valley glaciers while the western side was mainly made up of large piedmont glaciers (Glasser et al., 2008). The eastern part of PIS also terminated on land, which is visible in form on terminal moraines (Glasser and Jansson, 2008). The western margin of the PIS is however more difficult to

determine due to the limited land there because the PIS most likely terminated into the fjords and open ocean along the coast (Glasser et al., 2008). Glasser et al. (2008) also suggest that the erosion had been far greater on the western side with the draining piedmont glaciers in contrast to the "alpine style" glaciers. As mentioned in the background chapter, the western side of Patagonia has a much milder and wetter climate than the cold dry climate on the eastern side, which would support more drainage and erosion (Glasser et al., 2008).

In studies by Lamy et al., (2004) and Kaiser et al., (2005), the relative concentration of Fe from X-ray fluorescence (XRF) data has been used to indicate the source rock of the sediment flux (the Andean Mountain range has high Fe content while the Coastal Range has low) where higher Fe content in offshore sediment cores indicate increased sediment flux from the Andes through glacial erosion and meltwater transport.

If the western PIS had marine termination, the IRD abundance at Site 1233 could provide some indication of marine calving rates and iceberg delivery offshore. Figure 7.6 shows the δ^{18}O record of *N. incompta* plotted versus *N. incompta*%, IRD% and the relative concentration of Fe (iron) XRF core scanning of Site 1233 (Kaiser et al., 2005)

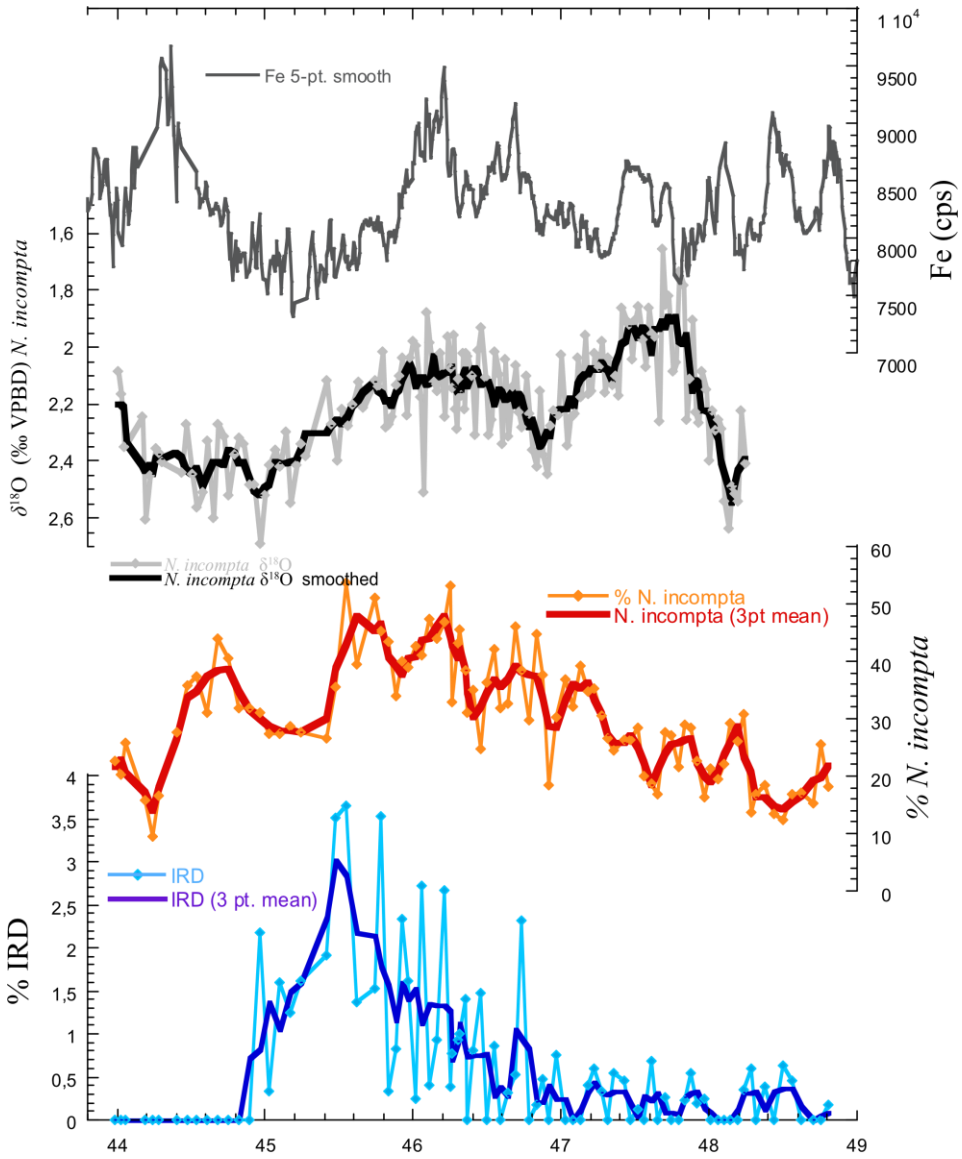

Figure 7.6 Iron (Fe)(grey) (Lamy et al., 2004; Kaiser et al; 2007) plotted together with δ^{18}O record of N. incompta (black), N. incompta% (red) and IRD % (blue)

As discussed previously, increase in *N. incompta*% may be associated with increased meltwater and/or runoff. Figure 7.6 indicates that *N. incompta*% has its highest abundance at the same time as the presence of IRD peaks. The δ^{18}O record of *N. incompta* also displays lower values coeval with peak IRD and *N. incompta*%. Consistent with increased glacial runoff and sedimentary influence, the Fe content is high during this peak—although notably Fe is also high in some intervals when IRD and *N. incompta*% are low. There is thus consistency of evidence for increased glacial meltwater and marine calving during the later phase of A2 warming. By contrast, the first peak of the A2 warming indicated by low δ^{18}O values at 47.8 Kyr BP does not show corresponding peaks in IRD and *N. incompta* %. Fe content does display increased values at 47.5 Kyr BP, slightly after the onset of the δ^{18}O

minima. Together, the records indicate that the strongest influence of icebergs and continental/glacial runoff at Site 1233 culminated during the second phase of the A2 warming, with less (partial support from Fe) or no (IRD, *N. incompta*%) indication of ice sheet and runoff signal during the first warming phase of A2.

Lamy et al. (2004) and Kaiser et al, (2005, 2007) observes a lag between Fe and SST during most of MIS 3 suggesting that ice sheet inertia may cause an offset between warming and offshore signals of ice sheet response. However, Lamy et al. (2004) suggest that the scale of this lag may be a function of ice sheet size and that a smaller PIS prior to 40 Kyr BP may have decreased the lag time. Our records show peaks of Fe (nearly) coeval with higher temperature (low $\delta^{18}O$), consistent with this shorter lag (Lamy et al., 2004). However, it is important to point out that while Fe provides a continuous record of the composition of continental sourced sedimentation, the Fe record shows peaks during both warm and cold periods suggesting that the relationship between climate, ice sheet size and dynamics, and Fe input to Site 1233 is complex. Similarly, IRD% can also be complex to interpret. Here however it provides unequivocal evidence that marine terminating glaciers calved icebergs that survived transport to Site 1233 throughout much of the study interval.

Small amounts of IRD occur prior to A2 warming, through the first phase of A2 warming, and then increase and peak during the final phase of A2 warming. The only period when no icebergs calved and were transported to Site 1233 is, paradoxically, during the cold period following the final phase of A2 warmth. Thus, the peak just prior to this interval may indicate a rapid retreat and/or surge of the PIS. If, during this phase, the margin of the PIS retreated significantly from its marine margins, this may explain why, even during a period of cool SST after 44.8 kyr BP, no IRD was deposited at Site 1233.

The coherence between offshore climate at Site 1233 and the onshore-based lithic signal in the same core, demonstrate that the PIS extent is very sensitive to offshore SST changes during glacial climate in the SE Pacific on millennial time scales. This agrees with modelling studies on PIS by Hulton et al., (2002) during the Last Glacial Maximum and the subsequent glaciation that demonstrated that their ice sheet model was most sensitive to changes in SST. Studies and observations done on the modern Patagonian Icefields and it's calving glaciers,

also document a very rapid response to an increase in regional ocean-atmosphere temperatures **(**Zemp et al., 2019; IPCC, 2019).

7.3 AAIW variability versus near surface water changes at ODP Site 1233

The planktonic foraminifera assemblages count produced in this study, and the planktonic $\delta^{18}O$ (*N. incompta and G. bulliodes*) from previous studies, document that extratropical near surface ocean properties in the SE Pacific are extremely variable on millennial-decadal timescales. Here we explore how these local surface hydrographic changes compare to local changes in bottom water properties.

The planktonic (*N. incompta*) $\delta^{18}O$ record (fig. 7.7) suggest that near surface water temperatures increased by up to about ~4.5°C over the A2 warming over a period of ~500 years (assuming temperature is the main influence on $\delta^{18}O$). The temperature increase is largest at the onset of A2 towards the peak at 47.8 Kyr BP. The second peak in the planktonic records shows a temperature increase of ~2.5°C. This twofold warming is also clearly expressed in the benthic oxygen isotopic values across the A2 event, which decrease and indicate an associated warming/freshening in AAIW. The similar timing between planktonic and benthic $\delta^{18}O$ changes indicates a close coupling between intermediate and surface water physical properties over this millennial scale event.

Subtle differences between near surface and intermediate changes do exist, however. Unlike the planktic $\delta^{18}O$ record, the benthic (*C. wuellerstorfi and U. peregrina*) $\delta^{18}O$ records (fig. 7.7) exhibit similar (temperature) changes over both peaks, displaying a ~3.6°C (both benthic records display a $\delta^{18}O$ decrease of 0.8‰) temperature increase of the intermediate waters over a period of 800-1000 years.

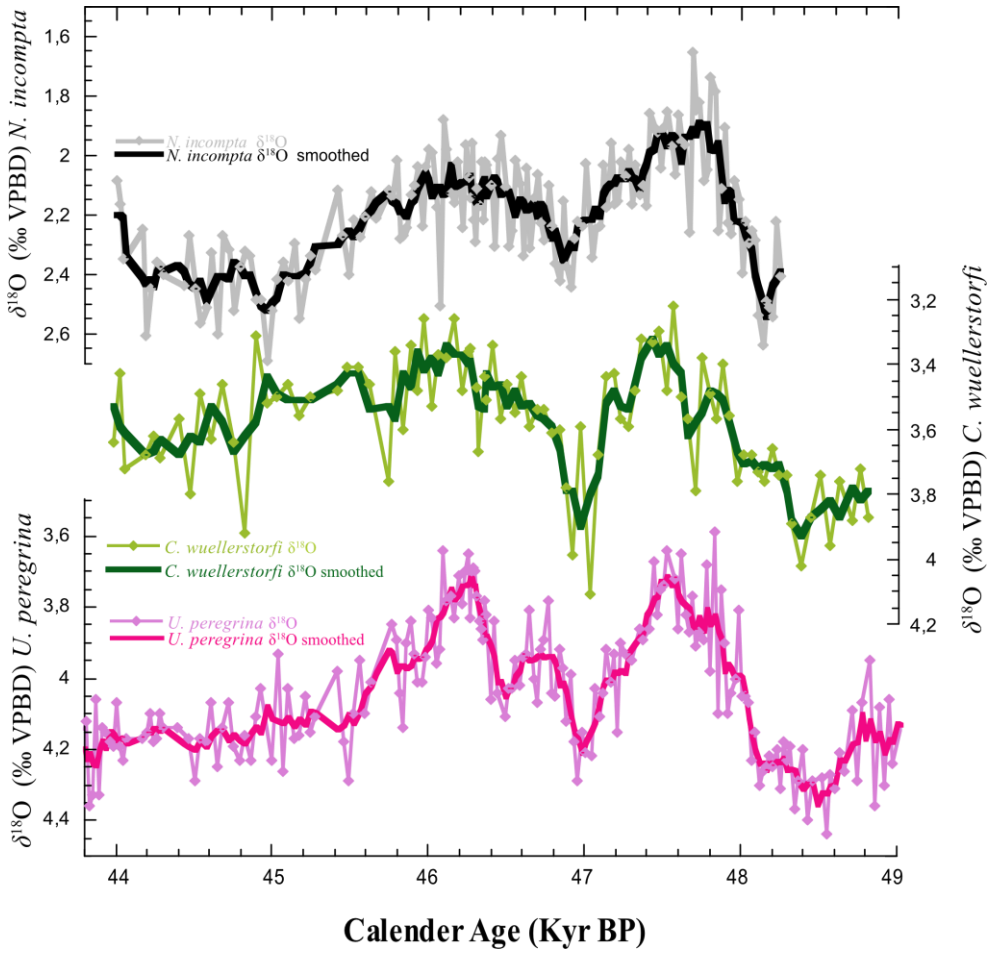

Figure 7.7: From top: The planktonic $\delta^{18}O$ record of *N. incompta* (black) plotted together with the benthic $\delta^{18}O$ records (*C. wuellerstorfi* (green) and *U. peregrina* (pink)).

The observed pattern in physical surface water properties during the A2 event at Site 1233 represents large areas in the southeast Pacific since it monitors the large scale oceanographic (ACC) and atmospheric (SWW) systems in the region. The covariance of benthic and planktonic foraminifera during the A2 event provides further evidence that these local changes are representing a much broader scale signal. AAIW, the bottom water at this location which benthic foraminifera are monitoring, is formed and subducted in the polar frontal zone (PFZ). Thus, this water mass is acquiring its properties at about 15° latitude further south and the local coherence between planktic and benthic isotope signals suggests a common influence on physical properties over a large region (41°S to approximately the PFZ/55°S). Such broad regional coherence of physical property changes in the SE Pacific has also been observed during the late Holocene (Euler and Ninnemann, 2010)

7.3.1 Mid latitude to polar coherence in the Southeast Pacific

The EDML $\delta^{18}O$ ice core signal reflects local surface air temperature over Antarctica, and it exhibits a warming during the A2 event of about ˜2°C (cf AIM12 in Antarctic temperature stack, Pedro et al., 2018). Warming over AA is (within the limitations of the age model) accompanied by warming in the formation region of AAIW (55°S) and in SE Pacific near surface waters (41°S) (fig. 7.8). All records show distinct centennial scale variability superimposed on the millennial scale warming during the A2 event. However, the split warming during the A2 that is seen in the $\delta^{18}O$ records from Site 1233 is not indicated in the Antarctic surface temperature record.

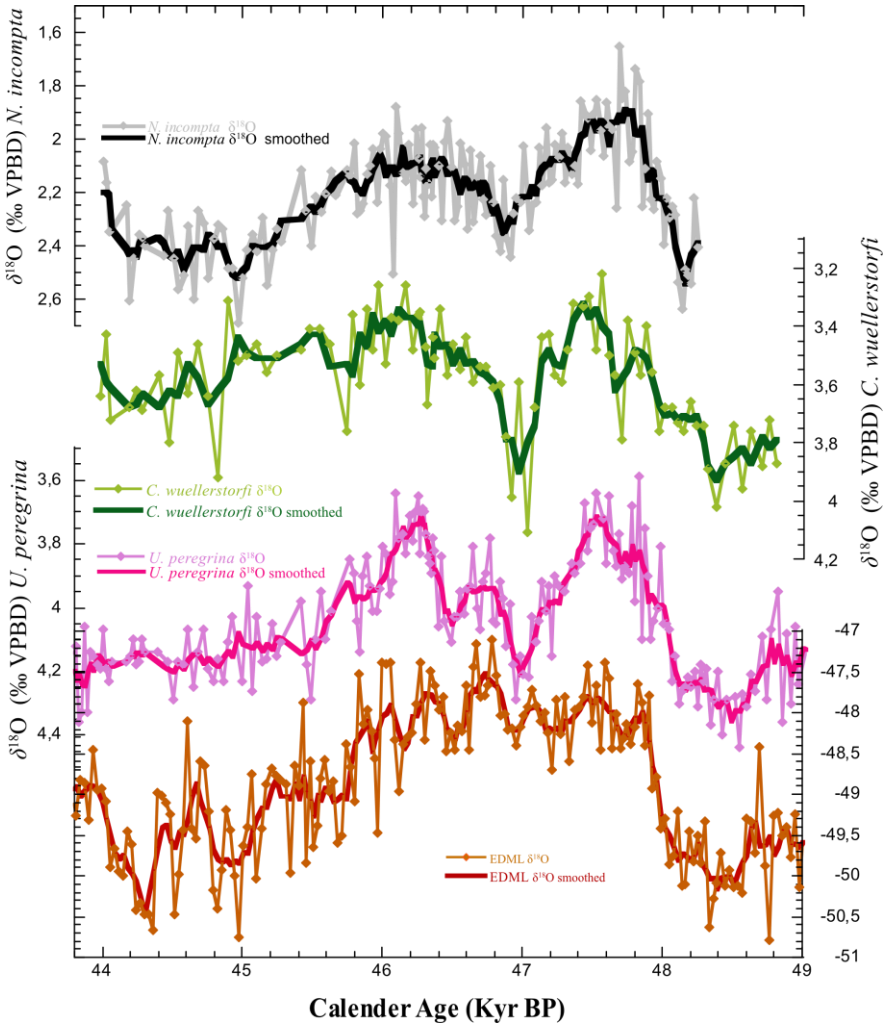

Figure 7.8: Planktonic $\delta^{18}O$ record of *N. incompta* (black) plotted together with benthic $\delta^{18}O$ record (*C. wuellerstorfi* (green) and *U. peregrina* (pink)) and the EDML $\delta^{18}O$ record (brown).

The relative timing of the centennial scale events is unconstrained with our current age model, but there is potential for fine-tuning between ODP 1233 and EDML proxies, which might align some of the centennial scale features in the foraminifera-based proxy records with those of Antarctic air temperature. The millennial scale expression of the A2 event with coeval increases in both surface temperatures at EDML and in the southeast Pacific near surface and interior, supports an active involvement of the ACC and possibly the Westerly Winds in Antarctic warming events. The extension of this climate signal also shows that AAIW is extremely sensitive and responds rapidly to climate variability in its source region over a broad spectrum of timescales.

Broader Significance of SE Pacific physical property changes.

The antiphase behavior of northern and southern ice core temperature records is most often explained as a consequence of the thermal bipolar seesaw (e.g., Crowley, 1992; Stocker and Johnsen, 2003). Southern Hemisphere warming (and northern cooling) is thought to be driven by reduced northward Atlantic heat transport as overturning circulation declines, resulting in an accumulation of heat in the Southern Hemisphere. The more muted, in both rate and magnitude, of the Antarctic temperature changes was thought to be due to the large thermal inertia of the Southern Hemisphere (i.e., the polar/deep ocean) south of the ACC which takes time and is difficult to heat (Stocker and Johnsen, 2003). In a recent study, Pedro et al., 2018 summarize model simulations of the response to reduced AMOC changes and suggest that the heat may accumulate much more rapidly in the thermocline (approximately the upper 1 km of the ocean) north of the ACC. The heat is transferred slowly across the ACC through eddies resulting in a smaller warming over Antarctica than in the subsurface thermocline of the Southern Hemisphere. Thus, the fingerprint of where, and how rapidly, this heat accumulates is critical for testing the mechanisms responsible for these interhemispheric changes. The A2 warming is associated with Heinrich Stadial 5 and reduced AMOC (Henry et al., 2016) and thus provides an opportunity to assess how and where heat accumulated in the Southern Hemisphere at this time.

The findings of this thesis are largely consistent with the general pattern of warming expected from a reduction in ocean overturning, and northward heat transport associated with reduced overturning (Pedro et al., 2018). Surface and intermediate depth warming of roughly similar magnitudes (3-4°C) suggest a broad and rapid, centennial scale, warming of the Southern Hemisphere extratropic extending south to the polar front. Thus, the Southern Hemisphere thermocline warmed and thickened during this event at roughly double the magnitude that Antarctica warmed (˜2°C; cf Antarctic temperature stack) (Fig. 2.2) It is interesting to note that such a large signal is observed in the SE Pacific thermocline suggesting that thermocline warming is propagated rapidly between the basins. Indeed, a recent study suggests that South Pacific thermocline temperature changes may be a particularly sensitive indicator for changes in northward Atlantic heat transport and AMOC variability (Sun et al., 2022) due to the inter-basinal seesaw of heat that accompanies an AMOC slowdown. Thus, our results suggest that the inter-hemispheric, and inter-basinal redistribution of heat that occurs on centennial timescales in models when AMOC is reduced, is consistent in both magnitude, and timing, with the pattern of warming observed in the SE Pacific.

Significance of Southern Hemisphere Warming for global thermocline properties

In addition to being a sensitive responder to changes in ocean circulation, AAIW has been suggested to play an important role in modulating thermocline properties over much of the global ocean (Shin et al., 2003) and could even play an active role in triggering millennial scale changes in circulation (Knorr et al., 2003). Through teleconnections in the ocean and atmosphere (here the focus is on the ocean), explained by Liu & Alexander (2007), heat is transported from one location (i.e., the poles) to another (i.e., the tropics). Thus, the intermediate ocean circulation acts as a "tunnel" through which property changes in high latitudes are transported to lower latitudes. Gu and Philander (1997) showed how intermediate and surface water in the SE Pacific could be advected through the AAIW tunnel to the tropics. Talley (1999) claims that AAIW influence intermediate and surface waters from 60°S to 20°N.

Model studies done by Liu et al. (2002) (fig.7.9) shows how an oceanic "tunnel" can transport water masses (i.e., AAIW) from the extratropics to the tropic and how these water masses can be tracked at Site 1233. The model in figure 7.9 also shows that equatorward Pacific SST is in synchrony with SH temperature. The covariance between surface and bottom dwelling isotope records confirms that extratropical surface changes are transmitted into the ocean tunnel and carried to lower latitudes just as models predict.

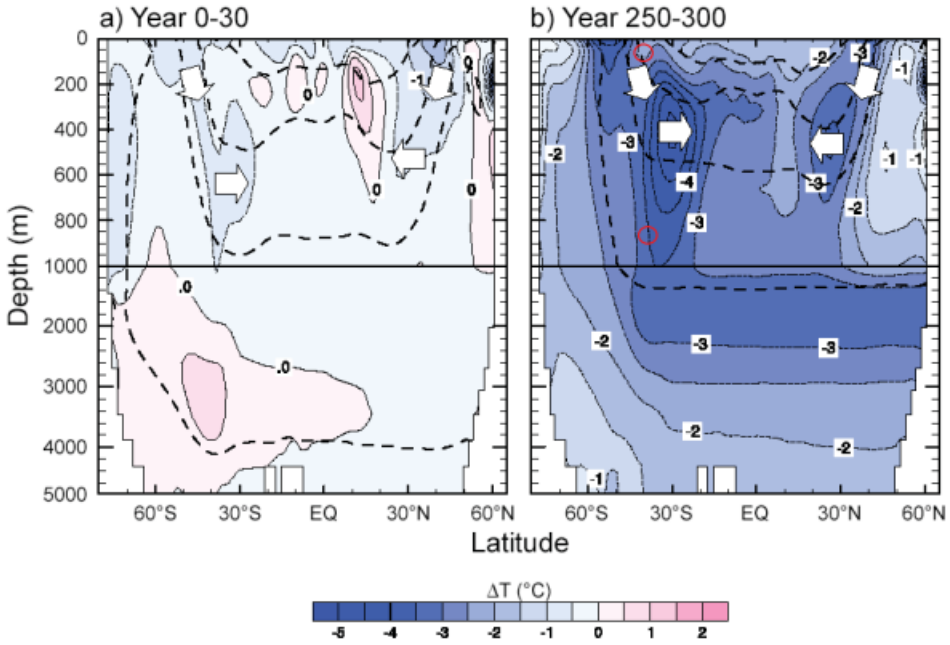

Figure 7.9: Zonally average annual mean temperature changes in the Pacific basin for (a) 0-30 years and (b) 250-300 years for modelling study of oceanic "tunnel" done by Liu et al. (2002) for the LGM. Contour interval is 1°C and negatives are dashed. The mean isotherms of 18, 10 5 and 0°C are plotted (heavy dash), coarsely representing the mean isopycnals in the ocean. The schematic arrows indicate the ventilation flow. The red circles indicate the position at which ODP Site 1233, planktic and benthic records monitor the properties of the oceanic tunnel. Shown in (a) is the cold equatorward ventilation, which can be traced to the SH extratropical surface as seen in (b). Figure modified after Liu et al. (2002).

The response and impact of intermediate water ventilation

Site 1233 is today positioned at the lower core of AAIW (838 m.b.s.l.), and its position makes it ideal to monitor vertical changes in the boundary between newly formed AAIW and the older, deeper Pacific Central Water (PCW), which underlies it. Dissolved inorganic carbon (DIC) $\delta^{13}C$ is a proxy for nutrients in the ocean and can be used to distinguish between water masses with different $\delta^{13}C$ values. Recently ventilated AAIW has a high $\delta^{13}C$ signature, while the older and nutrient rich PCW has a lower $\delta^{13}C$ signal (Eide et al., 2017). Figure 7.10 shows the $\delta^{13}C$ record of *C. wuellerstorfi* plotted versus the $\delta^{18}O$ record from EDML.

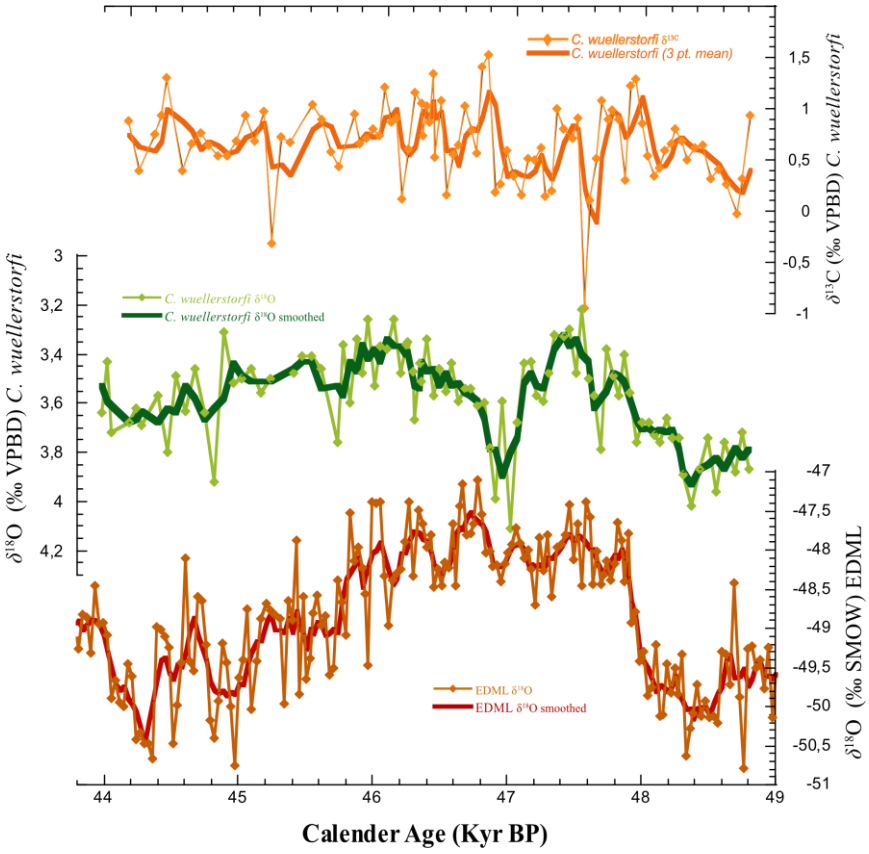

Figure 7.10: $\delta^{13}C$ record of C. wuellerstorfi (orange) plotted together with the $\delta^{18}O$ record from EDML (red). Red shading displays AAIW $\delta^{13}C$ in preindustrial ocean and the blue shading displays PCW $\delta^{13}C$ in preindustrial ocean.

During the period of Antarctic warming (high EDML $\delta^{18}O$) from 47.8 Kyr BP to 45.8 Kyr BP there are generally high $\delta^{13}C$ values, suggesting overall well-ventilated intermediate waters bathe the site. However, a distinct feature of the record are the shorter centennial scale reductions in $\delta^{13}C$ values occurring periodically during A2. The most prominent reduction in $\delta^{13}C$ occurs around 47.5 Kyr BP, near the peak in warming as indicated by the *C. wuellerstorfi* $\delta^{18}O$ record. While this is only a single point, and requires verification, it might suggest a connection between rapid warming and periods of ventilation stagnation. An alternative mechanism (to a slowdown in ventilation) to explain the lower $\delta^{13}C$, is that there was a shoaling of AAIW, and thereby an increase in PCW influence, over the site. Interestingly, a large vertical shift in the AAIW-PCW boundary has also been observed in the modern ocean (Schmidtko and Johnson, 2012) associated with warming of AAIW. Comparing $\delta^{13}C$ to $\delta^{18}O$ suggests there may be some level of coherence between high AAIW influence (high $\delta^{13}C$) and low $\delta^{18}O$ (warmer) on millennial timescales—in addition to that observed during the strong (single point) reduction. This coherence may indicate that AAIW influence was largest during the warmer periods of A2 but fluctuated significantly on centennial scales. The realization that large fluctuations in the ventilation rate, or ventilation depth of intermediate water may accompany climate changes is significant given that these intermediate waters are the source of nutrients sustaining most of the global ocean primary productivity harvestable resources (Sarmiento et al, 2011) (Moore et al., 2018)

8. Conclusion

Sedimentary samples from Ocean Drilling Program Site 1233 in the Southeast Pacific allowed millennial-centennial resolved proxy records over Antarctic warming event A2, documenting the magnitude of surface water variability and expression of Antarctic Intermediate Water (AAIW) variability in unprecedented detail.

Foraminiferal assemblage counts assess the productivity and water mass properties of the surface ocean and demonstrate that the extratropical near surface ocean properties are extremely variable on millennial-centennial timescales.

Ice-rafted detritus (IRD) counts assess the variability of the Patagonian Ice Sheet, and the IRD peaks that spans most of warming event A2, reflects calving from the northernmost part of the marine terminating Patagonian ice sheet, and is closely coupled to offshore climate.

The benthic foraminiferal oxygen isotopic record monitors the physical properties of AAIW close to its source in the Southeast Pacific, while the planktonic isotopic record monitors the near surface water properties and the large scale atmospheric (Southern Westerlies) and oceanic (Antarctic Circumpolar Current) systems influencing them. Taken together, these records provide a simultaneous sub-millennial scale description of Southeast Pacific surface and intermediate water properties over A2.

The close coupling of near surface water and intermediate water $\delta^{18}O$ in this study, together imply that changes in the foraminiferal $\delta^{18}O$ are driven by temperature. Model studies have suggested that the extratropic could play an important role in modulating tropical climate, ocean circulation, and even the global ice volume and sea-level. The close coupling between AAIW properties and the EPICA Dronning Maud Land air temperature record in this study, demonstrates that the observed changes in Antarctic climate are transmitted through the mouth of the oceanic tunnel and along the base of the thermocline (AAIW).

Bibliography

Ackert Jr, R. P., Becker, R. A., Singer, B. S., Kurz, M. D., Caffee, M. W., & Mickelson, D. M. (2008). Patagonian glacier response during the late glacial– holocene transition. *Science*, *321*(5887), 392–395.

Aguirre, C., Garcıa-Loyola, S., Testa, G., Silva, D., Farıas, L., & Tremblay, J.-E.´ (2018). Insight into anthropogenic forcing on coastal upwelling off southcentral chile. *Elementa: Science of the Anthropocene*, *6*.

Alheit, J., & Bernal, P. (1993). Effects of physical and biological changes on the biomass yield of the Humboldt Current ecosystem. In K. Sherman, L. M. Alexander, & B. D. Gold (Eds.), Large marine ecosystems – Stress, mitigation and sustainability (pp. 53–68). Washington: American Association for the Advancement of Science.

Andersen, K. K., Svensson, A., Johnsen, S. J., Rasmussen, S. O., Bigler, M., R¨othlisberger, R., Ruth, U., Siggaard-Andersen, M.-L., Steffensen, J. P., Dahl-Jensen, D., et al. (2006). The greenland ice core chronology 2005, 15–42 ka. part 1: Constructing the time scale. *Quaternary Science Reviews*, *25*(23-24), 3246–3257.

Anderson, R., Ali, S., Bradtmiller, L., Nielsen, S., Fleisher, M., Anderson, B., & Burckle, L. (2009). Wind-driven upwelling in the southern ocean and the deglacial rise in atmospheric co2. *science*, *323*(5920), 1443–1448.

Bandy, O. L. (1960). The geologic significance of coiling ratios in the foraminifer globigerina pachyderma (ehrenberg)[california]. *Journal of Paleontology*, *34*(4), 671–681.

Bard, E., & Rickaby, R. E. (2009). Migration of the subtropical front as a modulator of glacial climate. *Nature*, *460*(7253), 380–383.

Bauch, D., Carstens, J., & Wefer, G. (1997). Oxygen isotope composition of living neogloboquadrina pachyderma (sin.) in the arctic ocean. *Earth and Planetary Science Letters*, *146*(1-2), 47–58.

Bauch, D., Darling, K., Simstich, J., Bauch, H. A., Erlenkeuser, H., & Kroon, D. (2003). Palaeoceanographic implications of genetic variation in living north atlantic neogloboquadrina pachyderma. *Nature*, *424*(6946), 299–302.

Be, A. W. H. (1960). Ecology of recent planktonic foraminifera–part 2, bathymetric and seasonal distributions in the sargasso sea off nermuda. *Micropaleontology*, *6*(4), 373–392.

B´e, A. W., & Hutson, W. H. (1977). Ecology of planktonic foraminifera and biogeographic patterns of life and fossil assemblages in the indian ocean. *Micropaleontology*, 369–414.

Beers, J. M., & Jayasundara, N. (2015). Antarctic notothenioid fish: What are the future consequences of 'losses' and 'gains' acquired during long-term evolution at cold and stable temperatures? *The Journal of experimental biology*, *218*(12), 1834–1845.

Bergami, C., Capotondi, L., Langone, L., Giglio, F., & Ravaioli, M. (2009). Distribution of living planktonic foraminifera in the ross sea and the pacific sector of the southern ocean (antarctica). *Marine Micropaleontology*, *73*(1-2), 37–48.

Berger, W., Smetacek, V., Wefer, G., et al. (1989). Ocean productivity and paleoproductivity—an overview. *Productivity of the ocean: present and past*, *44*, 1–34.

Berger, W., Vincent, E., & Thierstein, H. (1981). The deep-sea record: Major steps in cenozoic ocean evolution.

Blanco, J. L., Carr, M.-E., Thomas, A. C., & Strub, P. T. (2002). Hydrographic conditions off northern chile during the 1996–1998 la nina and el nino events. *Journal of Geophysical Research: Oceans*, *107*(C3), 3–1.

Blunier, T., & Brook, E. J. (2001). Timing of millennial-scale climate change in antarctica and greenland during the last glacial period. *science*, *291*(5501), 109–112.

Blunier, T., Spahni, R., Barnola, J.-M., Chappellaz, J., Loulergue, L., & Schwander, J. (2007). Synchronization of ice core records via atmospheric gases. Climate of the past, 3 (2), 325–330.

Boex, J., Fogwill, C., Harrison, S., Glasser, N., Hein, A., Schnabel, C., & Xu, S. (2013). Rapid thinning of the late pleistocene patagonian ice sheet followed migration of the southern westerlies. *Scientific Reports*, *3*(1), 1–6.

Boltovskoy, E. (1973). Note on the determination of absolute surface water paleotemperature by means of the foraminiferglobigerina bulloides d'orbigny. *Pal¨aontologische Zeitschrift*, *47*(3), 152–155.

Bond, G., Broecker, W., Johnsen, S., McManus, J., Labeyrie, L., Jouzel, J., & Bonani, G. (1993). Correlations between climate records from north atlantic sediments and greenland ice. *Nature*, *365*(6442), 143–147.

Bond, G., Heinrich, H., Broecker, W., Labeyrie, L., McManus, J., Andrews, J., Huon, S., Jantschik, R., Clasen, S., Simet, C., et al. (1992). Evidence for massive discharges of

icebergs into the north atlantic ocean during the last glacial period. *Nature*, *360*(6401), 245–249.

Bond, G., Showers, W., Cheseby, M., Lotti, R., Almasi, P., DeMenocal, P., Priore, P., Cullen, H., Hajdas, I., & Bonani, G. (1997). A pervasive millennial-scale cycle in north atlantic holocene and glacial climates. *science*, *278*(5341), 1257– 1266.

BouDagher-Fadel, M. K. (K. (2015). Biostratigraphic and geological significance of planktonic foraminifera (Updated second edition.).

Boyer, Tim P.; García, Hernán E.; Locarnini, Ricardo A.; Zweng, Melissa M.; Mishonov, Alexey V.; Reagan, James R.; Weathers, Katharine A.; Baranova, Olga K.; Paver, Christopher R.; Seidov, Dan; Smolyar, Igor V. (2018). World Ocean Atlas 2018. [indicate subset used]. NOAA National Centers for Environmental Information. Dataset. https://www.ncei.noaa.gov/archive/accession/NCEI-WOA18. Accessed [date]

Bravo, C., Bozkurt, D., Ross, A. N., & Quincey, D. J. (2021). Projected increases in surface melt and ice loss for the northern and southern patagonian icefields. *Scientific Reports*, *11*(1), 1–13.

Broecker, W. S. (1994). Massive iceberg discharges as triggers for global climate change. *Nature*, *372*(6505), 421–424.

Broecker, W. S. (1998). Paleocean circulation during the last deglaciation: A bipolar seesaw? *Paleoceanography*, *13*(2), 119–121.

Brummer, G.-J. A., & Kroon, D. (1998). Genetically controlled planktonic foraminif -eral coiling ratios as tracers of past ocean dynamics. In G.-J. A. Brummer & D. Kroon (Eds.), *Planktonic foraminifers as tracers of ocean-climate history* (pp. 293–298). Free Univ. Press, Amsterdam.

Caniupan, M., Lamy, F., Lange, C., Kaiser, J., Arz, H., Kilian, R., Baeza Urrea, O., Aracena, C., Hebbeln, D., Kissel, C., et al. (2011). Millennial-scale sea surface temperature and patagonian ice sheet changes off southernmost chile (53 s) over the past 60 kyr. *Paleoceanography*, *26*(3).

Carrivick, J. L., Davies, B. J., James, W. H., Quincey, D. J., & Glasser, N. F. (2016). Distributed ice thickness and glacier volume in southern south america. *Global and Planetary Change*, *146*, 122–132.

Carstens, J., Hebbeln, D., & Wefer, G. (1997). Distribution of planktic foraminifera at the ice margin in the arctic (fram strait). *Marine Micropaleontology*, *29*(34), 257–269.

Cayre, O., Beaufort, L., & Vincent, E. (1999). Paleoproductivity in the equatorial indian ocean for the last 260,000 yr: A transfer function based on planktonic foraminifera. *Quaternary Science Reviews*, *18*(6), 839–857.

Charles, C. D., Wright, J. D., & Fairbanks, R. G. (1993). Thermodynamic influences on the marine carbon isotope record. *Paleoceanography*, *8*(6), 691–697.

Clark, I., & Fritz, P. (1997). *Environmental isotopes in hydrogeology*. https://doi.org/10.1201/9781482242911

Clark, P. U., Pisias, N. G., Stocker, T. F., & Weaver, A. J. (2002). The role of the thermohaline circulation in abrupt climate change. *Nature*, *415*(6874), 863– 869.

Cooke, S., & Rohling, E. J. (2001). *Stable isotopes in foraminiferal carbonate*. Southampton Oceanography Centre.

Curry, W. B., Duplessy, J.-C., Labeyrie, L., & Shackleton, N. J. (1988). Changes in the distribution of δ13c of deep water Σco2 between the last glaciation and the holocene. *Paleoceanography*, *3*(3), 317–341.

Damm-Johnsen, T. (2019). *Centennial scale variability in southeast pacific hydrography and its link to the bipolar seesaw and ice sheet dynamics.* (Master's thesis). Department of earth science University of Bergen.

Dansgaard, W., Johnsen, S., Clausen, H., Dahl-Jensen, D., Gundestrup, N., Hammer, C., & Oeschger, H. (1984). North atlantic climatic oscillations revealed by deep greenland ice cores. *Climate processes and climate sensitivity*, *29*, 288–298.

Darling, K. F., Kucera, M., Kroon, D., & Wade, C. M. (2006). A resolution for the coiling direction paradox in neogloboquadrina pachyderma. *Paleoceanography*, *21*(2).

Darling, K. F., Kucera, M., Pudsey, C. J., & Wade, C. M. (2004). Molecular evidence links cryptic diversification in polar planktonic protists to quaternary climate dynamics. *Proceedings of the National Academy of Sciences*, *101*(20), 7657– 7662.

Darling, K. F., Wade, C. M., Siccha, M., Trommer, G., Schulz, H., Abdolalipour, S., & Kurasawa, A. (2017). Genetic diversity and ecology of the planktonic foraminifers globigerina bulloides, turborotalita quinqueloba and neogloboquadrina pachyderma off the oman margin during the late sw monsoon. *Marine Micropaleontology*, *137*, 64–77.

Darling, K. F., Wade, C. M., Stewart, I. A., Kroon, D., Dingle, R., & Brown, A. J. L. (2000). Molecular evidence for genetic mixing of arctic and antarctic subpolar populations of planktonic foraminifers. *Nature*, *405*(6782), 43–47.

Darvill, C. M., Bentley, M. J., Stokes, C. R., Hein, A. S., & Rod´es, A. (2015). ´ Extensive mis 3 glaciation in southernmost patagonia revealed by cosmogenic nuclide dating of outwash sediments. *Earth and Planetary Science Letters*, *429*, 157–169.

Davies, B. J., Darvill, C. M., Lovell, H., Bendle, J. M., Dowdeswell, J. A., Fabel, D., Garcıa, J.-L., Geiger, A., Glasser, N. F., Gheorghiu, D. M., et al. (2020). The evolution of the patagonian ice sheet from 35 ka to the present day (patice). *Earth-Science Reviews*, *204*, 103152.

Davies, B., & Glasser, N. (2012). Accelerating shrinkage of patagonian glaciers from the little ice age (˜ad 1870) to 2011. *Journal of Glaciology*, *58*(212), 1063– 1084.

De Deckker, P., Moros, M., Perner, K., & Jansen, E. (2012). Influence of the tropics and southern westerlies on glacial interhemispheric asymmetry. *Nature Geoscience*, *5*(4), 266–269.

Denton, G. H., Lowell, T., Heusser, C., Schlu¨chter, C., Andersen, B. G., Heusser, L. E., Moreno, P. I., & Marchant, D. R. (1999). Geomorphology, stratigraphy, and radiocarbon chronology of llanquihuedrift in the area of the southern lake district, seno reloncavı, and isla grande de chilo´e, chile. *Geografiska Annaler: Series A, Physical Geography*, *81*(2), 167–229.

Deuser, W., Ross, E., Hemleben, C., & Spindler, M. (1981). Seasonal changes in species composition, numbers, mass, size, and isotopic composition of planktonic foraminifera settling into the deep sargasso sea. *Palaeogeography, Palaeoclimatology, Palaeoecology*, *33*(1-3), 103–127.

Dieckmann, G., Spindler, M., Lange, M. A., Ackley, S. F., & Eicken, H. (1991). Antarctic sea ice: A habitat for the foraminifer neogloboquadrina pachyderma. *Journal of Foraminiferal Research*, *21*(2), 182–189.

Doe, B. R. (1983). The past is the key to the future. *Geochimicaet CosmochimicaActa*, *47*(8), 1341–1354. https://doi.org/https://doi.org/10.1016/00167037(83)90293-4

Dowdeswell, J., Canals, M., Jakobsson, M., Todd, B., Dowdeswell, E., & Hogan, K. (2016). The variety and distribution of submarine glacial landforms and implications for ice-sheet reconstruction. *Geological Society, London, Memoirs*, *46*(1), 519–552.

Eide, M., Olsen, A., Ninnemann, U. S., & Johannessen, T. (2017). A global ocean climatology of preindustrial and modern ocean δ13c. *Global Biogeochemical Cycles*, *31*(3), 515–534.

Ekman, V. W. (1905). On the influence of the earth's rotation on ocean-currents.

Epstein, S., Buchsbaum, R., Lowenstam, H. A., & Urey, H. C. (1953). Revised carbonate-water isotopic temperature scale. *Geological Society of America Bulletin*, *64*(11), 1315–1326.

Ericson, D. B. (1959). Coiling direction of globigerina pachyderma as a climatic index. *Science*, *130*(3369), 219–220.

Ericson, D. B., Wollin, G., & Wollin, J. (1955). Coiling direction of globorotalia truncatulinoides in deep-sea cores. *Deep Sea Research (1953)*, *2*(2), 152–158.

Euler, C. (2010). *Natural decadal to centennial scale variability of southeast pacific water mass properties. multiproxy reconstructions under different climatic boundary conditions in the late quaternary.* (Doctoral dissertation). Department of Earth Science, University of Bergen.

Euler, C., & Ninnemann, U. S. (2010). Climate and Antarctic Intermediate Water coupling during the late Holocene. *Geology*, *38*(7), 647–650. https://doi.org/ 10.1130/G30902.1

Fairbanks, R. G., Sverdlove, M., Free, R., Wiebe, P. H., & B´e, A. W. (1982). Vertical distribution and isotopic fractionation of living planktonic foraminifera from the panama basin. *Nature*, *298*(5877), 841–844.

Fairbanks, R. G., Wiebe, P. H., & B´e, A. W. (1980). Vertical distribution and isotopic composition of living planktonic foraminifera in the western north atlantic. *Science*, *207*(4426), 61–63.

Faure, G., & Mensing, T. M. (2005). *Principles and applications*. John Wiley & Sons, Inc.

Ferrari, R., Jansen, M. F., Adkins, J. F., Burke, A., Stewart, A. L., & Thompson, A. F. (2014). Antarctic sea ice control on ocean circulation in present and glacial climates. *Proceedings of the National Academy of Sciences*, *111*(24), 8753–8758.

Field, D. B. (2004) Variability in vertical distributions of planktonic foraminifera in the California Current: Relationship to vertical ocean structure, Paleoceanography, vol. 19, PA2014, pp. 1-22,

Fontanier, C., Mackensen, A., Jorissen, F. J., Anschutz, P., Licari, L., & Griveaud, C. (2006). Stable oxygen and carbon isotopes of live benthic foraminifera from the bay of biscay: Microhabitat impact and seasonal variability. *Marine Micropaleontology*, *58*(3), 159–183.

Førde, A. E. (2008). *Millennial to sub-millennial scale variability in sub antarctic near surface and intermediate water properties across the antarctic warming event 1 and the*

laschamp geomagnetic excursion at odp site 1233 (Master's thesis). Department of earth science University of Bergen.

Galli-Olivier, C. (1967). Pediplain in northern chile and the andean uplift. *Science*, *158*(3801), 653–655.

Garcıa, J.-L., Hein, A. S., Binnie, S. A., G´omez, G. A., Gonza´lez, M. A., & Dunai, T. J. (2018). The mis 3 maximum of the torres del paine and u´ltima esperanza ice lobes in patagonia and the pacing of southern mountain glaciation. *Quaternary Science Reviews*, *185*, 9–26.

Gersonde, R., & Zielinski, U. (2000). The reconstruction of late quaternary antarctic sea-ice distribution—the use of diatoms as a proxy for sea-ice. *Palaeogeography, Palaeoclimatology, Palaeoecology*, *162*(3-4), 263–286.

Glasser, N., & Jansson, K. (2008). The glacial map of southern south america. *Journal of Maps*, *4*(1), 175–196. https://doi.org/10.4113/jom.2008.1020

Glasser, N. F., Jansson, K. N., Goodfellow, B. W., de Angelis, H., Rodnight, H., & Rood, D. H. (2011). Cosmogenic nuclide exposure ages for moraines in the lago san martin valley, argentina. *Quaternary Research*, *75*(3), 636–646.

Graham, D. W., Corliss, B. H., Bender, M. L., & Keigwin Jr, L. D. (1981). Carbon and oxygen isotopic disequilibria of recent deep-sea benthic foraminifera. *Marine micropaleontology*, *6*(5-6), 483–497.

Greco, M., Jonkers, L., Kretschmer, K., Bijma, J., & Kucera, M. (2019). Depth habitat of the planktonic foraminifera neogloboquadrina pachyderma in the northern high latitudes explained by sea-ice and chlorophyll concentrations. *Biogeosciences*, *16*(17), 3425–3437.

Grootes, P. M., Steig, E. J., Stuiver, M., Waddington, E. D., Morse, D. L., & Nadeau, M.-J. (2001). The taylor dome antarctic 18o record and globally synchronous changes in climate. *Quaternary Research*, *56*(3), 289–298.

Grossman, E. L. (1987). Stable isotopes in modern benthic foraminifera; a study of vital effect. *The Journal of Foraminiferal Research*, *17*(1), 48–61.

Gu, D., and S. G. H. Philander, Interdecadal climate fluctuations that depend on exchanges between the tropics and extratropics, Science, 275, 805-807, 1997.

Hansen, J. E., & Sato, M. (2012). Paleoclimate implications for human-made climate change. *Climate change* (pp. 21–47). Springer.

Haynes, J. R. (1981). The agglutinating foraminifera. *Foraminifera* (pp. 81–116). Springer.

Hays, J. D., Imbrie, J., & Shackleton, N. J. (1976). Variations in the earth's orbit: Pacemaker of the ice ages: For 500,000 years, major climatic changes have followed variations in obliquity and precession. *science*, *194*(4270), 1121– 1132.

Hebbeln, D., Marchant, M., Freudenthal, T., & Wefer, G. (2000). Surface sediment distribution along the chilean continental slope related to upwelling and productivity. *Marine Geology*, *164*(3-4), 119–137.

Hebbeln, D., Marchant, M., & Wefer, G. (2000). Seasonal variations of the particle flux in the peru-chile current at 30 s under 'normal'and el nin˜o conditions. *Deep Sea Research Part II: Topical Studies in Oceanography*, *47*(9-11), 2101– 2128.

Heinrich, H. (1988) Origin and consequences of cyclic ice rafting in the northeast Atlantic Ocean during the past 130000 years. Quat Res 29:143-152

Heusser, C. J. (2003) Ice age southern Andes: a chronicle of palaeoecological events, Elsevier, Tuxedo, US.

Heusser, L., Heusser, C., Mix, A., & McManus, J. (2006). Chilean and southeast pacific paleoclimate variations during the last glacial cycle: Directly correlated pollen and d18o records from odp site 1234. *Quaternary Science Reviews*, *25*(23-24), 3404–3415.

Heusser, L., Heusser, C., & Pisias, N. (2006). Vegetation and climate dynamics of southern chile during the past 50,000 years: Results of odp site 1233 pollen analysis. *Quaternary Science Reviews*, *25*(5-6), 474–485.

NGRIP members, (2004) High-resolution record of northern hemisphere climate extending into the last interglacial period. *Nature*, *431*(7005), 147–151.

Hulton, N. R., Purves, R., McCulloch, R., Sugden, D. E., & Bentley, M. J. (2002). The last glacial maximum and deglaciation in southern south america. *Quaternary Science Reviews*, *21*(1-3), 233–241.

Ivanova, E. M., Conan, S. M.-H., Peeters, F. J., & Troelstra, S. R. (1999). Living neogloboquadrina pachyderma sin and its distribution in the sediments from oman and somalia upwelling areas. *Marine Micropaleontology*, *36*(2-3), 91– 107.

Johannessen, T., Jansen, E., Flatøy, A., & Ravelo, A. C. (1994). The relationship between surface water masses, oceanographic fronts and paleoclimatic proxies in surface sediments of the greenland, iceland, norwegian seas. *Carbon cycling in the glacial ocean: Constraints on the ocean's role in global change* (pp. 61– 85). Springer.

Johnsen, S. J., Dansgaard, W., Clausen, H., & Langway, C. (1972). Oxygen isotope profiles through the antarctic and greenland ice sheets. *Nature*, *235*(5339), 429–434.

Jonkers, L., Brummer, G.-J. A., Peeters, F. J., van Aken, H. M., & De Jong, M. F. (2010). Seasonal stratification, shell flux, and oxygen isotope dynamics of left-coiling n. pachyderma and t. quinqueloba in the western subpolar north atlantic. *Paleoceanography*, *25*(2).

Jouzel, J., Lorius, C., Petit, J.-R., Genthon, C., Barkov, N. I., Kotlyakov, V. M., & Petrov, V. M. (1987). Vostok ice core: A continuous isotope temperature record over the last climatic cycle (160,000 years). *nature*, *329*(6138), 403– 408.

Kaplan, M., et al. (2008) Southern Patagonian glacial chronology for the Last Glacial period and implications for Southern Ocean climate. Quaternary Science Reviews, 27 (3-4), p. 284-294.

Kaiser, J., Lamy, F., Arz, H. W., & Hebbeln, D. (2007). Dynamics of the millennialscale sea surface temperature and patagonian ice sheet fluctuations in southern chile during the last 70 kyr (odp site 1233). *Quaternary International*, *161*(1), 77–89.

Kaiser, J., Lamy, F., & Hebbeln, D. (2005). A 70-kyr sea surface temperature record off southern chile (ocean drilling program site 1233). *Paleoceanography*, *20*(4).

Kaiser, J., & Lamy, F. (2010). Links between patagonian ice sheet fluctuations and antarctic dust variability during the last glacial period (mis 4-2). *Quaternary Science Reviews*, *29*(11-12), 1464–1471.

Keigwin, L. D., & Lehman, S. J. (1994). Deep circulation change linked to heinrich event 1 and younger dryas in a middepth north atlantic core. *Paleoceanography*, *9*(2), 185–194.

Kleiven, H. F., Jansen, E., Fronval, T., & Smith, T. (2002). Intensification of northern hemisphere glaciations in the circum atlantic region (3.5–2.4 ma)–icerafted detritus evidence. *Palaeogeography, Palaeoclimatology, Palaeoecology*, *184*(3-4), 213–223.

Kleiven, H. F., Jansen, E., Curry, W. B., Hodell, D. A., & Venz, K. (2003). Atlantic ocean thermohaline circulation changes on orbital to suborbital timescales during the mid-pleistocene Paleoceanog-raphy, 18, 1008, doi:10.1029/2001PA000629, 1.). Paleoceanography, 18 (1), 1008–n/a.

Knorr, G., and Lohmann, G. (2003) Southern Ocean origin for the resumption of Atlantic thermohaline circulation during deglaciation, Nature, 424, 532– 536.

Kohfeld, K. E., Fairbanks, R. G., Smith, S. L., & Walsh, I. D. (1996). Neogloboquadrina pachyderma (sinistral coiling) as paleoceanographic tracers in polar oceans: Evidence

from northeast water polynya plankton tows, sediment traps, and surface sediments. *Paleoceanography*, *11*(6), 679–699.

Kucera, M. (2007). Chapter six planktonic foraminifera as tracers of past oceanic environments. *Developments in marine geology*, *1*, 213–262.

Kucera, M., Weinelt, M., Kiefer, T., Pflaumann, U., Hayes, A., Weinelt, M., Chen, M.-T., Mix, A. C., Barrows, T. T., Cortijo, E., et al. (2005a). Reconstruction of sea-surface temperatures from assemblages of planktonic foraminifera: Multi-technique approach based on geographically constrained calibration

data sets and its application to glacial atlantic and pacific oceans. *Quaternary Science Reviews*, *24*(7-9), 951–998.

Kucera, M., Weinelt, M., Kiefer, T., Pflaumann, U., Hayes, A., Weinelt, M., Chen, M.-T., Mix, A. C., Barrows, T. T., Cortijo, E., Duprat, J. M., Juggins, S., & Waelbroeck, C. (2005b). Compilation of planktic foraminifera census data, modern from the Pacific Ocean [In supplement to: Kucera, M et al. (2005): Reconstruction of sea-surface temperatures from assemblages of planktonic foraminifera: multi-technique approach based on geographically constrained calibration datasets and its application to glacial Atlantic and Pacific Oceans.

Quaternary Science Reviews, 24(7-9),

951-998, https://doi.org/10.1016/j.quascirev.2004.07.014

PANGAEA. https://doi.org/10.1594/PANGAEA.227323

Kuhlbrodt, T., Griesel, A., Montoya, M., Levermann, A., Hofmann, M., & Rahmstorf, S. (2007). On the driving processes of the atlantic meridional overturning circulation. *Reviews of Geophysics*, *45*(2).

Lamy, F., et al. (2001) Holocene rainfall variability in southern Chile: a marine record of latitudinal shifts of the Southern Westerlies. Earth and Planetary Science Letters, 185 (3), p. 369-382.

Lamy, F., Kaiser, J., Arz, H. W., Hebbeln, D., Ninnemann, U., Timm, O., Timmermann, A., & Toggweiler, J. R. (2007). Modulation of the bipolar seesaw in the southeast pacific during termination 1. *Earth and Planetary Science Letters*, *259*(3-4), 400–413.

Lamy, F., Kaiser, J., Ninnemann, U., Hebbeln, D., Arz, H. W., & Stoner, J. (2004). Antarctic timing of surface water changes off chile and patagonian ice sheet response. *Science*, *304*(5679), 1959–1962.

Levitus, S., & Boyer, T. P. (1994). *World ocean atlas 1994. volume 4. temperature* (tech. rep.). National Environmental Satellite, Data, and Information Service, Washington ...

Libby, W. F. (1961). Radiocarbon dating: The method is of increasing use to the archeologist, the geologist, the meteorologist, and the oceanographer. *Science*, *133*(3453), 621–629.

Liu, Z., Shin, S., Otto-Bliesner, B., Kutzbach, J. E, Brady, E. C., and Lee, D. (2002) Tropical cooling at the Last Glacial Maximum and extratropical ocean ventilation, Geophys. Res. Lett, 29,

Liu, Z., & Alexander, M. (2007). Atmospheric bridge, oceanic tunnel, and global climatic teleconnections. *Reviews of Geophysics*, *45*(2).

Liu, Z., & Yang, H. (2003). Extratropical control of tropical climate, the atmospheric bridge and oceanic tunnel. *Geophysical Research Letters*, *30*(5).

Lund, S. P., Stoner, J., & Lamy, F. (2007). Late quaternary paleomagnetic secular variation and chronostratigraphy from odp sites 1233 and 1234. *Proceedings of the Ocean Drilling Program: Scientific Results*, *202*.

Lwasa, S., Seto, K., Bai, X., Blanco, H., Gurney, K., Kilki¸s, S., Lucon, O., Murakami, J., Pan, J., Sharifi, A., & Yamagata, Y. (2022). Urban systems and other settlements Supplementary Material. In P. Shukla, J. Skea, R. Slade, A. A. Khourdajie, R. van Diemen, D. McCollum, M. Pathak, S. Some, P. Vyas, R. Fradera, M. Belkacemi, A. Hasija, G. Lisboa, S. Luz, & J. Malley (Eds.), *Ipcc, 2022: Climate change 2022: Mitigation of climate change. contribution of working group iii to the sixth assessment report of the intergovernmental panel on climate change*. Cambridge University Press.

Manabe, S., & Stouffer, R. J. (1997). Coupled ocean-atmosphere model response to freshwater input: Comparison to younger dryas event. *Paleoceanography*, *12*(2), 321–336.

Marchant, M., Hebbeln, D., Giglio, S., Coloma, C., & Gonza´lez, H. E. (2004). Seasonal and interannual variability in the flux of planktic foraminifera in the humboldt current system off central chile (30 s). *Deep Sea Research Part II: Topical Studies in Oceanography*, *51*(20-21), 2441–2455.

Marchant, M., Hebbeln, D., & Wefer, G. (1998). Seasonal flux patterns of planktic foraminifera in the peru–chile current. *Deep Sea Research Part I: Oceanographic Research Papers*, *45*(7), 1161–1185.

Markgraf, V., Dodson, J. R., Kershaw, A. P., McGlone, M. S., & Nicholls, N. (1992). Evolution of late pleistocene and holocene climates in the circum-south pacific land areas. *Climate Dynamics*, *6*(3), 193–211.

Martinez, P., Lamy, F., Robinson, R. R., Pichevin, L., & Billy, I. (2006). Atypical δ15n variations at the southern boundary of the east pacific oxygen minimum zone over the last 50 ka. *Quaternary Science Reviews*, *25*(21-22), 3017–3028.

McCrea, J. M. (1950). On the isotopic chemistry of carbonates and a paleotemperature scale. *The Journal of Chemical Physics*, *18*(6), 849–857.

McManus, J. F., Bond, G. C., Broecker, W. S., Johnsen, S., Labeyrie, L., & Higgins, S. (1994). High-resolution climate records from the north atlantic during the last interglacial. *Nature*, *371*(6495), 326–329.

McManus, J. F., Oppo, D. W., & Cullen, J. L. (1999). A 0.5-million-year record of millennial-scale climate variability in the north atlantic. *science*, *283*(5404), 971–975.

Members, C. P. (1976). The surface of the ice-age earth. Science (American Association for the Advancement of Science), 191 (4232), 1131–1137.

Members, C. P., Ruddiman, W. F., Cline, R. M. L., Hays, J. D., Prell, W. L., Moore, T. C., Kipp, N. G., Molfino, B. E., Denton, G. H., Hughes, T. J., et al. (1984). The last interglacial ocean. *Quaternary Research*, *21*(2), 123–224.

Members, W. D. P. et al. (2015). Precise interpolar phasing of abrupt climate change during the last ice age. *Nature*, *520*(7549), 661–665.

Michael, S. (1996). On the salinity tolerance of the planktonic foraminifer neogloboquadrina pachyderma from antarctic sea ice (17th symposium on polar biology). *Proceedings of the NIPR Symposium on Polar Biology*, (9), 85–91.

Milankovitch, M. (1941). Kanon der erdbestrahlung und seine anwendung auf das eiszeitenproblem. *Royal Serbian Academy Special Publication*, *133*, 1–633.

Mix, A. C., Morey, A. E., Pisias, N. G., & Hostetler, S. W. (1999). Foraminiferal faunal estimates of paleotemperature: Circumventing the no-analog problem yields cool ice age tropics. *Paleoceanography*, *14*(3), 350–359.

Mohtadi, M. & Hebbeln, D. (2004) Mechanisms and variations of the paleoproductivity off northern Chile (24 S–33 S) during the last 40,000 years. Paleoceanography, 19 (2).

Mohtadi, M., Hebbeln, D., & Marchant, M. (2005). Upwelling and productivity along the peru–chile current derived from faunal and isotopic compositions of planktic foraminifera in surface sediments. *Marine Geology*, *216*(3), 107– 126.

Mohtadi, M., et al. (2008) Deglacial pattern of circulation and marine productivity in the upwelling region off central-south Chile. Earth and Planetary Science Letters, 272 (1-2), p. 221-230.

Montecinos, A., & Aceituno, P. (2003). Seasonality of the enso-related rainfall variability in central chile and associated circulation anomalies. *Journal of climate*, *16*(2), 281–296.

Moore, J. K., Fu, W., Primeau, F., Britten, G. L., Lindsay, K., Long, M., Doney, S. C., Mahowald, N., Hoffman, F., & Randerson, J. T. (2018). Sustained climate warming drives declining marine biological productivity. Science, 359 (6380), 1139–1143. https://doi.org/10.1126/science.aao6379

Morales, C. E., Blanco, J. L., Braun, M., Reyes, H., & Silva, N. (1996). Chlorophyll-a distribution and associated oceanographic conditions in the upwelling region off northern chile during the winter and spring 1993. *Deep Sea Research Part I: Oceanographic Research Papers*, *43*(3), 267–289.

Moreno, P. I., Denton, G. H., Moreno, H., Lowell, T. V., Putnam, A. E., & Kaplan, M. R. (2015). Radiocarbon chronology of the last glacial maximum and its termination in northwestern patagonia. *Quaternary Science Reviews*, *122*, 233–249.

Moreno, P. I., Videla, J., Valero-Garc´es, B., Alloway, B. V., & Heusser, L. E. (2018). A continuous record of vegetation, fire-regime and climatic changes in northwestern patagonia spanning the last 25,000 years. *Quaternary Science Reviews*, *198*, 15–36.

Morley, A., Babila, T. L., Wright, J., Ninnemann, U., Kleiven, K., Irvali, N., & Rosenthal, Y. (2017). Environmental controls on mg/ca in neogloboquadrina incompta: A core-top study from the subpolar north atlantic. *Geochemistry, Geophysics, Geosystems*, *18*(12), 4276–4298.

Munday, D. R., Johnson, H. L., & Marshall, D. P. (2013). Eddy saturation of equilibrated circumpolar currents. *Journal of Physical Oceanography*, *43*(3), 507– 532.

Muratli, J., Chase, Z., Mix, A., & McManus, J. (2010). Increased glacial-age ventilation of the chilean margin by antarctic intermediate water. *Nature Geoscience*, *3*(1), 23–26.

Naidu, P. D., & Malmgren, B. A. (1996). A high-resolution record of late quaternary upwelling along the oman margin, arabian sea based on planktonic foraminifera. *Paleoceanography*, *11*(1), 129–140.

Niebler, H.-S., Hubberten, H.-W., & Gersonde, R. (1999). Oxygen isotope values of planktic foraminifera: A tool for the reconstruction of surface water stratification. *Use of proxies in paleoceanography* (pp. 165–189). Springer.

Nier, A. O. (1940). A mass spectrometer for routine isotope abundance measurements. *Review of Scientific Instruments*, *11*(7), 212–216.

Ninnemann, U. S., & Charles, C. D. (1997). Regional differences in quaternary Subantarctic nutrient cycling: Link to intermediate and deep water ventilation. *Paleoceanography*, *12*(4), 560–567. https://doi.org/10.1029/97PA01032

Oeschger, H., Beer, J., Siegenthaler, U., Stauffer, B., Dansgaard, W., & Langway, C. (1983). Late-glacial climate history from ice cores. *Palaeoclimatic research and models* (pp. 95–107). Springer.

EPICA community members (2006) One-to-one coupling of glacial climate variability in greenland and antarctica. (2006). *Nature*, *444*(7116), 195–198.

Oppo, D. W., & Lehman, S. J. (1995). Suborbital timescale variability of north atlantic deep water during the past 200,000 years. *Paleoceanography*, *10*(5), 901–910.

Ottens, J. J., & Nederbragt, A. J. (1992). Planktic foraminiferal diversity as indicator of ocean environments. *Marine Micropaleontology*, *19*(1-2), 13–28.

Parker, F. L. (1962). Planktonic foraminiferal species in pacific sediments. *Micropaleontology*, *8*(2), 219–254.

Pearson, P. N., Wade, B. S., & Huber, B. T. (2018). Taxonomy, biostratigraphy, and phylogeny of oligocene globigerinitidae (dipsidripella, globigerinita, and tenuitella). Cushman Foundation for Foraminiferal Research.

Pedro, J. B., Jochum, M., Buizert, C., He, F., Barker, S., & Rasmussen, S. O. (2018). Beyond the bipolar seesaw: Toward a process understanding of interhemispheric coupling. *Quaternary Science Reviews*, *192*, 27–46.

Pinochet, A., Garc´es-Vargas, J., Lara, C., & Olguın, F. (2019). Seasonal variability of upwelling off central-southern chile. *Remote Sensing*, *11*(15), 1737.

Pisias, N. G., Heusser, L., Heusser, C., Hostetler, S. W., Mix, A. C., & Weber, M. (2006). Radiolaria and pollen records from 0 to 50 ka at odp site 1233: Continental and marine climate records from the southeast pacific. *Quaternary Science Reviews*, *25*(5-6), 455–473.

Po¨rtner, H.-O., Roberts, D. C., Masson-Delmotte, V., Zhai, P., Tignor, M., Poloczanska, E., & Weyer, N. (2019). The ocean and cryosphere in a changing climate. *IPCC Special Report on the Ocean and Cryosphere in a Changing Climate*.

Quade, J., & Kaplan, M. (2017). Lake-level stratigraphy and geochronology revisited at lago (lake) cardiel, argentina, and changes in the southern hemispheric westerlies over the last 25 ka. *Quaternary Science Reviews*, *177*, 173–188.

Rahmstorf, S. (2002). Ocean circulation and climate during the past 120,000 years. *Nature*, *419*(6903), 207–214.

Rahmstorf, S. (2006). Thermohaline ocean circulation.

Rasmussen, L., Conway, H., & Raymond, C. (2007). Influence of upper air conditions on the patagonia icefields. *Global and Planetary Change*, *59*(1-4), 203–216.

Ravelo, A., Fairbanks, R., & Philander, S. (1990). Reconstructing tropical atlantic hydrography using planktontic foraminifera and an ocean model. *Paleoceanography*, *5*(3), 409–431.

Reynolds, L. A., & Thunell, R. C. (1986). Seasonal production and morphologic variation of neogloboquadrina pachyderma (ehrenberg) in the northeast pacific. *Micropaleontology*, 1–18.

Rohling, E. J., & Cooke, S. (1999). Stable oxygen and carbon isotopes in foraminiferal carbonate shells. *Modern foraminifera* (pp. 239–258). Springer.

Romero, O. E., Kim, J.-H., & Hebbeln, D. (2006). Paleoproductivity evolution off central chile from the last glacial maximum to the early holocene. *Quaternary Research*, *65*(3), 519–525.

Rosman, K., & Taylor, P. (1998). Isotopic compositions of the elements 1997 (technical report). *Pure and Applied Chemistry*, *70*(1), 217–235.

Ruddiman. (2001). *Earth's climate: Past and future*. W. H. Freeman.

Ruddiman, W. F. (1977). Late quaternary deposition of ice-rafted sand in the subpolar north atlantic (lat 40 to 65 n). *Geological Society of America Bulletin*, *88*(12), 1813–1827.

Rutllant, J., & Fuenzalida, H. (1991). Synoptic aspects of the central chile rainfall variability associated with the southern oscillation. *International Journal of Climatology*, *11*(1), 63–76.

Sagredo, E., & Lowell, T. (2012). Climatology of andean glaciers: A framework to understand glacier response to climate change. *Global and Planetary Change*, *86*, 101–109.

Sarmiento, J., Gruber, N., Brzezinski, M. *et al.* Erratum: High-latitude controls of thermocline nutrients and low latitude biological productivity. *Nature* **479**, 556 (2011). https://doi.org/10.1038/nature10605

Sautter, L. R., & Thunell, R. C. (1991). Seasonal variability in the δ18o and δ13c of planktonic foraminifera from an upwelling environment: Sediment trap results from the san pedro basin, southern california bight. *Paleoceanography*, *6*(3), 307–334.

Schmidtko, S. & Johnson, G. C. (2012) Multidecadal Warming and Shoaling of Antarctic Intermediate Water**. Journal of climate, 25.

Schiebel, R., & Hemleben, C. (2017). Classification and taxonomy of extant planktic foraminifers. *Planktic foraminifers in the modern ocean* (pp. 11–110). Springer Berlin Heidelberg.

Schmittner, A., Bostock, H. C., Cartapanis, O., Curry, W. B., Filipsson, H. L., Galbraith, E. D., Gottschalk, J., Herguera, J. C., Hoogakker, B., Jaccard, S. L., Lisiecki, L. E., Lund, D. C., Mart´ınez-M´endez, G., Lynch-Stieglitz, J., Mackensen, A., Michel, E., Mix, A. C., Oppo, D. W., Peterson, C. D., . . . Waelbroeck, C. (2017). Calibration of the carbon isotope composition (13c) of benthic foraminifera. Paleoceanography, 32 (6), 512–530

Schneider, C., & Gies, D. (2004). Effects of el nin˜o–southern oscillation on southernmost south america precipitation at 53 s revealed from ncep–ncar reanalyses and weather station data. *International Journal of Climatology: A Journal of the Royal Meteorological Society*, *24*(9), 1057–1076.

Shin, S.-I., Liu, Z., Otto-Bliesner, B. L., Kutzbach, J. E., & Vavrus, S. J. (2003). Southern ocean sea-ice control of the glacial north atlantic thermohaline circulation. *Geophysical Research Letters*, *30*(2).

Simstich, J., Sarnthein, M., & Erlenkeuser, H. (2003). Paired δ18o signals of neogloboquadrina pachyderma (s) and turborotalita quinqueloba show thermal stratification structure in nordic seas. *Marine Micropaleontology*, *48*(1-2), 107– 125.

Spero, H. J., & Lea, D. W. (1996). Experimental determination of stable isotope variability in globigerina bulloides: Implications for paleoceanographic reconstructions. *Marine Micropaleontology*, *28*(3-4), 231–246.

Stocker, T. F., & Johnsen, S. J. (2003). A minimum thermodynamic model for the bipolar seesaw. *Paleoceanography*, *18*(4).

Straub, D. N. (1993). On the transport and angular momentum balance of channel models of the antarctic circumpolar current. *Journal of physical oceanography*, *23*(4), 776–782.

Strub, P. T., J. M. Mesías, V. Montecino, J. Rutllant, and S. Salinas (1998) Coastal ocean circulation off western South America - Coastal segment (6,E). The sea - the Global Coastal Ocean. Regional Studies and Syntheses, 11, p. 273-315.

Sun, S., Thompson, A. F., Xie, S.-P., & Long, S.-M. (2022). Indo-pacific warming induced by a weakening of the atlantic meridional overturning circulation. Journal of climate, 35 (2), 815–832.

Talley, L. (1996). Antarctic intermediate water in the south atlantic. *The south atlantic* (pp. 219–238). Springer.

Talley, L. D. (1999). Some aspects of ocean heat transport by the shallow, intermediate and deep overturning circulations. *Geophysical Monograph-American Geophysical Union*, *112*, 1–22.

Thiede, J. (1975). Distribution of foraminifera in surface waters of a coastal upwelling area. *Nature*, *253*(5494), 712–714.

Thornburg, T. M., & Kulm, L. D. (1987). Sedimentation in the chile trench; petrofacies and provenance. *Journal of Sedimentary Research*, *57*(1), 55–74.

Tiedemann, R., & Mix, A. C. (2007). Leg 202 synthesis: Southeast pacific paleoceangraphy. *Proceedings of the Ocean Drilling Program. Scientific Results*, *202*.

Tierney, J. E., Zhu, J., King, J., Malevich, S. B., Hakim, G. J., & Poulsen, C. J. (2020). Glacial cooling and climate sensitivity revisited. *Nature*, *584*(7822), 569–573.

Tolderlund, D. et al. (1971). Distribution and ecology of living planktonic foraminifera in surface waters of the atlantic and indian oceans. *The micropaleontology of oceans*, 105–149.

Trenberth, K. E. (1991). Storm tracks in the southern hemisphere. *Journal of Atmospheric Sciences*, *48*(19), 2159–2178.

Tsuchiya, M. (1989). Circulation of the antarctic intermediate water in the north atlantic ocean. *Journal of Marine Research*, *47*(4), 747–755.

Urey, H. C. (1947). The thermodynamic properties of isotopic substances. *Journal of the Chemical Society (Resumed)*, 562–581.

Van Leeuwen, R. J. W. (1989). *Sea-floor distribution and late quaternary faunal patterns of planktonic and benthic foraminifers in the angola basin* (Doctoral dissertation). University Utrecht.

Voelker, A. H. et al. (2002). Global distribution of centennial-scale records for marine isotope stage (mis) 3: A database. *Quaternary Science Reviews*, *21*(10), 1185– 1212.

Wefer, G., & Berger, W. H. (1991). Isotope paleontology: Growth and composition of extant calcareous species. *Marine geology*, *100*(1-4), 207–248.

Wollenburg, J. E., & Mackensen, A. (1998). Living benthic foraminifers from the central arctic ocean: Faunal composition, standing stock and diversity. *Marine Micropaleontology*, *34*(3-4), 153–185.

Wright, A. K., & Flower, B. P. (2002). Surface and deep ocean circulation in the subpolar north atlantic during the mid-pleistocene revolution. *Paleoceanography*, *17*(4), 20–1.

Wu, G., & Hillaire-Marcel, C. (1994). Oxygen isotope compositions of sinistral neogloboquadrina pachyderma tests in surface sediments: North atlantic ocean. *Geochimica et Cosmochimica Acta*, *58*(4), 1303–1312.

Zemp, M., Huss, M., Thibert, E. (2019) Global glacier mass changes and their contributions to sea-level rise from 1961 to 2016. *Nature* **568**, 382–386

9. Appendix

Appendix A

Foraminiferal and lithic Counts from ODP site 1233

Core section	depth(cm)	mcd	G. bulloides %	G. glutinata%	N. incompta%	G. inflata%	T. quinqueloba	N.pachyderma	G. Truncatulinc	G. Crassaformis	O. Universa%	Other%	Benthics%	IRD%	Coiling ratio
7H-3	76	76.190	15,45	15,45	22,76	13,82	1,63	26,02	2,03	0,00	0,00	6,91	33,51	0,00	53,33
7H-3	84	76.270	14,98	11,11	20,29	16,43	4,35	29,95	0,97	0,00	0,00	1,93	28,87	0,00	59,62
7H-3	92	76.350	10,58	7,81	25,69	10,08	4,28	36,52	2,02	0,00	1,26	1,76	22,61	0,00	58,70
7H-3	116	76.590	16,07	13,57	15,71	14,29	1,43	35,00	2,14	0,36	0,36	1,07	31,54	0,00	69,01
7H-3	124	76.670	21,63	19,23	9,62	16,35	0,96	26,44	3,85	0,00	0,00	1,92	39,53	0,00	73,33
7H-3	132	76.750	21,43	17,46	16,67	13,89	4,76	19,05	2,38	0,79	0,00	3,57	45,10	0,00	53,33
7H-4	2	76.950	25,18	13,65	27,53	11,06	1,88	18,35	0,94	0,00	0,24	1,18	31,67	0,00	40,00
7H-4	10	77.030	21,26	7,09	35,83	6,68	0,81	26,32	1,21	0,00	0,00	0,81	22,81	0,00	42,35
7H-4	18	77.110	15,17	6,18	37,45	8,24	1,12	27,34	0,75	0,00	0,75	3,00	24,47	0,00	42,20
7H-4	26	77.190	26,61	8,87	31,05	10,89	0,40	19,35	0,00	0,81	0,40	1,61	15,36	0,00	38,40
7H-4	34	77.270	16,86	5,75	44,06	7,28	1,53	24,52	0,00	0,00	0,00	0,00	23,46	0,00	35,75
7H-4	42	77.350	23,59	5,63	40,49	3,17	1,41	23,59	1,41	0,00	0,70	0,00	19,77	0,00	36,81
7H-4	50	77.430	29,92	3,69	31,97	7,38	0,82	23,36	2,05	0,41	0,20	0,20	9,29	0,00	42,22
7H-4	58	77.510	24,21	5,95	31,75	12,70	2,38	20,24	1,19	0,79	0,40	0,40	16,56	0,00	38,93
7H-4	66	77.590	23,11	6,37	31,13	5,42	1,65	27,83	3,07	0,47	0,00	0,94	29,22	2,17	47,20
7H-4	74	77.670	27,04	7,73	27,47	12,45	1,72	21,46	2,15	0,00	0,00	0,00	22,59	0,33	43,86
7H-4	82	77.750	20,77	4,07	27,29	11,81	1,63	32,79	1,63	0,00	0,00	0,00	22,06	1,59	54,58

7H-4	90 77.830	17,39	4,06	28,70	6,38	2,32	39,71	1,45	0,00	0,00	0,00	13,97	1,25	58,05
7H-4	98 77.910	22,30	5,76	27,70	9,71	0,72	33,45	0,36	0,00	0,00	0,00	24,86	1,62	54,71
7H-4	118 78.110	23,27	7,23	26,73	16,04	2,20	22,96	0,00	0,63	0,94	0,00	13,11	1,91	46,20
7H-4	126 78.190	20,73	4,36	35,64	17,82	1,09	17,09	0,00	1,82	1,09	0,36	12,14	3,51	32,41
7H-4	134 78.270	11,04	3,07	53,68	7,06	0,31	23,31	0,31	0,61	0,61	0,00	8,43	3,65	30,28
7H-4	142 78.350	16,82	3,36	39,45	14,98	1,83	20,80	1,53	0,61	0,61	0,00	10,66	1,37	34,52
7H-5	4 78.480	14,36	3,59	51,03	11,03	0,00	18,97	0,26	0,26	0,26	0,26	15,58	1,52	27,11
7H-5	12 78.560	13,68	4,72	45,28	19,34	0,00	16,04	0,00	0,94	0,00	0,00	16,86	3,53	26,15
7H-5	20 78.640	14,09	7,34	43,45	12,50	0,40	19,44	1,19	0,40	0,79	0,40	13,55	0,34	30,91
7H-5	28 78.720	17,63	2,52	34,01	9,57	0,50	33,50	1,76	0,50	0,00	0,00	18,98	0,82	49,63
7H-5	36 78.800	20,66	2,82	40,14	12,21	0,00	23,94	0,23	0,00	0,00	0,00	16,80	2,34	37,36
7H-5	44 78.880	16,67	3,70	38,89	21,60	1,54	16,67	0,00	0,93	0,00	0,00	13,14	1,61	30,00
7H-5	52 78.960	9,18	4,11	42,72	12,97	1,58	27,85	1,27	0,32	0,00	0,00	20,40	0,25	39,46
7H-5	60 79.040	14,45	1,77	41,00	24,78	0,59	14,45	2,65	0,29	0,00	0,00	16,09	2,72	26,06
7H-5	68 79.120	9,36	3,48	47,33	11,50	1,87	25,94	0,00	0,00	0,53	0,00	22,41	0,41	35,40
7H-5	76 79.200	12,06	2,01	43,97	15,83	1,76	20,85	0,50	1,01	2,01	0,00	24,91	0,94	32,17
7H-5	84 79.280	11,95	2,92	46,94	5,54	1,46	30,03	0,29	0,58	0,29	0,00	29,86	2,66	39,02
7H-5	92 79.360	12,38	3,57	53,10	3,57	2,38	22,86	0,48	0,00	0,95	0,71	20,30	0,38	30,09
9H-3	4 79.380	14,36	8,21	32,82	4,10	0,51	37,44	0,51	0,00	2,05	0,00	62,57	0,77	53,28

7H-5	100 79.440	20,50	5,44	43,10	3,77	1,26	23,01	2,09	0,42	0,00	0,42	43,76	0,94	34,81
9H-3	12 79.460	20,38	6,71	45,56	5,28	1,68	19,18	1,20	0,00	0,00	0,00	39,91	1,01	29,63
7H-5	108 79.520	20,93	5,81	38,37	8,14	3,49	22,09	1,16	0,00	0,00	0,00	39,44	1,41	36,54
9H-3	20 79.540	27,84	5,69	31,14	8,98	3,59	20,96	0,90	0,00	0,60	0,30	47,07	0,00	40,23
9H-3	28 79.620	19,72	6,88	35,09	14,68	0,92	21,33	0,00	0,69	0,00	0,69	12,63	0,80	37,80
9H-3	36 79.700	29,44	12,69	24,87	6,60	1,52	24,87	0,00	0,00	0,00	0,00	27,04	1,48	50,00
9H-3	44 79.780	12,65	6,44	36,28	17,42	0,00	26,73	0,48	0,00	0,00	0,00	10,28	0,00	42,42
9H-3	52 79.860	13,08	6,96	42,19	17,51	1,48	18,57	0,00	0,00	0,00	0,21	18,42	0,86	30,56
9H-3	60 79.940	20,27	3,79	31,82	21,40	0,95	20,83	0,95	0,00	0,00	0,00	8,17	0,00	39,57
9H-3	68 80.020	14,60	4,42	32,74	25,22	2,65	19,03	0,44	0,00	0,88	0,00	26,86	0,32	36,75
9H-3	76 80.100	8,65	1,92	46,15	13,94	0,48	26,92	1,44	0,00	0,48	0,00	45,26	0,53	36,84
9H-3	84 80.180	14,97	1,70	38,44	23,13	1,02	20,07	0,34	0,00	0,00	0,34	14,78	2,32	34,30
9H-3	92 80.260	29,79	2,13	29,79	17,02	2,13	19,15	0,00	0,00	0,00	0,00	84,79	0,00	39,13
9H-3	100 80.340	10,48	1,37	44,87	17,31	0,68	24,15	0,23	0,00	0,00	0,91	21,04	0,18	34,98
9H-3	108 80.420	15,73	3,23	37,72	11,21	1,72	28,66	1,08	0,43	0,00	0,22	25,40	0,48	43,18
9H-3	116 80.500	28,74	6,90	18,39	22,13	2,30	19,54	0,57	0,29	0,00	1,15	31,76	0,00	51,52
9H-3	124 80.580	21,80	7,52	30,33	9,27	2,26	27,82	0,00	0,75	0,00	0,25	25,14	0,75	47,84
9H-4	2 80.690	19,90	6,28	36,91	8,90	2,09	25,65	0,26	0,00	0,00	0,00	19,92	0,00	41,00
9H-4	10 80.770	19,50	3,50	32,25	7,25	2,00	34,50	1,00	0,00	0,00	0,00	12,66	0,00	51,69

9H-4	18 80.850	25,94	3,53	39,29	4,79	2,52	22,92	0,50	0,50	0,00	0,00	16,95	0,00	36,84
9H-4	26 80.930	21,43	4,08	34,69	11,73	2,30	24,74	1,02	0,00	0,00	0,00	21,91	0,40	41,63
9H-4	34 81.010	20,10	2,18	35,35	17,19	1,21	22,76	0,97	0,24	0,00	0,00	18,86	0,59	39,17
9H-4	42 81.090	21,71	2,33	30,62	7,36	2,33	34,88	0,00	0,00	0,00	0,78	11,34	0,34	53,25
9H-4	50 81.170	27,82	3,67	26,51	13,91	1,05	26,25	0,26	0,00	0,00	0,52	13,41	0,00	49,75
9H-4	58 81.250	27,37	2,67	24,49	21,81	2,26	18,93	0,62	0,21	0,82	0,82	13,06	0,54	43,60
9H-4	70 81.370	15,34	5,52	26,38	10,43	2,45	37,12	1,84	0,00	0,31	0,61	26,91	0,45	58,45
9H-4	78 81.450	12,99	6,49	26,41	3,90	3,03	45,45	0,87	0,43	0,43	0,00	68,14	0,00	63,25
9H-4	86 81.530	15,32	4,50	28,53	8,41	3,60	38,14	0,60	0,00	0,30	0,60	55,66	0,13	57,21
9H-4	94 81.610	19,94	4,62	19,94	8,67	2,89	41,62	0,87	0,29	0,29	0,87	47,58	0,00	67,61
9H-4	102 81.690	34,39	3,56	18,58	8,70	1,98	30,04	1,58	0,00	1,19	0,00	41,71	0,69	61,79
9H-4	110 81.770	16,96	6,61	16,96	13,66	1,76	40,75	2,20	0,00	0,88	0,22	7,63	0,00	70,61
9H-4	118 81.850	16,67	2,04	27,55	9,18	2,38	39,80	0,68	0,00	1,02	0,68	24,23	0,26	59,09
9H-4	126 81.930	25,81	4,03	27,15	5,65	2,15	31,45	2,96	0,00	0,27	0,54	25,60	0,00	53,67
9H-5	2 82.020	31,58	4,93	21,71	7,24	2,63	27,96	2,30	0,33	1,32	0,00	11,63	0,00	56,29
9H-5	10 82.100	25,41	3,83	28,96	4,64	4,37	30,87	1,37	0,00	0,27	0,27	17,19	0,23	51,60
9H-5	18 82.180	18,92	1,50	28,53	4,80	5,41	33,33	1,80	0,00	4,50	1,20	9,26	0,54	53,88
9H-5	26 82.260	31,78	3,04	22,66	4,67	3,04	31,31	0,23	0,00	2,34	0,93	16,89	0,19	58,01
9H-5	34 82.340	51,77	3,00	16,35	1,63	1,91	22,62	1,91	0,82	0,00	0,00	10,49	0,24	58,04

Appendix B

C. wuellerstorfi $\delta^{18}O$ and $\delta^{13}C$ data from ODP Site 1233

Core section	depth(cm)	mcd	Average C. wuellerstorfi δ13C (‰)	Average C. wuellerstorfi δ18O (‰)
7H-3	76	76,19	0,88	3,64
7H-3	84	76,27	0,61	3,43
7H-3	92	76,35	0,4	3,72
7H-3	116	76,59	0,75	3,68
7H-3	124	76,67	0,93	3,62
7H-3	132	76,75	1,31	3,69
7H-4	2	76,95	0,39	3,57
7H-4	10	77,03	0,66	3,8
7H-4	18	77,11	0,77	3,49
7H-4	26	77,19	0,64	3,63
7H-4	34	77,27	0,54	3,46
7H-4	42	77,35	0,54	3,64
7H-4	50	77,43	0,69	3,92

7H-4	58	77,51	0,94	3,31
7H-4	66	77,59	0,69	3,52
7H-4	74	77,67	0,97	3,5
7H-4	82	77,75	-0,32	3,46
7H-4	90	77,83	0,72	3,56
7H-4	98	77,91	0,67	3,5
7H-4	118	78,11	1,04	3,48
7H-4	126	78,19	0,89	3,41
7H-4	134	78,27	0,58	3,41
7H-4	142	78,35	0,44	3,46
7H-5	4	78,48	0,95	3,76
7H-5	12	78,56	0,66	3,36
7H-5	20	78,64	0,71	3,6
7H-5	28	78,72	0,81	3,34
7H-5	36	78,80	0,74	3,48
7H-5	44	78,88	1,21	3,26
7H-5	52	78,96	0,87	3,53
7H-5	60	79,04	0,91	3,37

7H-5	68	79,12	0,12	3,38
7H-5	76	79,20	0,61	3,26
7H-5	84	79,28	1,16	3,48
7H-5	92	79,36	1,06	3,36
9H-3	4	79,38	0,74	3,35
7H-5	100	79,44	1,03	3,47
9H-3	12	79,46	0,87	3,67
7H-5	108	79,52	1,34	3,44
9H-3	20	79,54	0,53	3,51
9H-3	28	79,62	1,08	3,34
9H-3	36	79,70	0,16	3,57
9H-3	44	79,78	0,56	3,46
9H-3	52	79,86	0,64	3,55
9H-3	60	79,94	1,03	3,44
9H-3	68	80,02	0,79	3,59
9H-3	76	80,10	0,57	3,54
9H-3	84	80,18	1,41	3,54
9H-3	92	80,26	1,53	3,61

9H-3	100	80,34	0,18	3,6
9H-3	108	80,42	0,27	3,78
9H-3	116	80,50	0,59	3,99
9H-3	124	80,58	0,34	3,59
9H-4	2	80,69	0,16	4,11
9H-4	10	80,77	0,52	3,68
9H-4	18	80,85	0,5	3,44
9H-4	26	80,93	0,62	3,43
9H-4	34	81,01	0,14	3,57
9H-4	42	81,09	0,2	3,59
9H-4	50	81,17	1	3,48
9H-4	58	81,25	0,8	3,32
9H-4	70	81,37	0,71	3,33
9H-4	78	81,45	0,91	3,3
9H-4	86	81,53	-0,94	3,48
9H-4	94	81,61	0,11	3,22
9H-4	102	81,69	0,51	3,5
9H-4	110	81,77	1,08	3,57

9H-4	118	81,85	0,9	3,79
9H-4	126	81,93	0,99	3,38
9H-5	2	82,02	0,89	3,49
9H-5	10	82,10	0,31	3,57
9H-5	18	82,18	1,23	3,4
9H-5	26	82,26	1,29	3,56
9H-5	34	82,34	0,85	3,76
9H-5	42	82,42	0,54	3,68
9H-5	50	82,50	0,35	3,68
9H-5	58	82,58	0,42	3,73
9H-5	66	82,66	0,59	3,76
9H-5	74	82,74	0,66	3,66
9H-5	82	82,82	0,81	3,74
9H-5	90	82,90	0,68	3,74
9H-5	98	82,98	0,5	3,89
9H-5	106	83,06	0,62	4,02
9H-5	114	83,14	0,65	3,87
9H-5	122	83,22	0,32	3,74

9H-5	130	83,30	0,41	3,96
9H-5	138	83,38	0,26	3,76
9H-6	4	83,49	-0,03	3,88
9H-6	12	83,57	0,32	3,72
9H-6	20	83,65	0,93	3,87